3D dynamics of crustal deformation along the western Andean margin

Investigations on strain partitioning above an obliquely convergent oceanic subduction zone using a 3D numerical geodynamical model

JORINA MARLENA SCHÜTT

ACADEMIC DISSERTATION

To be presented, with the permission of the Faculty of Science of the University of Helsinki, for public examination in Auditorium A111, Exactum (Gustaf Hällströmin katu 2b, Helsinki) on 23 February 2018, at 12 o'clock noon.

Helsinki 2018

DEPARTMENT OF GEOSCIENCES AND GEOGRAPHY A63 / HELSINKI 2018

Author: Jorina Marlena Schütt
Department of Geoscience and Geography
P.O. Box 68
00014 University of Helsinki
Finland

Supervisor: Associate Professor David Whipp
Department of Geoscience and Geography
University of Helsinki

Reviewers: Professor Ulrich Riller
Department of Earth Sciences
University of Hamburg

Professor Hemin Koyi
Department of Earth Sciences
Uppsala University

Opponent: Professor Claire Currie
Department of Physics
University of Alberta

ISSN 1798-7911
ISBN 978-951-51-3978-8 (pbk)
ISBN 978-951-51-3979-5 (PDF)

Unigrafia
Helsinki 2018

Schütt J., 2018. *3D dynamics of crustal deformation along the western Andean margin*. Unigrafia. Helsinki. 139 pages, 69 figures and 3 tables.

Abstract

Subduction zones play an important role in the dynamics of the Earth. At plate margins, where one tectonic plate subsides underneath a second one, mountain ranges are built, earthquakes experienced and volcanic activity observed. The subduction zone of South America, where the Nazca Plate slides underneath the South American Plate, extends for roughly 7000 km along the plate margin of the continent. Ongoing since at least the Cretaceous this subduction zone is a laboratory for tectonic systems. This study focuses on how the geometry and relative motion of the two convergent plates affects dynamics in the overriding plate utilizing 3D numerical mechanical and thermo-mechanical models.

Along the South American subduction zone the obliquity angle, subduction dip angle and strength of the continental crust vary. All these factors influence the dynamics and deformation of the continental crust and affect – especially in oblique subduction systems – how oblique convergence is partitioned onto various fault systems in the overriding plate. The partitioning of strain into margin-normal slip on the plate-bounding fault and horizontal shearing on a strike-slip system parallel to the margin is mainly controlled by the margin-parallel shear forces acting on the plate interface and the strength of the continental crust. While the plate interface forces are influenced by the dip angle of the subducting plate (i.e., the length of plate interface in the frictional domain) and the obliquity angle between the normal to the plate margin and the plate convergence vector, the strength of the continental crust is strongly affected by the presence or absence of weak zones such as regions of arc volcanism, pre-existing fault systems, or boundaries of stronger crustal blocks. In order to investigate which of these factors are most important in controlling how the overriding continental plate deforms, this study compares results of lithospheric-scale 3D numerical geodynamic experiments from two regions in the north-central Andes: the Northern Volcanic Zone (NVZ; 5°N - 3°S) and adjacent Peruvian Flat Slab Segment (PFSS; 3°S -14°S).

The NVZ is characterized by a ~35° subduction dip angle, an obliquity angle of about 40°, extensive volcanism and significant strain partitioning in the continental crust. In contrast, the PFSS is characterized by flat subduction (the slab flattens beneath the continent at around 100 km depth for several hundred kilometers), an obliquity angle of about 20°, no volcanism and minimal strain partitioning. The geometry and strength characteristics of these regions are incorporated in 3D (1600 x 1600 x 160 km) numerical experiments of oceanic subduction beneath a continent, focusing on the conditions under which strain partitioning occurs in the continental plate. In addition to different slab geometries and obliquity angles, the effect of a continental crust of uniform strength (friction angle $\varphi = 15^{\circ}$) versus one including a weak zone in the continental crust ($\varphi = 2^{\circ}$) that runs parallel to the margin is compared in

systematic purely mechanical experiments. Finally, reference models representing the NVZ and PFSS are revisited with fully coupled thermo-mechanical experiments.

Results of the experiments show that the obliquity angle has, as expected, the largest effect on initiation of strain partitioning, but development of sliver movement parallel to the margin is clearly enhanced by the presence of a continental weakness. While velocities in the continental sliver in the NVZ reference model are similar to the values observed in nature, the model without a continental weakness develops slivers with velocities half as fast. In addition, a shallower subduction angle results in formation of a wider continental sliver. Based upon the results, the lack of strain partitioning observed in the PFSS results from both a low convergence obliquity and lack of a weak zone in the continent, even though the shallow subduction should make strain partitioning more favorable. Purely mechanical models are despite their simplicity a good suited tool for investigations of subduction zone dynamics and in very good agreement with observations in nature in the particular study areas of this work as well as global subduction zones. The sliver movement observed in the thermo-mechanical models agrees well with purely mechanical reference experiments representing the NVZ and the PFSS. While this is the case, the thermo-mechanical experiments do expose the boundary between successful (NVZ) and partly failing (PFSS) incorporation of temperature dependence into mechanical models. With this they provide a good starting point for further refinement and development of temperature dependent experiments.

Acknowledgments

I would like to thank my supervisor David Whipp for introducing me to the world of subduction zone modeling and for his support and encouragement during the project. Also, I would like to thank Lars Kaislaniemi for his help and advice, Emilia Koivisto and Ilmo Kukkonen as well as Seija Kultti and Tapani Rämö for their feedback, ideas and support. Thank you also to Annakaisa Korja and the people of the Institute of Seismology for accommodating me.

I wish to thank my parents and friends for being there – near and far.

This project was financially supported by a Three-Year Research Grant from the University of Helsinki.

Helsinki, February 2018

You are braver than you believe,
stronger than you seem,
and smarter than you think.
Winnie the Pooh
A. A. Milne

Contents

List of symbols and abbreviations

symbol or abbreviation	unit	**description**
α	°	subduction dip angle
A		proportionality coefficient; arbitrary point
A_b	m^2	area of basal thrust in a subduction zone
A_r	m^2	area of vertical rear shear zone of a subduction zone
ALE		Arbitrary Lagrangian-Eulerian
c	Pa	cohesion
CCPP		Chingual-Cosanga-Pallatunga-Puná (Shear Zone)
C_p	J/K	heat capacity
CFL		the Courant–Friedrichs–Lewy (condition)
η	Pa· s	viscosity
$\frac{\partial}{\partial t}$		Eulerian time derivate
$\frac{D}{Dt}$		Lagrangian time derivate
div	$\frac{\partial F_x}{\partial x} + \frac{\partial F_y}{\partial y} + \frac{\partial F_z}{\partial z}$	divergence; defined as a scalar function over a three dimensional vector field F
DGM		Dolores Guayaquil Mega (Shear Zone)
ϵ		strain
$\dot{\epsilon}$	1/s	strain rate
FEM		Finite Element Method
F_{MC}		yield function for the Mohr-Coulomb yield criterion
$F(x)$		Function *F* of *x*
τ_f	kg/ms^2	inter plate frictional force
F_p	kg/ms^2	margin parallel force component
F_R	kg/ms^2	resisting force
g	m/s^2	gravitational acceleration (g = 9.81 m/s^2)
grad	$\left(\frac{\partial S}{\partial x}, \frac{\partial S}{\partial y}, \frac{\partial S}{\partial z}\right)$	gradient; defined as a differential operator over a three dimensional scalar field S
H	J	volumetric heat production
i		natural number; index number
ICF		incompressible fluid
j		natural number; index number
k	W/ (m·K)	thermal conductivity
λ	Pa·s	penalty factor
γ	°	obliquity angle
M	kg	mass
MA		material acceleration
M_W		moment magnitude (earthquake scale)
N		natural number
$\mathbb{N}$		set of all natural numbers
n		natural number; power law exponent
NAB		North Andean Block
NAS		North Andean Sliver
NVZ		Northern Volcanic Zone

(n_1, n_2, n_3)		set of normal vectors in $\mathbb{R}^3$
P	kg · m/s	momentum
p	Pa	pressure
φ		friction angle
Φ_i		i component of shape function
PFSS		Peruvian Flat Slab Segment
Q	kJ/mol	activation energy
q	W/m^2	heat flux
R	m^2kg/s^2K	the Boltzmann gas constant ($R = 1.3 \cdot 10^{-23}$ m^2kg/s^2K)
$\mathbb{R}^3$		real coordinate space in three dimensions
R_B	kg/ms^2	slab bending resistance force
ρ	kg/m^3	density
σ_{ij}		stress tensor
σ_d	Pa	differential stress
σ_n	Pa	normal stress
σ_m	Pa	mean stress
σ_y	Pa	yield stress
σ_1	Pa	maximum principle stresses
σ_3	Pa	minimum principle stresses
t	s	time
T	°C	temperature
τ	Pa	shear strength
τ_f	Pa	subduction shear stress
τ_m	Pa	maximum shear strength
τ_n	Pa	margin – normal component of subduction shear stress
τ_p	Pa	margin – parallel component of subduction shear stress
τ_v	Pa	margin – vertical component of subduction shear stress
U	J	energy
$\vec{v}$		velocity vector
v_i	m/s	i-th component of velocity field
v_{adv}	cm/a	advancing subduction velocity
v_{conv}	cm/a	total relative convergence velocity
v_s	cm/a	subduction velocity
v_{p100}	cm/a	margin parallel velocity component of a fully partitioned system
v_{n100}	cm/a	northward pointing velocity component of a fully partitioned system
x	m	x-coordinate in a Cartesian coordinate system
(x_1, x_2, x_3)		coordinates in a Cartesian coordinate system
(X_1, X_2, X_3)		set of body forces on a three dimensional body in $\mathbb{R}^3$
(x,y)		pair of coordinates in $\mathbb{R}^2$
(x,y,z)		set of coordinates on $\mathbb{R}^3$
y	m	y-coordinate in a Cartesian coordinate system
z	m	z-coordinate in a Cartesian coordinate system
z_f	m	depth range of faults

1 Introduction and motivation

The Earth's lithosphere is a strong layer overlying the rheologically weaker asthenosphere. The idea of continents drifting on the asthenosphere was first introduced by Wegener in 1912. This idea was rejected due to the lack of a driving factor. After mantle convection was suggested as a possible mechanism for moving continents by Holmes in 1931, the idea of the lithosphere consisting of several main and micro plates drifting on asthenosphere was established. Including important ideas, such as sea-floor spreading as the driver of plate movement (Hess, 1962) the life cycle of tectonic plates was described by Wilson (1966) in the framework of the eponymous Wilson cycle. At ocean ridges magmas rise, producing new plate material and pushing the adjacent tectonic plates away from each other. This ridge push plate driving force is together with the slab pull and drag force at the base of the plates the driving mechanism that leads the continents to drift apart from each other, collide or subduct (Turcotte and Schubert, 2014). In total, three types of plate boundaries are distinguished: divergent plate margins, where new oceanic lithosphere is produced, convergent plate margins, where lithosphere is destroyed by one plate subducting beneath the other, and transform margins, where lithosphere is neither produced nor destroyed but the plates slide horizontally past each other (Wessel and Müller, 2009). In general, relative motion of two (or more) plates causes earthquakes, which define the plate boundaries. Volcanism is also often observed in connection with plate boundaries: at ocean ridges and subduction zones. However, also magma rising in intraplate regions (plumes) leads to volcanism.

A subduction zone (cf. Figure 1.1) is a convergent plate boundary, where an oceanic (or continental) plate starts to bend due to negative buoyancy and induced weaknesses (e.g. penetration of fluids) and subducts beneath a continental or oceanic plate. The subducting slab sinks following a parabolic shape into the mantle where certain temperature and pressure conditions are reached and the slab melts. Volatiles and hot mantle wedges enhance melting (Gaetani and Grove, 1998). These melts cause arc volcanism in the overriding plate. Subduction zones can be distinguished upon different slab geometries, plate configurations and plate strengths, which all influence the dynamics of the overriding plate and the entire subduction zone system.

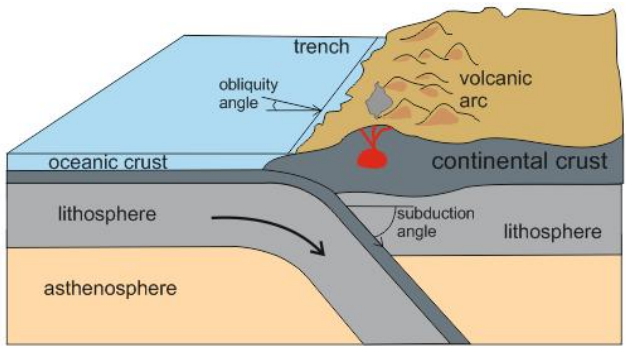

Figure 1.1. Schematic representation of a subduction zone.

The steepness of the subducting slab is one important criterion and is defined as the average angle between the horizontal (overriding) and subducting plate. Normal subduction denotes a subducting slab descending at an angle of around 30° (Kumar, et al., 2016). Subduction dip angles of less than 30° are abnormal cases of subduction and occur only in cases where the subducting slab is buoyant enough to stay directly underneath the overriding lithosphere the subduction is shallow (Lallemand et al., 2005). Highly buoyant slabs commonly result in flat subduction, which describes that the subducting slab declines normally at first, but then continues at a relatively shallow depth almost horizontally for several hundreds or thousands of kilometers and finally sinks deep into the mantle (Gutscher, et al., 1999; 2000; Kumar, et al., 2016). Due to higher buoyancy oceanic ridges descending with the oceanic plate play an important and possibly decisive role in shallow and flat subduction occurrence (Gutscher, et al., 1999; 2000; van Hunen, et al., 2002; 2004; Ramos and Folguera, 2009). A steep-angle subduction (more than 30°) on the other hand occurs mainly in subduction zones where an old and thick – and thus very dense – subducting plate is overridden. A prominent example is the Mariana Trench: here the dipping angle is at the steepest (almost vertical) and the oceanic crust is the oldest on Earth (Jurassic in age). Steep subduction zones are associated with extensive volcanism (e.g. Barazangi and Isacks, 1978).

Subduction systems are always accompanied by seismicity, volcanism is not always present. Flat or shallow subduction is often marked with the absence of volcanic arcs. Requirements of pressure and temperature to melt the slab are usually not met in flat or shallow subduction settings as the slab does not reach deep enough. Instead of magmatism, low heat flow (30 – 70 mW/m^2) in the crust and high level of seismicity is experienced (Gutscher et al., 2000). Friction between the slab and the overriding plate accumulates stress, which is released in earthquakes (e.g. Barazangi and Isacks, 1978, Dumitru, 1991, Lallemand et al., 2005). Normal to steep subduction zones experience both volcanism, high heat flow (50 – 120 mW/m^2) in the crust and seismicity in the slab (Gutscher, et al., 2000).

A second important criterion in subduction zone configuration is the angle of plate convergence obliquity, which is the angle between the velocity vector and the margin of the subducting plate. The obliquity angle plays a key role in the upper plate dynamics. The plate convergent motion can be accommodated by oblique slip on the plate-bounding fault system or strain can be partitioned (i.e., Fitch, 1972). Strain partitioning in this context is defined as the division of oblique convergence into margin-normal slip on the plate-bounding fault and horizontal shearing on a strike-slip system parallel to the subduction margin. Thus, an oblique subduction system may or may not have this deformation along the margin as a strike-slip strain system (see also Figure 3.5). Strain partitioning is observed in several subduction zones on Earth in oceanic as well as continental settings. However, areas of strain partitioning are not equally distributed along subduction zones as can be seen in the global map (Figure 1.2) of major plate boundaries, locations of subduction zones and areas of strain partitioning (based on Jarrard, 1986).

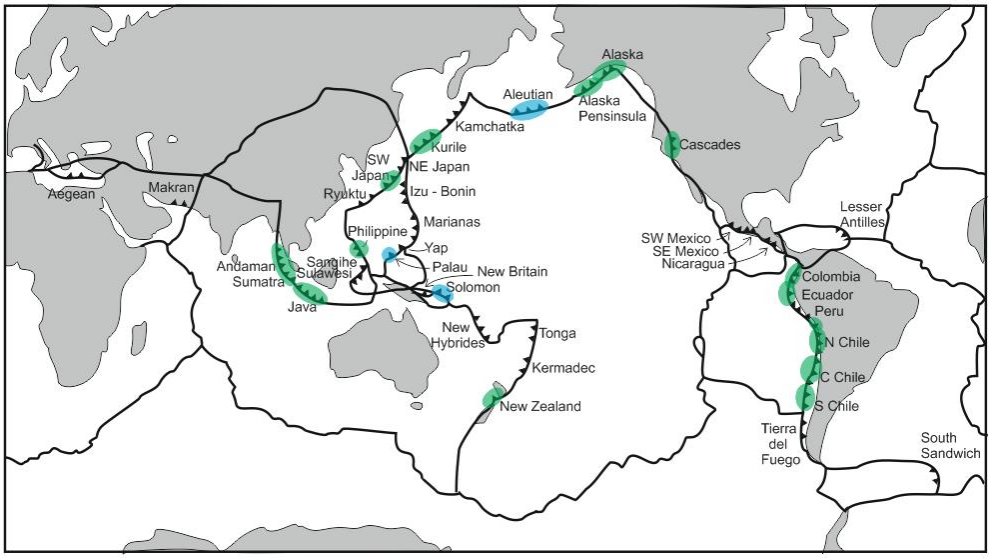

Figure 1.2. Global map of major plate boundaries and subduction zones (after Jarrard, 1986). Areas with strain partitioning indicated for oceanic (blue) and continental (green) plate margins.

Subduction angle and obliquity angle as well as pre-existing fault zones, sutures and volcanic arcs, i.e. weaknesses in the continental crust, influence the dynamics of the subduction zone (e.g. Ramos, 1999; Gutscher et al., 2000). Observations suggest that subduction zones with certain characteristics, like high obliquity angle and present continental crustal weakness, experience strain partitioning in the continental crust, while others do not: It is thought that the obliquity angle is the main controlling parameter in these tectonic scenarios (e.g. Fitch, 1972; Nocquet el al., 2014). The subduction angle largely determines the formation of volcanic arcs, which in turn act as weaknesses in the system (Dewey and Lamb, 1992). However, volcanic arcs are not necessarily triggering strain partitioning (Alvarado, et al., 2016) but are thought to only enhance the partitioning of the continental crust. In addition, plate tectonic fault systems are weakening the lithosphere and act as an initiator or enhancer for strain partitioning (Alvarado, et al., 2016). The extent to which the above characteristics control strain partitioning has however not previously been investigated in detail and it is the primary goal of this study to investigate how the following factors might be correlated: the subduction angle, the obliquity angle, a weakness (e.g. volcanic arc or shear zones) in the continental crust and strain partitioning.

First numerical modelling studies investigated mechanisms of oceanic subduction (Minear and Toksöz, 1970) and mantle convection (Torrance and Turcotte, 1971), the two key factors behind plate movement in the at that time recently formulated plate tectonic theory. The insufficiency of analog models handling thermal advection, which is essential in plate tectonic models, made the step from analog to numerical models inevitable. Not only oceanic

subduction but also continental collisions (e.g. Bird, 1978) and other aspects of plate tectonics have been investigated with the help of numerical experiments since then (Burov, et al., 2014). Several experiments have been focusing on the initiation of slab subduction (e.g. Hager and O´Connell, 1978; Hassani, et al., 1997; Schmeling, et al., 2008; Baes, et al., 2011). These have shown that a slab does not automatically sink into the mantle when it becomes old and cold (as suggested by early plate tectonic theory) but that plate strength grows with age and the plate becomes too strong to bend without precedent weakening. Local weakening of the oceanic crust can be achieved by fluids penetrating into fractures resulting from bending of the plate (Burov, et al., 2014). Also, friction between the subducting and overriding plate is important and numerical models focusing on interplate coupling (e.g. Hassani, et al., 1997; Upton and Koons, 2003; Malatesta, et al., 2016) have shown that some kind of lubrication between the plates is necessary for plate subduction. Another issue well suited for numerical investigation is the timing, depth and impact of slab break off, which has been studied by a range of mantle scale experiments (e.g. Gerya, et al., 2004; Duretz, et al., 2010) together with mantle instabilities and dynamics (e.g. Gerya and Yuen, 2003; Arcay, et al., 2005; Sobolev, et al., 2006; Currie, et al., 2014). It has been shown that the impact of slab break off is a function of i. a. subduction rate and plate rheology (Burov et al., 2014).

Together with the advance of computing machines, the potential of numerical models has been improved. During the early stages in the 1970s only two dimension, rather simple, experiments could be performed. Today's models are capable of running complex thermomechanical models in two or three dimensions. This development goes hand in hand with increased knowledge on subduction zones and its dynamics (data acquisition by e.g. GPS and seismic stations) and increased desire to understand complex subduction zone geometries and dynamics better, also with regard to hazard assessment. Previous two dimensional modeling approaches on dynamics in an oblique subduction setting (e.g. Gerya, et al., 2004; Syracuse et al., 2010) are not sufficient for the investigations of the three dimensional problem of oblique motion. Past 3D modeling studies on oblique subduction have been focusing on fore-arc deformation (e.g. Kellner, 2007; Zeumann, 2013) and dynamics of the oceanic plate. Here, this study adds on and gives insight on dynamics of the continental plate in an oblique subduction setting using a 3D numerical thermodynamic model.

One of the most interesting subduction zones for geodynamic studies is the western margin of South America, the subduction of the oceanic Nazca Plate underneath the continental South American Plate (Figure 1.3).

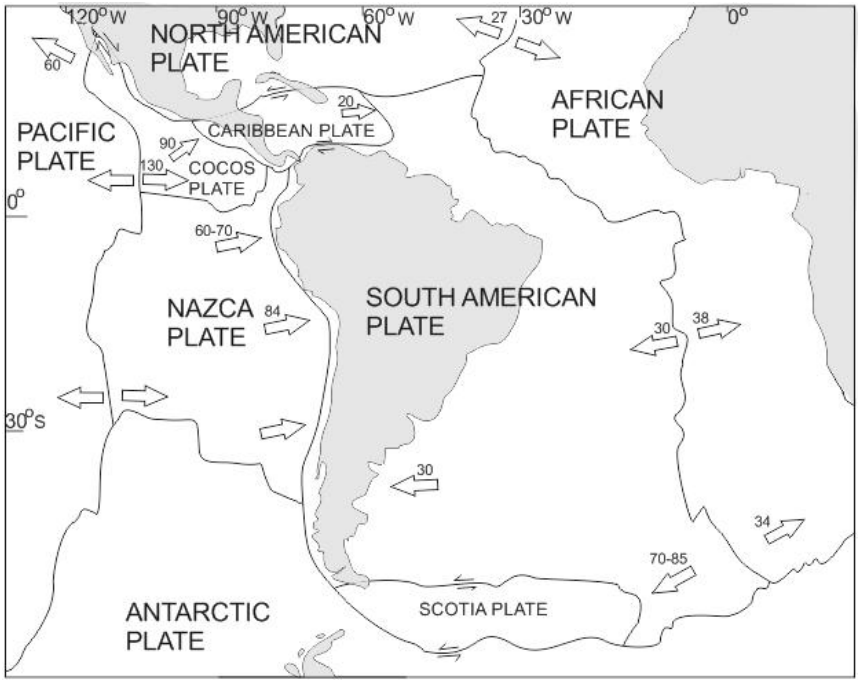

Figure 1.3. Present plate configuration (modified from Orme, 2007): The most important plate boundaries are a divergent plate margin separating the South American Plate from the African Plate and a subduction zone between the Nazca Plate and the South American Plate. Arrows with velocities in mm/year show approximate plate motions relative to the Mid Atlantic Ridge, the boundary between the African and the South American Plate.

The most prominent feature of South America is the Andes Mountain Range that extends along the entire western coast of the continent. The Andes comprise the highest non-collisional mountains in the world (Ramos, 1999). The mountain chain is approximately 7000 km long and between 200 and 700 km wide and the highest elevations reach 7000 m. These dimensions make it the longest and, save for Asia, also highest mountain range on Earth (Kono et al., 1989). This mountain range is the consequence of oceanic subduction since the Paleozoic or Mesozoic (Jaillard, et al., 1990 and references therein), with plate-tectonic activities continuing during the Cenozoic and still ongoing (Stern, 2004). The Nazca Plate (a segment of the former Pacific Plate) subducts with a total convergence velocity of about 5-7 cm/year (e.g., Stern, 2004; Gutscher et al., 2000; Nocquet et al., 2014). The subduction margin is not uniform in symmetry and dynamics along its entire length and subduction and obliquity angle vary. Furthermore, volcanic activity and earthquake occurrences change along the margin. It is notable that flat and steep subduction zones alternate along the margin, coinciding with absence and presence of a volcanic arc, respectively (Rosenbaum, et al., 2005). Several different divisions of the Andes prevail. A common first-order division is the one into the Northern Andes (12°N-3°S), the Central Andes (3-47°S) and the Southern Andes (47-56°S) (e.g. Ramos, 1999; Gausser, 1975).

Further distinctions have been made according to tectonic or geological characteristics. Figure 1.4 shows the division of the Andes and the main geological/geographical features of it.

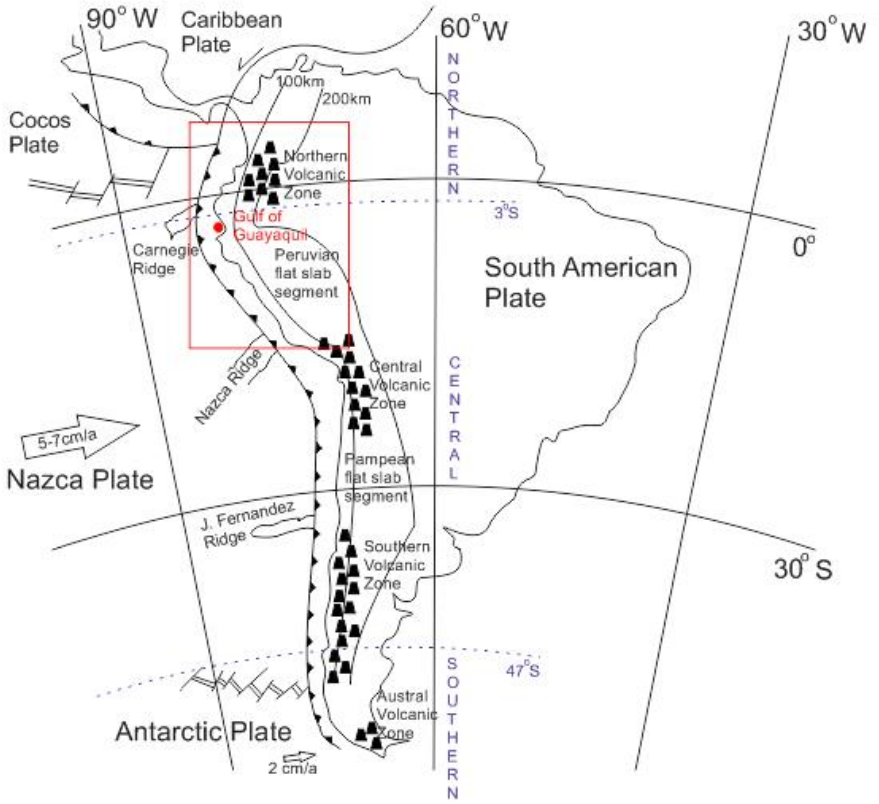

Figure 1.4. The Andes with the division into the Northern, Central and Southern Andes (blue dashed lines at 3° and 47°S and with the volcanic zones indicated; following Stern (2004); the study areas (red box) of the Northern Volcanic Zone (NVZ, 5°N - 3°S) and adjacent Peruvian flat slab segment (PFSS, 3°S - 14°S); modified after Gutscher et al. (2000).

For this work, an investigation area between 5°N and 14°S in the Northern and Central Andes was chosen (rectangle in Figure 1.4). This area includes two different zones (following the division by Stern, 2004): the Northern Volcanic Zone (NVZ, 5°N - 3°S) in the North and the Peruvian flat slab segment (PFSS, 3°S - 14°S) in the South. The main emphasis of this work is on the NVZ, which is characterized by steep (approx. 35°) oblique (about 40°) subduction and a prominent volcanic zone (e.g. Ramos, 1999; Stern, 2014) and shear zones (e.g. Veloza, et al., 2012; Yepes, et al., 2016, Alvarado et al., 2016). In this area, strain partitioning is observed with a sliver movement of about 1cm/year (Nocquet, et al.,

2014; Gutscher et al., 1999). The PFSS is characterized by flat subduction (initial subduction angle about 25° and flattening once reaching to a depth of approx. 100 km; Ramos, 1999; Gutscher, et al., 2000). The obliquity angle is disputed in literature and varies from similar to the NVZ (40°; e.g. Velosa et al., 2012; Mc Nulty et al. 2002, Pulido et al., 2014) to much smaller (10°-20°; Knezevic Antonijevic et al., 2015; Yepes et al., 2016; Ramos, 1999). The PFSS lacks volcanism and experiences only weak strain partitioning, about 0.5 cm/year (Nocquet et al., 2014).

In pursuit of investigating the influence of subduction dip angle, convergence obliquity, and weaknesses in the crust on strain partitioning behavior, lithospheric-scale 3D numerical geodynamic experiments have been undertaken. Case Study I focuses on the NVZ: a model is designed to represent normal to steep subduction with high obliquity angle and a continental crustal weakness. Several tests have been carried out including en- and disabling the continental weakness as well as varying subduction and obliquity angle. The results of this study show that the obliquity angle is, as expected, the crucial factor for initiating strain partitioning. Margin-parallel mass transport velocities in the continental sliver are similar to the values observed in the NVZ (about 1 cm/year) and twice as high as in models with a continental zone of weakness compared to those without, meaning that strain partitioning is also controlled by crustal strength. In addition, a shallower subduction angle results in a wider continental sliver. Case Study II focuses on the PFSS: a model is designed to represent flat subduction with low obliquity angle and no continental crustal zone of weakness. Here, mainly tests regarding the obliquity angle have been carried out. Maximum margin-parallel mass transport velocities are similar to observed velocities in the PFSS (around 5 mm/year) and suggest that the obliquity angle is a main driving force of strain partitioning. Both Case Study I and II are purely mechanical models. In order to investigate the effect of heat flow and temperature dependence Case Study III revisits both study areas with a thermo-mechanical model. The sliver formation in the thermo-mechanical models agrees well with results from the purely mechanical reference experiments representing the NVZ and the PFSS. While the NVZ experiment is successfully incorporating temperature dependence into purely mechanical experiments, the more complicated slab geometry of the PFSS leaves weaknesses to be refined and developed in future thermo-mechanical experiments.

2 Tectonic and geological setting in the northern and central Andes of South America (5°N and 14°S)

2.1 The South American Plate

The formation of the supercontinent Rodinia (at about 1 Ga) led to the formation of major features of today's South American Plate. The collision of land masses, later to be called Laurentia and South America, formed the basis of the South American North and North-East craton. After the breakup of Rodinia (at about 750 Ma) and several subsequent collisions and rifting events (e.g. Gondwanaland and Pangaea), Pangaea started to drift apart about 200 Ma ago. North America and Eurasia and the continents of today's southern hemisphere formed successively. South America separated from Africa as Antarctica was placed over the South Pole (Levin, 2013). During the last 80 Ma years, the Mid Atlantic Ocean Ridge has pushed Africa and South America further apart towards the present configuration of the continents.

With the separation of Pangaea and the onset of the Mid Atlantic Ridge on the eastern side of South America, the western side is forced into a convergent plate boundary. The convergent tectonic setting with the Farallon Plate subducting under the North and South American Plate had already started in the Jurassic and a complex plate tectonic history in the circum-Gulf of Mexico region to begin (Pindell and Kennan, 2009). The tectonic scenario of South America, however, has not changed very much since the Cretaceous (Cobbold, et al., 2007; and references therein). The Nazca Plate subducts since the final breakup of the Farallon Pacific Plate into Nazca and Cocos Plate ~24 Ma ago with a total convergence velocity of about 5-7 cm/year (e.g., Stern, 2004; Gutscher et al., 2000; Cobbold, et al., 2007; Nocquet et al., 2014). Moreover, the margin is due to westward migrating of South America (Cobbold, et al., 2007) experiencing advancing subduction. This implies together with oblique motion changes in e.g. position of rifts underneath the continent (Gutscher, et al., 1999; Stern, 2004; discussed later).

Several different divisions of the Andes can be found in literature. A common first order division is the one into the Northern Andes (12°N - 3°S), the Central Andes (3 - 47°S) and the Southern Andes (47 - 56°S) (e.g. Gansser, 1973; Ramos, 1999). Then, further distinctions are made according to tectonic or geological characteristics. The division with respect to volcanic zones and steep vs. flat slab segments is shown in Figure 1.4.

2.2 The Northern Volcanic Zone (NVZ, 5°N - 3°S)

The Northern Andes extend from 5°N to about 3°S (Figure 2.1). As a boundary and distinction between the Northern Andes and the central segment of the Andes, a sharp geological boundary at the latitude of the Gulf of Guayaquil (approx. 3°S) is established in form of the Grijalva Fault Zone: accreted oceanic terranes in the North and continental crust

to the South (Gansser, 1973), belonging to the Nazca slab and the old oceanic Farallon slab (subducting underneath North and South America), respectively.

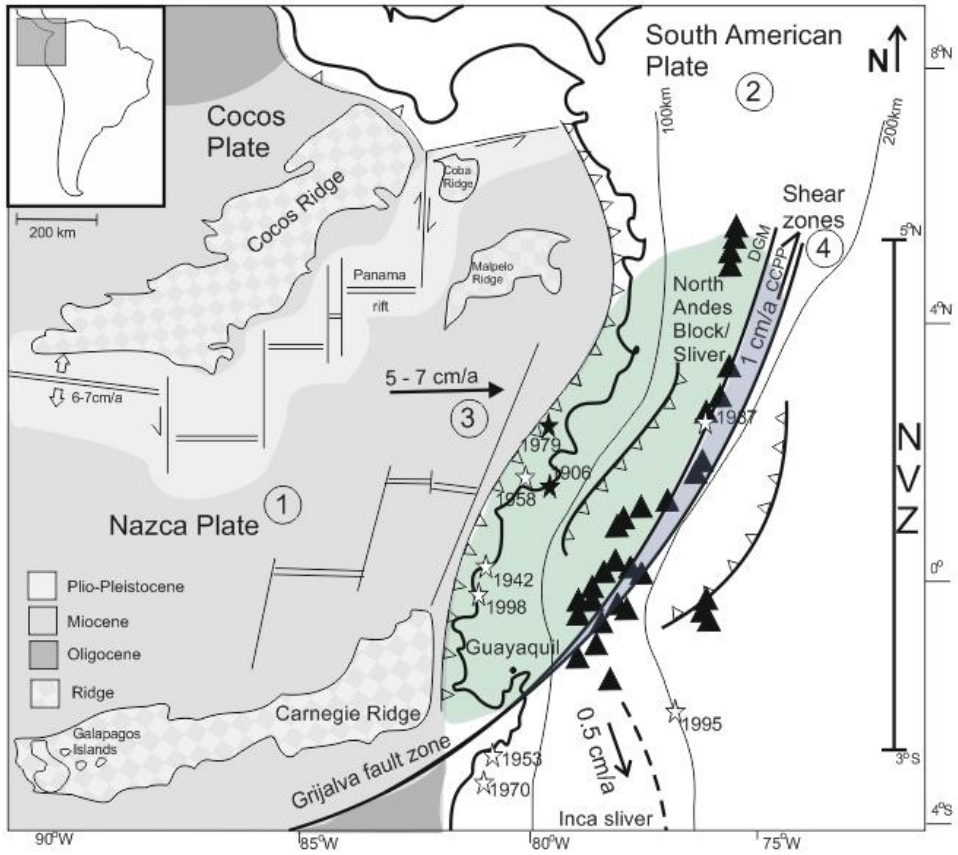

Figure 2.1. Northern Volcanic Zone (NVZ) between 5°N - 3°S (modified from Gutscher et al., 1999 and Yepes, et al., 2016) (1) Nazca Plate, (2) South American Plate converging with (3) a velocity relative to South America of 5-7cm/a with obliquity angle of about 40°, (4) volcanic arc and shear zones revealing strain partitioning. Margin parallel sliver movement (about 1cm/a) of the North Andes Block (NAB, green shaded area) and the Northern Andes Sliver (NAS, green and blue shaded area) are bounded by the Dolores Guayaquil Mega (DGM) shear and the Chingual-Cosanga-Pallatunga-Puná (CCPP) shear, respectively. The Inca sliver is located south of the Grijalva fault zone and movement rates of 0,5 cm/a are observed. The 100 km and 200 km isolines of the subducting slab as well as the Carnegie, the Cocos Ridge and minor Coba and Malpelo Ridge are indicated. Ages of the oceanic crust are shaded in grey (after Cobbold and Rossello, 2003). Black triangles show the approximate location of Holocene volcanoes. The position of nine $M_W \geq 7.0$ earthquakes of the twentieth century in the NVZ are marked with white ($M_W \geq 7.0$) and black ($M_W \geq 8.0$) stars ([year; M_W]: [1906; 8.8], [1942;7.8], [1953;7.6], [1958;7.6], [1970;7.2], [1979;8.1], [1987;7.1], [1995;7.0], [1998;7.1])

About 200 km south of the crustal boundary of the Gulf of Guayaquil, a deflection marking abrupt change in structural trend from North-West to North-North-East, is a second indicator for the boundary between the Northern and Central Andes (e.g. Ham and Herrera, 1963). More recent studies including geophysical and geochemical studies have confirmed and refined the border: Bouguer gravity maps provided independent evidence to establish the oceanic and continental boundary (Mooney, 1979) and paleomagnetic studies confirm and support allochthonous terranes being of multiple origin (Roperch et al., 1987; Cosma et al., 1998).

Separating the Northern and the Central Andes the Grijalva Fault Zone reaches in South-West North-East direction into the Gulf of Guayaquil and further inland, where it merges with a system of shear and thrust faults. The Dolores Guayaquil Mega (DGM) Shear Zone (Campbell, 1974; Gutscher, et. al., 1999; Lavenu, 2006) reaches from the Gulf of Guayaquil north-eastward through the Andean Cordillera of Ecuador and Colombia. This right-lateral fault marks the distinct boundary for the North Andean Block (NAB; Gutscher, et al., 1999, 2000, Bourgois, 2013), a continental sliver being displaced at rates of 1cm/a along the continental margin. However, 15 Ma of exhumation and tectonic history of accreted terranes (Pindell and Kennan, 2009) suggest that with the north-eastward movement of the NAB also its boundary migrated north-eastward (Alvarado, et al., 2016). A new tectonic map of Ecuador connects the Grijalva Fault zone with the Chingual-Cosanga-Pallatunga-Puná (CCPP) Shear Zone (Yepes, et al., 2016, Alvarado et al., 2016), a right-lateral shear fault sharply marking the new eastern boundary of the North Andean Sliver (NAS), the expanded NAB, and leaves the DGM as an ancient shear zone inactive (Alvarado, et al., 2016). Both right-lateral shear faults do however belong to the extensive system of (abandoned, reactivated and new) shear and thrust faults (Veloza, et al., 2012, Alvarado, et al., 2016) located in the Andean Cordillera of Ecuador and Colombia. This fault system approximately coincides with the volcanic arc in the continent and determines sharply the boundary of the NAB (cf. Figure 2.1).

During the Jurassic (201 – 145 Ma), Cretaceous (145 – 66 Ma) and Paleogene (66 – 23 Ma) oceanic crust accreted into what is today's western margin of the South American Plate. This crust is still present as oceanic basement and the main constituent of the Northern Andes (Almeida, et al., 2000). The accretion of the oceanic basement of the Northern Andes was during that time related to ophiolite obduction, penetrative deformation and metamorphism.

During the Cretaceous and early Cenozoic times, oceanic volcanic arcs were amalgamated after each collision by high-angle, west-verging thrusts to form the western mountain ranges of the Northern Andes. These thrusts form today an extensive system of abandoned, reactivated and active fault and shear zones (including DGM and CCPP) in the NVZ. This part of the mountain chain is characterized by heavily deformed rocks and ophiolitic suites. A continental magmatic arc was deformed between the western and the eastern Cordillera during mid-Cenozoic times (Ramos, 2015). The eastern parts of the Northern Andes resulted from collision of the Caribbean and the South American Plate (Ramos, 2015). The shear zones, the boundary between the former Pacific Plate and the Nazca Plate, was already established while the triple point between South American, Caribbean and Nazca Plates was

still unstable (Pindell and Kennan, 2009). This tectonic instability resulted in the initiation of another plate, the Cocos Plate, around 7 Ma (Bandy, et al., 2000) and generally in a system of rather scattered transition faults, rifts and ridges in the North Pacific oceanic plate configuration (e.g. Gutscher, et al., 1999). The Cocos Ridge (~ 5° N, Figure 2.2) is sitting on the Cocos Plate and thus influencing mostly the tectonics of the Caribbean, Panama and North American Plates. It is further approximately marking the boundary between the Cocos and Nazca Plate. South of this boundary two minor ridges (not in Figure 2.2; cf. e.g. Gutscher, et al., 1999 for detailed map) and several rift zones and transform faults are complicating the tectonic system. The subduction slab dip angle beneath the NVZ is normal with ~35° (e.g. Gutscher, et al., 1999; Stern, 2004). The Carnegie Ridge (0° latitude) is the southern boundary of this complex area and at the same time the southern boundary of the NVZ on the Nazca Plate. The ridge itself, located north of the Grijalva Fault Zone, is an aseismic, oceanic plateau and has a big influence on the subducting slab geometry as well as on the overall continental topography and dynamics. Due to its higher elevation relative to the surrounding sea floor and the difference in rock composition (younger volcanic rocks and thus more buoyant) it is subducting with a shallow angle (~20°) and even pushing into the continental plate, resulting in an increased coastal relief (Gutscher, et al., 1999). The overall subduction zone configuration has not changed since the Late Cretaceous (Cobbold, et al., 2007).

Volcanism was initiated in the Neogene by partial melting of the mantle wedge due to subduction of oceanic lithosphere (Stern, 2004) and the NVZ is still today characterized by extensive volcanism (e.g. Ramos, 1999; Stern 2004). Volcanoes are usually located about 100 - 200 km from the margin. Over this distance, the slab descends to a depth of about 100 km and reaches temperature and pressure conditions under which magma is produced (Molnar, et al., 1979). There are around 75 active and extinct volcanoes in the NVZ, of which more than 2/3 are located in Ecuador (see Figure 2.1; Stern, 2004 and references therein). Volcanoes become inactive due to changes in the subduction zone configuration, like e.g. migration of flat slab segments or ridges (Stern, 2004). Steep subduction is in theory often the result of old and dense lithosphere sinking due to low buoyancy (Stern, 2004). Contrary to what this would imply on the NVZ, the slab subducting underneath the continental South American Plate is rather young (12 – 20 Ma, Stern, 2004). The yet relatively steep slab dip can be either explained by melting of oceanic lithosphere at the edges of the neighboring Carnegie Ridge resulting in a lithospheric tear dragging the slab deeper downward or by detachment of the buoyant ridge from the oceanic crust assisted by a pre-existing rift (Gutscher, et al., 1999). It is however speculated that the ridge continues independently underneath the South American Plate, tending north-eastward accompanying the DGM (or CCPP) shear zone for up to 500 km (Gutscher, et al., 1999). The abrupt change in subduction dip angle in connection with the Carnegie Ridge and the buoyant ridge migrating underneath the continental plate itself is having an effect on the interplate coupling between the Nazca and South American Plate. The NVZ volcanic arc is more or less coinciding with the system of DGM shear and fault zones (Gutscher, et al., 1999) and only several tens of kilometers off the main shear zone (Alvarado, et al., 2016; Yepes, et al., 2016).

There is potentially a strong interplate coupling between the subducting and overriding plate in shallow subduction zones. The overtime accumulating stress is released in earthquakes (e.g. Lallemand, et al., 2005, Barazangi and Isacks, 1978) with a higher magnitude in shallow subduction zones compared to steep subduction zones (Stern, 2002, Gutscher, et al., 1999). The earthquake foci mark the approximate location of the slab interface. This way, seismic evidences allow tectonic reconstructions and the out lining of the slab (Gutscher, et al., 1999, Rosenbaum, et al., 2005). Deep earthquake foci (to ~200 km) depth have been measured in the northern region of the NVZ (5°N), whereas rather shallow earthquakes (< 70 km) have been recorded at latitudes of the Carnegie Ridge (~0°) (e.g. Gutscher et al., 1999, 2000). The earthquake pattern is describing steep subduction north of and flat subduction above the Carnegie Ridge. The subduction zone along the western border of South America is generally one of the most active convergent margins on Earth (Yepes, et al., 2016 and references therein). Only during the twentieth century, eight $M_W > 7.0$ earthquakes have been measured, five of them in the Northern Andes domain north of the Grijalva fault and three in the northern segment of the Central Andes south of it (Yepes, et al., 2016). In the northern domain, the M_W 8.8 earthquake in 1906 Ecuador Colombia is one of the ten most powerful ever recorded by seismometers (Kanamori, 1977). The locations of the earthquakes are marked in Figure 2.1.

Focal mechanisms for earthquakes above magnitude 5 between 1900 and 2014 (from Harvard CTM database) are shown in Figure 2.2. Generally, focal mechanisms are bimodal with NW-SE and ENE-WSW maximum compressive stress directions associated with convergence and collision of the circum-Gulf of Mexico plates (Egbue and Kellog, 2010 and references therein). Many of the strike-slip earthquakes can be correlated to north-east trending displacement along fault systems in Ecuador and Colombia, including the Grijalva Fault Zone (Egbue and Kellog, 2010). Deep earthquakes occur at depths of 163±10 km (Pennington, et al., 1979; Egbue and Kellog, 2010) and may represent the maximum thickness of the NAB/NAS (Egbue and Kellog, 2010). The crustal earthquakes reflect slip partitioning on high angle faults, which are located above crustal detachment ramps. Continental strike slip faults often extend over broad zones with up to 200-350 km width (Stevens, et al., 2002; Egbue and Kellog, 2010).

GPS data (Figure 2.2) (compiled from Veloza, et al. (2012)) include postseismic and interseismic deformations correlated with plate motion and crustal deformation at plate boundaries. The data show high inland velocities, especially in close vicinity to the Grijalva Fault Zone north of the Gulf of Guayaquil, which reflects strain associated with convergence at the Nazca – South American plate boundary. Approximately 50% of the convergence is locked at the subduction interface (Egbue and Kellog, 2010). The accumulated elastic strain in the overriding plate will be released in interplate thrust earthquakes as part of the Ecuador and Colombia Earthquake cycle.

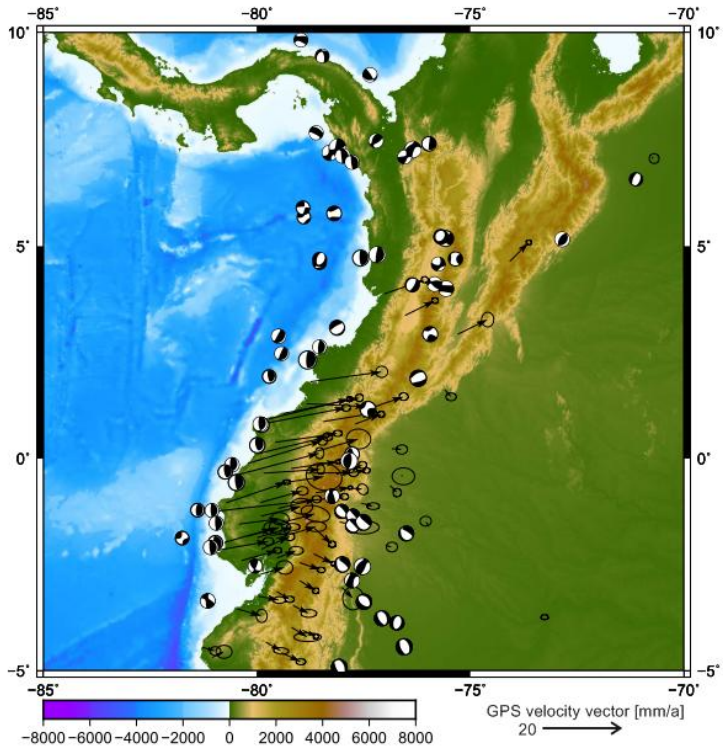

Figure 2.2. GPS data (compiled from Veloza, et al. (2012)) and focal mechanisms (from Harvard CTM database, years 1900 to 2014) for earthquakes above magnitude 5 in the Northern Andes.

Additionally, the NVZ is characterized by an obliquity angle of 40° (e.g. Nocquet, et al., 2014). The obliquity angle varies significantly along the western margin of the South American Plate from 2°N to 10°S with a total change of about 60° (Yepes, et al., 2016) or more (Veloza, et al., 2012; Pulido et al., 2014). The obliquity angle influences significantly not only the dynamics of the subduction zone, but also crustal morphology. As a consequence of oblique subduction and high coupling along the subducting slab interface, a tectonic block, wedged between the subducting slab and the inland shear zones, began to be pushed toward the northeast (Yepes, et al., 2016) in the Andes of north Ecuador. This block (or 'sliver') evolved, enhanced by pre-defined shear zones from oceanic terranes accretion during the Cretaceous and Paleogene (Pindell and Kennan, 2009), to be the NAB (Gutscher et al., 1999) or NAS (Alvarado, et al., 2016), respectively, cf. Figure 2.1, experiencing a margin parallel movement of about 1cm/a (Nocquet, et al., 2014).

2.3 The Peruvian Flat Slab Segment (PFSS, 3°S - 14°S)

The northern sector of the Central Andes extends from 3°S to 14°S (Carnegie Ridge in the North to Nazca Ridge in the South) and is also known as the Peruvian flat slab segment (PFSS, cf. Figure 2.3; Stern, 2004).

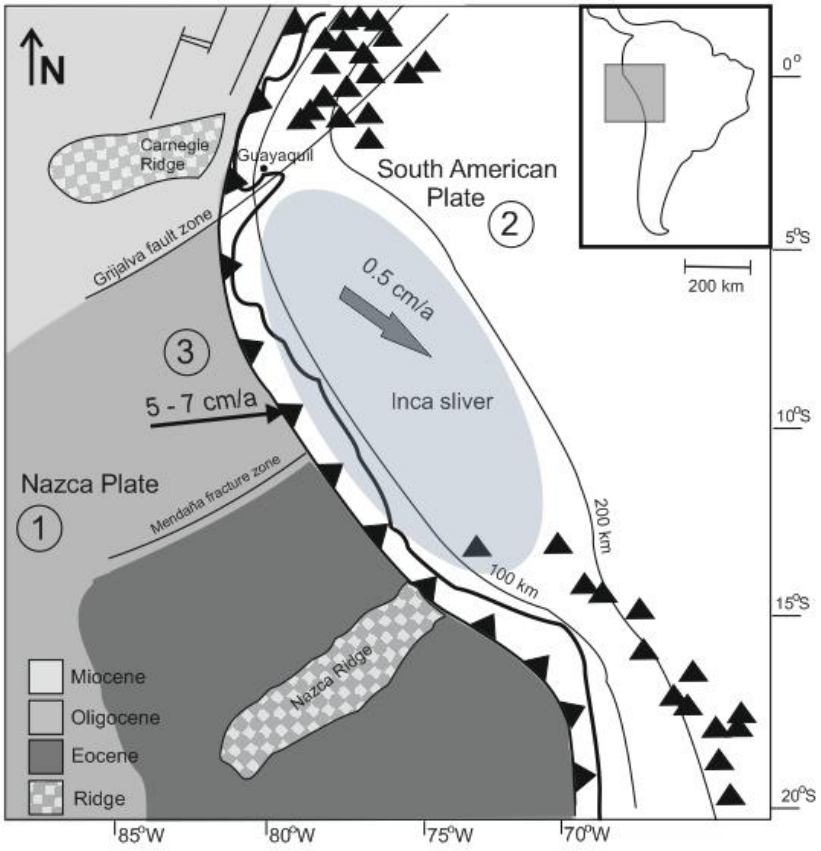

Figure 2.3. Peruvian Flat Slab Segment (PFSS) between 3°S - 14°S (modified from Huchon and Buorgois, 1990; Gutscher et al., 1999; Stern, 2004; Nocquet, et al., 2014) bordered by the Carnegie Ridge in the North and Nazca Ridge in in the South): (1) Nazca Plate, (2) South American Plate converging with (3) a velocity relative to South America of 5-7cm/a with obliquity angle of about 20°. Ages of the oceanic crust are shaded in grey (after Cobbold and Rossello, 2003). Black triangles show the approximate location of Holocene volcanoes. The Inca sliver (blue shaded) is located south of the Grijalva fault zone and movement rates of 0.5 cm/a are observed (Nocquet, et al., 2014). The 100 km and 200 km isolines of the subducting slab are indicated.

The formation of the Central Andes is driven by subduction processes that occurred in absence of major continent collisions (Jaillard, et al., 1990; Ramos, 1999; 2015). The Central Andes comprise one volcanic zone (central Central Andes) bounded by two flat slab segments (northern (cf. Figure 2.3) and southern Central Andes). A period of rifting-type extension during Triassic and Jurassic is recorded by subsidence and local unconformities (Jaillard, et al., 1990). Magmatic activity is during this period restricted to the Northern and central Central Andes (where also volcanism is observed also today). Magmatic belts in the Northern Andes and intrusions in the Central Andes mark the beginning of subduction around 190 – 180 Ma ago (Jaillard, et al., 1990). Scarcely distributed intrusions in what is today's PFSS are interpreted to result from highly oblique southeastward subduction (Jaillard, et al., 1990). In line with tectonic changes in the circum-Gulf of Mexico region, the setting in the Central Andes changed from extension to compression (Ramos, 1999). A very low convergence rate between the Farallon and the South American Plate is correlated to weak deformation and almost no magmatic activity between 30 and 26 Ma (Sébrier and Soler, 1991). After 26 Ma the tectonic setting changed and together with the breakup of the Farallon Plate into Nazca and Cocos Plate approx. 24 Ma ago (Cobbold, et al., 2007) the convergence velocity increased (Sébrier and Soler, 1991) and arc volcanism stopped around 4 Ma ago, around 5 Ma after the aseismic Nazca and Carnegie Ridge arrived at the margin (Faccenna, et al., 2017).

Today, the PFSS is characterized by lack of volcanism (Veloza, et al., 2012), which is generally the case above flat slab subduction zones (Stern, 2004). It is suggested that flat subduction was very common and important (for continental growth) in Earth's history (e.g. van Hunen, et al., 2004, Li et al., 2011). Today, flat subduction occurs at about 10% of convergent margins (e.g., Gutscher, et al., 2000; Lallemand, et al., 2005). Here, the slab sinks at an angle of between 30° to 10° (variation form north to south; e.g. Yepes, et al., 2016; Jarrard, 1986) down to an approximate depth of about 100 km depth and flattens out. It travels for around 300 km to 700 km (variation from north to south; Sacks, 1983; Gutscher, et al., 2000) almost horizontally until it steeply sinks into the mantle (Gutscher, et al., 1999). Even though buoyancy has a large influence on forcing old and dense lithosphere to sink and young (40-50 Ma; Jarrard, 1986) to resist subduction (Wortel, et al., 1991; Stern, 2002, van Hunen, et al., 2004), flat subduction is commonly observed at places where topographic anomalies subduct (Rosenbaum, et al., 2005). Such anomalies can be for example above mentioned oceanic ridges (van Hunen, et al., 2004).

There are three major oceanic ridges (North to South: Carnegie Ridge, Nazca Ridge and J. Fernandez Ridge; cf. Figure 1.4) influencing the subduction of the Nazca Plate underneath the South American Plate. Most importantly, the elevation and composition of the ridge result in shallow subduction dip angle (Pilger et al., 1981) and possibly control the geology and topography of the overlying area (Jordan et al., 1983). Oceanic ridges are of more recent volcanic (plume) origin than the surrounding oceanic plate and thicken the oceanic crust locally, which is why the average density for the oceanic lithosphere is lower (more buoyant) than for the continental lithosphere. This local anomaly in buoyancy results in shallow subduction dip angles (Gutscher, et al., 1999, van Hunen, et al., 2004). In a similar way as the Carnegie Ridge (discussed above in Chapter 2.2), the Nazca Ridge is thought to have

influenced or caused the flat subduction in the PFSS. The Carnegie and the Nazca Ridge are framing the PFSS in the northern Central Andes: Both ridges are migrating north-eastward beneath the South American Plate. This way, a flat slab subduction has been introduced in the PFSS since the last about 8-5 Ma (Berrocal and Fernandez, 2005).

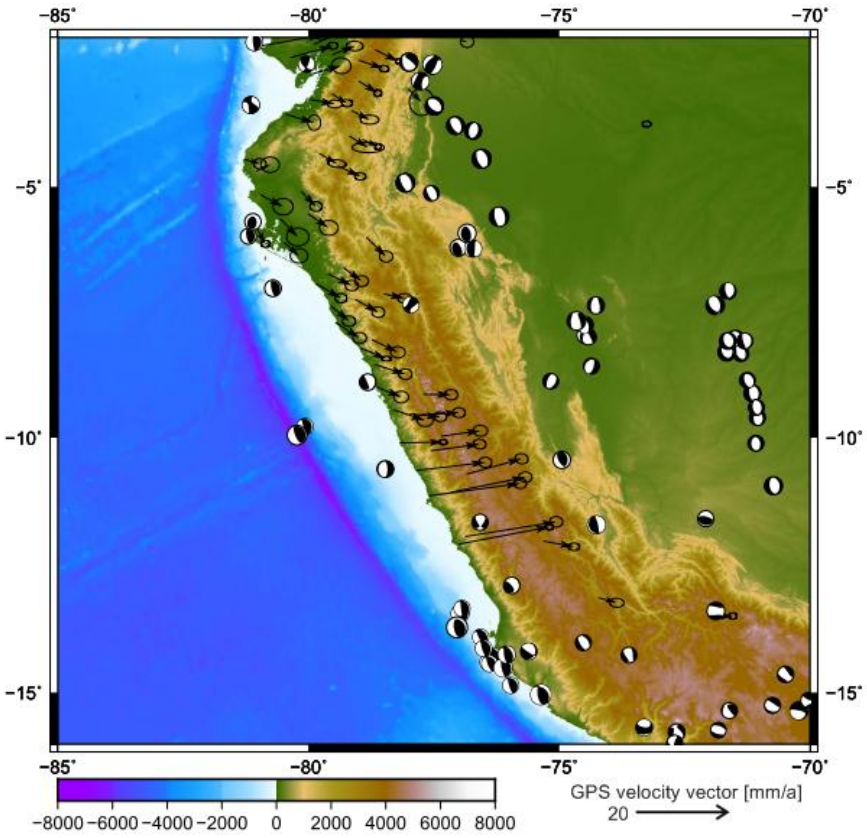

Figure 2.4. GPS data (compiled from Veloza, et al. (2012)) and focal mechanisms (from Harvard CTM database, years 1900 to 2014) for earthquakes above magnitude 5 in the northern Central Andes.

Focal mechanisms for earthquakes above magnitude 5 between 1900 and 2014 (from Harvard CTM database) are shown in Figure 2.4 together with GPS data compiled from Veloza, et al. (2012). The seismic zone is planar with small dip angles of 10° to 15° at intermediate depth up to 200 km (Isacks and Molnar, 1971). Beneath this depth, seismic activity decreases significantly resulting in a seismic gap until depths of 500 km. Here, earthquake centers form two almost parallel belts beneath Argentina and western Brazil, respectively (Isacks and Molnar, 1971). Intense intermediate-depth seismic activity at the

Peru Chile border (approx. 15° S) reflects with a higher dip angle (of 28°) a change in tectonic configuration. Also, the earthquakes are in alignment with the volcanoes of the Central Volcanic Zone south of the PFSS (Isacks and Molnar, 1971).

Interseismic deformation (Figure 2.4) shows high (up to 20 mm/a) inland, slightly northward, tending velocities along the center part (approx. 10° S to 13° S) of the flat slab margin. In the northern part (approx. 6° S to 10° S) velocities are rather low (5 mm/a) and clearly south-eastward tending. GPS solutions of the northern part of the PFSS match well in orientation and magnitude with the observed sliver movement (Nocquet, et al., 2014). The proximity of the increase in magnitude and change in direction coincides to the location of the Mendaña fracture zone (Figure 2.4) suggests an influence of this seawards propagating active spreading center (Huchon and Buorgois, 1990) on the dynamics of the continental margin.

The obliquity angle and plate motions of the PFSS is disputed: representations include an almost symmetric scenario to the NVZ with about 40° obliquity (e.g. Ramos, 1999; Velosa, et al., 2012; Pulido, et al., 2014); while others (e.g. Knezevic Antonijevic, et al., 2015; Yepes, et al., 2016) estimate the obliquity angle to be rather small (10°-20°). The influence of the obliquity angle on the deformation of the overriding plate is insignificant. In the PFSS is, instead of a fast moving sliver – such as in the NVZ, the Inca sliver observed (Nocquet, et al., 2014). This sliver moves with approx. 0.5 cm/a south-eastward along the plate margin in the same direction as the Nazca Ridge (Berrocal and Fernandez, 2005; Nocquet, et al., 2014).

3 Theoretical background and numerical modelling

3.1 Governing geodynamic equations

The description of deformation and flow of earth materials is a fundamental part of many branches of earth sciences and an integral to numerical models that replicate the deformation of the Earth. Due to changes in temperature, pressure, composition, and other factors, Earth's layers cannot be treated the same way, thus different rheological behavior plays a significant role in geodynamics. For example, the asthenosphere can be considered viscous on long times scales (thousands to millions of years), whereas on short geological time scales (up to thousands of years) the lithosphere behaves elastically. The crust is better described as plastic due to the fracturing and faulting of upper crustal rocks (Turcotte and Schubert, 2014).

Aiming for a numerical model of the dynamics of a subduction zone, one must consider the fundamental physical concepts of equilibrium and conservation. Equations of equilibrium state that a body is in balance when all forces acting upon it are balanced. Conservation equations require that a system is neither losing nor gaining mass, momentum or energy over time. These two concepts are closely linked to each other.

A body in equilibrium or force balance must fulfill the following condition, expressed using the stress tensor $\sigma_{ij}, (i, j \in \{1,2, \dots, n\}, n \in \mathbb{N})$, the density ρ and the body forces X_i, $(i \in \mathbb{N})$:

$$\frac{\partial \sigma_{ij}}{\partial x_j} + \rho X_i = 0 \tag{3.1}$$

In the three-dimensional space $\mathbb{R}^3$ with a Cartesian coordinate system (x_1, x_2, x_3) where the x_3-axis is vertical and pointing upwards, the body forces reduce to $X_1 = X_2 = 0;\ X_3 = -g$, where g is the gravitational acceleration. The component equations of equilibrium in a 3D continuous medium can thus be written as:

$$\frac{\partial \sigma_{11}}{\partial x_1} + \frac{\partial \sigma_{12}}{\partial x_2} + \frac{\partial \sigma_{13}}{\partial x_3} = 0 \tag{3.2a}$$

$$\frac{\partial \sigma_{21}}{\partial x_1} + \frac{\partial \sigma_{22}}{\partial x_2} + \frac{\partial \sigma_{23}}{\partial x_3} = 0 \tag{3.2b}$$

$$\frac{\partial \sigma_{31}}{\partial x_1} + \frac{\partial \sigma_{32}}{\partial x_2} + \frac{\partial \sigma_{33}}{\partial x_3} = \rho g \tag{3.2c}$$

In order to solve this first system of equations of stress (Equation 3.2), the rheological properties of the materials need to be considered. This is included in the second set of governing equations, the equations of conservation.

In classical mechanics, i.e. not quantum or relativistic mechanics, neither mass, momentum or energy can be lost over time and need to be conserved. This leads to the fundamental conservation equations of mass, momentum and energy in their most general form

$$\frac{\partial M}{\partial t} = 0 \tag{3.3a}$$

$$\frac{\partial P}{\partial t} = 0 \tag{3.3b}$$

$$\frac{\partial U}{\partial t} = 0 \tag{3.3c}$$

where M is mass, P is momentum, U is energy, and t is time.

In the following, I provide a short introduction to these governing equations of conservation and a brief overview of different deformation behavior of rocks. For further details refer to Turcotte and Schubert (2014) or Gerya (2010), for example.

3.1.1 Continuity equation (conservation of mass)

The continuity equation states that the mass and volume of a body do not change when its shape or position changes over time. In mechanics, such a change can be formulated with respect to one single chosen and kept particle (the reference is moving with the particle) or for a chosen and kept point within the material (the reference is fixed). These two different ways are represented by the Lagrangian (reference is fixed on particle) and by the Eulerian (reference is fixed on space) formalism. Although the numerical modelling software used in this study is an Eulerian finite element code, the conservation equations are for completeness presented in both reference concepts.

For a fixed space (Eulerian) reference frame, the general equation of conservation of mass (Equation 3.3a) relates the local velocity $\bar{v}$ and the local density ρ to the Eulerian time derivative $\partial/\partial t$:

$$\frac{\partial \rho}{\partial t} + \mathrm{div}(\rho\, \vec{v}) = 0 \tag{3.4}$$

The divergence div, defined as a scalar function over a vector field $\vec{v}$, gives $\frac{\partial v_x}{\partial x} + \frac{\partial v_y}{\partial y} + \frac{\partial v_z}{\partial z}$ in a three dimensional Cartesian coordinate system. This means that Equation 3.4 can also be written as

$$\frac{\partial \rho}{\partial t} + \rho \left(\frac{\partial v_x}{\partial x} + \frac{\partial v_y}{\partial y} + \frac{\partial v_z}{\partial z} \right) = 0 \tag{3.5}$$

For one moving point in space (Lagrange) the same condition of conservation of mass is written as

$$\frac{D\rho}{Dt} + \text{div}(\rho\, \vec{v}) = \frac{D\rho}{Dt} + \rho \left(\frac{\partial v_x}{\partial x} + \frac{\partial v_y}{\partial y} + \frac{\partial v_z}{\partial z} \right) = 0 \tag{3.6}$$

where $\frac{D\rho}{Dt}$ the Lagrangian time derivate expressing changes in density with time at one point).

The time derivatives of the two reference systems can be compared when performing a transformation of the Eulerian continuity equation (details given in Gerya, 2010). Doing so, one ends up with the following equation,

$$\frac{D\rho}{Dt} = \frac{\partial \rho}{\partial t} + \vec{v}\ \text{grad}\ (\rho) \tag{3.7}$$

which includes an additional term, $\vec{v}$ grad (ρ), the advective transport, reflecting changes of density in an fixed (Eulerian) point. The gradient grad, defined as a differential operator over a scalar field ρ, gives $\frac{\partial \rho}{\partial x} + \frac{\partial \rho}{\partial y} + \frac{\partial \rho}{\partial z}$ in a three dimensional Cartesian coordinate system. Now, for many geological media (such as for example the Earth's crust and mantle) an incompressibility condition is applied. This means, that the density of material points does not change with time. In other words, the Equation 3.7 needs to fulfill this requirement:

$$\frac{D\rho}{Dt} = \frac{\partial \rho}{\partial t} + \vec{v}\ \text{grad}\ (\rho) = 0 \tag{3.8}$$

This is valid, when temperature and pressure do not change or the change is neglectable small and no phase transformations (leading to change in volume) occur. In these situations one can apply the incompressible continuity equation

$$\text{div}\ \vec{v} = 0 \tag{3.9}$$

for both, Lagrangian and Eulerian formulations. This incompressible continuity equation is often used in numerical geodynamic experiments, which can be a big simplification or a numerical necessity. As later discussed in Chapter 3.2.2, the incompressibility can also be bypassed with a penalty factor, which assumes material to be nearly incompressible.

3.1.2 Stokes flow (conservation of momentum)

The momentum equation relates forces acting on a medium to its deformation or acceleration. This is expressed using the stress tensor $\sigma_{i,j}, i,j \in \{1,2,..,n\}, n \in \mathbb{N}, n = 3$ in three dimensions, density ρ, gravity g_i and velocity field v_i.

$$\rho\left(\frac{\partial v_i}{\partial t} + v_j\frac{\partial v_i}{\partial x_j}\right) = \frac{\partial \sigma_{ij}}{\partial x_j} + \rho g_i \tag{3.10a}$$

$$\rho\frac{Dv_i}{Dt} = \frac{\partial \sigma_{ij}}{\partial x_j} + \rho g_i \tag{3.10b}$$

in Eulerian (Equation 3.10a) and Lagrangian (3.10b) form, respectively. This equation can be seen as similar to Newton's second law of motion $F = m \cdot a$, where F is the net force applied on a medium and $a = \frac{Dv_i}{Dt}$ the acceleration or deformation of the medium.

Flow of viscous fluids is described by the Navier-Stokes equation, which is an expression of conservation of momentum (Equation 3.10b) assuming conservation of mass. The Navier-Stokes equation can also include body properties such as incompressibility (Equation 3.9) and material acceleration. Assuming a constant Newtonian viscosity, the Navier-Stokes equation is

$$-\frac{\partial p}{\partial x_j} + \eta\frac{\partial^2 v_j}{\partial x_i \partial x_j} + \underbrace{\frac{1}{3}\eta\frac{\partial^2 v_k}{\partial x_j \partial x_k}}_{ICF} + \rho g_i = \underbrace{\rho\frac{Dv_j}{Dt}}_{MA} \tag{3.11}$$

where p is the hydrostatic pressure, η is the viscosity and $\frac{D}{Dt}$ expresses the total derivation as introduced in Equation 3.6. For geological materials, material acceleration (MA) can be neglected and the Navier-Stokes Equation 3.11 reduces to the Stokes equation:

$$-\frac{\partial p}{\partial x_j} + \eta\frac{\partial^2 v_j}{\partial x_i \partial x_j} + \underbrace{\frac{1}{3}\eta\frac{\partial^2 v_k}{\partial x_j \partial x_k}}_{ICF} + \rho g_i = 0 \tag{3.12}$$

Additionally, with the incompressibility assumption (Equation 3.9) the term for incompressible fluids (ICF, Equation 3.11 and 3.12) drops out and the Stokes equation simplifies to:

$$-\frac{\partial p}{\partial x_j} + \eta \frac{\partial^2 v_j}{\partial x_i \partial x_j} + \rho g_i = 0 \tag{3.13}$$

This simplified form is mostly used in numerical models studying deformation of the Earth.

3.1.3 Heat transfer (conservation of energy)

The change of energy of a medium is determined by the local heat added to the system (advective and conductive heat transport) and by the energy or heat produced by the system (heat production),

$$\underbrace{\rho C_p \frac{DT}{Dt}}_{change\ in\ temperature} = \underbrace{-\frac{\partial q_i}{\partial x_i}}_{heat\ added/released} + \underbrace{H}_{heat\ produced} \tag{3.14}$$

with q_i being the heat flux, C_p the heat capacity, H volumetric heat production and T is temperature. Applying Fourier's law, $q_i = -k\frac{\partial T}{\partial x_i}$, one gets the following for a three-dimensional medium

$$\rho\, C_p \frac{DT}{Dt} = \frac{\partial}{\partial x}\left(k\frac{\partial T}{\partial x}\right) + \frac{\partial}{\partial y}\left(k\frac{\partial T}{\partial y}\right) + \frac{\partial}{\partial z}\left(k\frac{\partial T}{\partial z}\right) + H \tag{3.15}$$

where k is thermal conductivity. Equation 3.15 is the Lagrangian form of the heat transport equation and by using the relation expressed in Equation 3.8, one can rewrite Equation 3.15 in Eulerian form as

$$\rho\, C_p \left(\frac{\partial T}{\partial t} + \vec{v} \cdot grad\,(T)\right) = \frac{\partial}{\partial x}\left(k\frac{\partial T}{\partial x}\right) + \frac{\partial}{\partial y}\left(k\frac{\partial T}{\partial y}\right) + \frac{\partial}{\partial z}\left(k\frac{\partial T}{\partial z}\right) + H \tag{3.16}$$

The system of conservation equations of mass (Equation 3.4), momentum (Equation 3.10a) and energy (Equation 3.14) are the second set of important equations that must be solved to consider deformation of the Earth. Owing to its dependence upon the stress tensor σ_{ij}, the conservation of momentum equation also depends on rheological properties.

3.1.4 Nonlinear viscosity

Viscosity measures the resistance to deformation or the creep of a fluid. In contrast to elastic deformation, viscous deformation is non-recoverable and the body will remain in its new shape even after the load is removed (Figure 3.1c). Over long time scales, rocks can be treated as highly viscous fluids.

Viscous behavior is independent from strain, but stress in a viscous fluid is a function of strain rate. The stress-strain-rate relation has the form

$$\dot{\epsilon} = A\sigma^n \tag{3.17}$$

The proportionality coefficient A is a function of temperature and pressure, among other factors. The exponent $n \in \mathbb{R}^+$ is a constant: $n = 1$ refers to Newtonian viscous deformation, where stress is linearly dependent on strain rate; for $n > 1$ deformation is referred to as non-Newtonian. In the Earth, there are mainly two different types of viscous creep. In high temperature environments with low stress conditions Newtonian behavior dominates. In moderate temperature and high stress the material behaves as a non-Newtonian fluid and is described with equation 3.17, the power-law creep equation, typically with an exponent around $n = 3$. Figure 3.1 shows the stress-strain-rate diagrams of a Newtonian (a) and non-Newtonian (b) fluid.

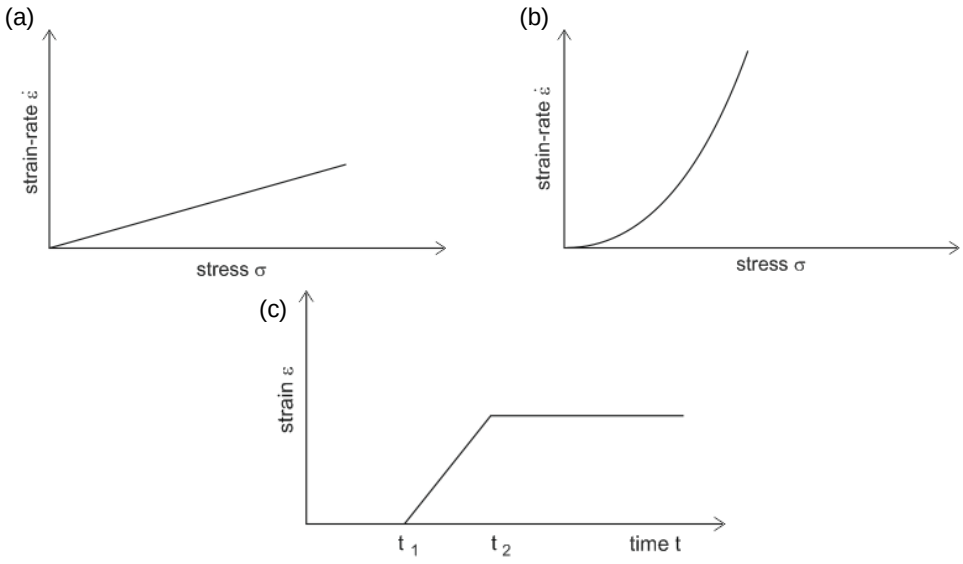

Figure 3.1. Deformation behavior for viscous fluid: (a) Stress-strain-rate diagram for a Newtonian fluid; (b) Stress-strain-rate diagram for a Non-Newtonian behavior with Power law coefficient $n = 3$; (c) Strain-time diagram, loading starts at time t_1 and ends at time t_2, while the strain ϵ remains.

Additionally, temperature is directly influencing viscosity: increase in temperature causes a decrease of resistance which results in a lower viscosity and vice versa.

The deformation of viscous fluids is described by the Navier-Stokes equation (see Chapter 3.1.2), which expresses conservation of momentum under the assumption of conservation of mass.

3.1.5 Frictional plasticity

Materials behaving as an elastic body fail at a certain critical or yield stress and deformation becomes irreversible. This critical value of yield stress or strength σ_y depends on many factors such as the material examined and pressure. After the yield strength is exceeded, the body may either fracture (brittle behavior) or experience plastic flow (ductile behavior). In the first case, the stress drops to zero when the yield stress is reached (Figure 3.2a); in the latter case, stress remains ideally constant with increasing stress at yield strength (Figure 3.2b; ii). When yield stress increases with increasing deformation, one refers to strain hardening (Figure 3.2b; i) and to strain softening (Figure 3.2b; iii) when the opposite is the case.

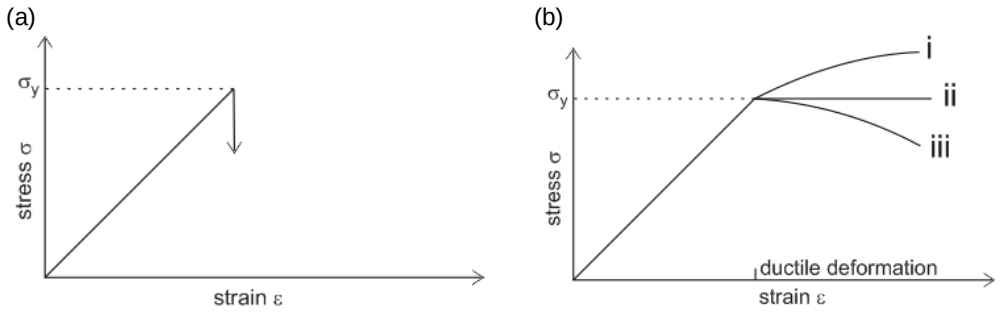

Figure 3.2. Strain-stress diagram for plastic behavior: (a) in theory, stress drops to zero (arrow) due to brittle failure when yield stress σ_y is reached, (b) in perfect plastic flow, stress is constant after the yield stress is constant (ii) and in cases of strain hardening (i) or softening (iii) yield stress increases or decreases, respectively.

The general form of a yield function for a plastic material is

$$F = \sigma - \sigma_y = 0 \tag{3.18}$$

which expresses that plastic deformation occurs when $\sigma = \sigma_y$. The two of the most commonly used criteria for plastic deformation in geoscience are the Mohr-Coulomb and Drucker-Prager criteria (Gross and Seelig, 2011). The Mohr-Coulomb criterion is commonly used for description of rock failure and is also used in this study to represent the plastic deformation of the materials applied. The yield function F_{MC} for the Mohr-Coulomb yield criterion is

$$F_{MC} = \sigma_n \tan\varphi + c - \tau = 0 \tag{3.19}$$

where τ the shear strength, σ_n the normal stress, φ the dimensionless angle of internal friction and c the cohesion. The shear strength and normal stress are expressed with normal vectors to the plane of interest and thus independent of the coordinate axes used. Defining the normal vector to

$$n = n_1 e_1 + n_2 e_2 + n_3 e_3 \tag{3.20}$$

with e_1, e_2, e_3being the assigned base vectors the normal stress σ_n takes the form

$$\sigma_n = n_1^2\sigma_1 + n_2^2\sigma_2 + n_3^2\sigma_3 \tag{3.21}$$

and the shear strength is expressed as

$$\tau = \sqrt{(n_1\sigma_1)^2 + (n_2\sigma_2)^2 + (n_3\sigma_3)^2 - \sigma^2} \tag{3.22}$$

Using the usual expression (Equation 3.19) this allows the evaluation of the Mohr-Coulomb criterion for six planes of maximum shear stress.

Alternatively, using the relations between the mean stress $\sigma_m = (\sigma_1 + \sigma_3)/2$ and the maximum shear strength $\tau_m = (\sigma_1 - \sigma_3)/2$ given by the position and radius of the Mohr's circle (Figure 3.3)

$$\sigma = \sigma_m - \tau_m \sin(\varphi) \tag{3.23a}$$

$$\tau = \tau_m \cos(\varphi) \tag{3.23b}$$

where σ_1 the maximum and σ_3 the minimum principle stresses, the Mohr-Coulomb criterion is expressed as

$$\tau_m = \sigma_m \sin(\varphi) + c \cos(\varphi) \quad (3.24)$$

For deformation of fluids, pressure can generally substitute for mean stress in Equation 3.24. This gives an expression of the shear strength dependent on pressure, cohesion and the friction angle.

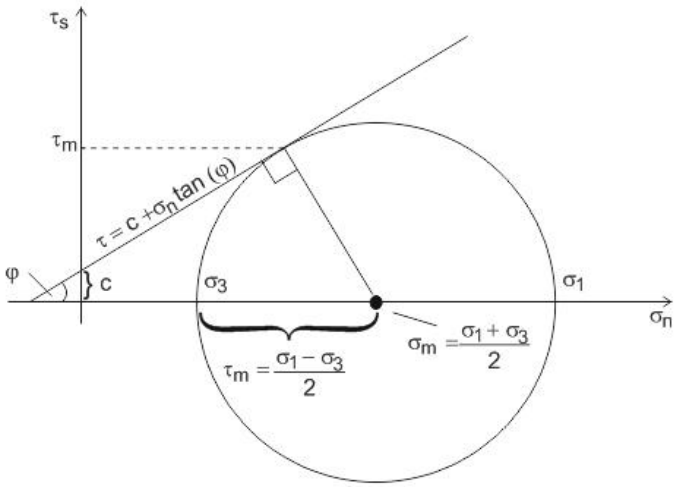

Figure 3.3. Mohr's circle is a graphical representation of the Coulomb criterion relating mean stress σ_m, maximum shear strength τ_m and maximum σ_1 and minimum σ_3 principle stresses as well as angle of internal friction φ and cohesion c.

The angle of internal friction φ in Equation 3.19 and 3.24 is referring to shear stress and normal effective stresses at which shear failure occurs. A larger angle of internal friction describes a stronger material (see also Figure 3.3). For example, $\varphi = 30°$ is a common value for dry sand. In purely mechanical models the friction angle can be used to 'artificially' weaken certain materials or areas within a material.

Fracturing and plastic flow (i.e. brittle and ductile behavior) are important in the mechanics of the upper lithosphere and determines the occurrence of earthquakes and mountain building, breaking, folding and faulting. A typical tool to investigate and compare the strength of the lithosphere is a strength profile, which plots the differential stress (i.e., the difference between the largest and smallest principal stresses) of a chosen rock type against the depth. In diagram (Figure 3.4) is the ductile strength cutting in exponential curve (compare Figure 3.2b) through the line representing brittle strength (compare Equation 3.19). The intersections mark the transition between brittle and ductile deformation. The resulting shape presents the maximum strength related to depth.

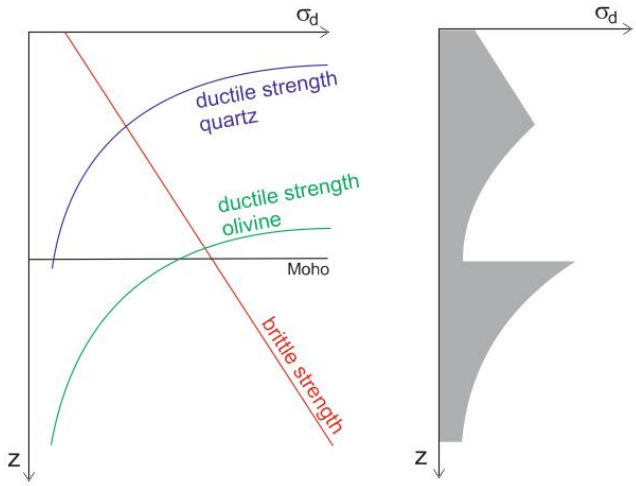

Figure 3.4. Example of a strength envelope: (a) ductile strength (blue and green) curves for quartz and olivine, respectively and brittle strength line (red); (b) resulting strength envelope.

3.2 Numerical modelling software

In the past, mostly two dimensional Earth models were available (apart from a few exceptions e.g. Braun, 1993, 2008; Ji et al., 2015); mainly due to lack of computational power. Two dimensional models are not capable of taking into account plate tectonic processes and deformation of continents at a sufficiently high resolution or cannot overlook three dimensional problems, like oblique motion. Central questions regarding potential couplings and feedbacks between tectonics, erosion and climate can thoroughly be investigated only by applying full three dimensional models.

3.2.1 General overview of the software

The numerical modelling software used in this study is DOUAR ("Earth" in the Breton language), an Eulerian 3D finite-element code for viscous-plastic creeping flows. The code DOUAR is designed to address 3D flow problems of crustal to mantle scale and solves the momentum and energy equations to determine material deformation (velocity field) and temperature evolution, providing useful geological predictions of surface uplift and strain rate variations in the lithosphere, among other outputs. Below I describe the main elements of the software that are relevant to this thesis. A detailed code description is given in Braun et al. (2008).

The Finite Element Method (FEM)

The equations describing a body's deformation, movement, change in properties and behavior are a complex system of equations that vary throughout the body and which require numerical methods to be solved. The numerical solution to partial differential equations is a matter of finding a stable approximation to the solution that stays within an acceptable range of error. Thus, the error must not propagate and amplify, which would make the data and calculations unusable. There are different approaches to solve such systems of equations. The most popular are the Finite Difference Method, Discrete Element Method and the Finite Element Method (FEM). DOUAR uses the FEM and a brief introduction to this method is given here. The FEM is often preferred over the other methods as it is especially suited for complex geometries, where some areas need higher resolution than others.

When using the FEM, the model domain or body is divided into a finite number of pieces of simple geometric form – the ´finite elements´. These elements (triangles, rectangles, etc.) do not necessarily have the same shape or size and are defined by nodes in their corners, edges and/or inside the element. In the FEM, it is assumed that the solution of the partial differential equations (here the components of the velocity and (in cases where it is enabled) the temperature field) can be approximated by their values at a finite number of "nodal" points. To provide values between the nodes, each element has a shape function Φ_i which defines the values of functions inside the element by using the values F_i at their nodes. The function for one element thus has the form

$$F(x) = \sum_{i=1}^{N} \Phi_i(x) F_i \tag{3.25}$$

where N is the number of nodes. The shape functions Φ_i can easily be calculated based on their simple geometry and predefined boundary conditions. For example, increasing the number of elements (i.e., dividing the elements into a larger number of smaller, geometrically simpler elements) provides more accurate solutions. However, a larger number of nodes increases the degree of freedom and thus requires a higher computational time. The user thus needs to find a compromise between accuracy and computational time.

Octree division of space

All calculations in DOUAR are done within a unit cube: the entire geological system is scaled to fit within a 1x1x1 dimensionless cube. This restricts the models basal extent to being squared. In the vertical direction, the model thickness can be adjusted by defining the position of a free surface boundary, where elements above the free surface are excluded from the calculation.

The octree concept (Meagher, 1980) is applied on the unit cube, which means that the unit cube is discretized by dividing it into eight equally sized smaller cubes. Theoretically, also non-uniform discretization is possible, but problematic with plasticity in DOUAR and thus not applied here. Further division of all the eight cubes into eight smaller ones and so forth

yields higher spatial resolution. The unit cube is defined as an octree of level zero with one leaf. After one division eight leaves are counted at refinement level one. The standard grid refinement level is five with 32 768 leaves. This calculation is following the equation

$$number\ of\ leaves = (2^{level})^3 \tag{3.26}$$

The leaves of the defined level of discretization are used as finite elements in an Eulerian reference frame (reference is fixed in space) with which the partial differential equations are solved.

Octrees are simple, memory-efficient tools for defining the location of nodes and elements. For example, to create a leave at level L around a point of known coordinates, L conditional statements are needed. When using the though simple scheme to store an octree, operations on the nodes become relatively costly. A refinement in height is achieved by scaling the element height with an additional, so called exaggeration factor. This increases the vertical refinement level while the horizontal components (x, y) remain in the original refinement.

Arbitrary Lagrangian-Eulerian (ALE) Method

In order to track the computational mesh, the so called arbitrary Lagrangian-Eulerian (ALE) Method is applied. Similar to the idea of change of reference frame when describing the equations of conservation (Chapter 3.1.1 – 3.1.3), the computational mesh can be changed. In the Lagrangian algorithm each individual node of computational mesh follows the associated material particle during motion, while in Eulerian algorithms the computational mesh is fixed and the particles move with respect to the grid. In the ALE algorithm, the nodes of the computational mesh may be fixed or, alternatively, move some arbitrarily defined way. This allows the handling of greater distortions in a higher resolution than would be in cases only one of the methods would be applied. Even though, DOUAR is strictly in the Eulerian reference frame regarding space discretization described above (Octree division of space), it is handling cloud particles in the Lagrangian reference frame.

Materials, surfaces and the particle cloud

Materials are defined with their properties as, e.g., density, viscosity, diffusivity and heat capacity. Due to DOUAR operating in the unit cube, all material properties need to be scaled with respect to the unit length. This is based on the requirement that the ratio between ‘nature’ and ‘model’ always needs to be the same and is accompanied by other scaling, such as time, velocity, viscosity and so on. One material is chosen as reference (often the mantle) and all other materials and their properties are scaled with respect to the reference values. Each material used in the experiment is assigned a material number, which refers to the respective scaled properties.

In the original version of DOUAR, surfaces are used to define material boundaries. Now, surfaces are only used to initially describe areas to which a certain material number is assigned. The material properties behind the material number are then stored on cloud particles and the surfaces – except the uppermost, free surface defining the vertical extent of the model domain – are discarded. Material properties for the material above the free surface are chosen such that the density corresponds to material properties of air. This defines a void space not filled with cloud particles and the area is excluded from calculations. The free surface can either be fixed and not allowed to change its shape during the run or be allowed to move freely in response to uplift, gravitation, and/or erosion and sedimentation.

The storage of material properties on the Lagrangian cloud (this means the reference frame for the cloud is fixed on the particles) is based on the particle-in-cell method (Gerya, 2010), which handles advection of the particles. The density of cloud particles in the octree is dynamically adjusted to maintain a balance between accuracy and efficiency (computational cost). Usually, the number of cloud particles in one leaf is limited to be between minimum and maximum bounds for the leaves (often 8 and 27, respectively). When a new particle is injected, the code performs a 'selection of ten': ten particles are injected, of which only one located furthest away from the existing particles is kept. To associate the new particle with data (e.g., strain at that position) the (strain) values from existing particles are interpolated onto the nodes of the octree and back onto the new particle. The injected particle receives its material properties based on a majority rule and gets the material number most of the particles in the element have. At the end of each time step, particles are moved following the calculated velocity solution. If there are too many particles in the leaf, the requisite number of particles is removed.

Code execution steps

The main input values for use of DOUAR include model domain dimensions, surface geometry and material properties. The run time is chosen and the time stepping is defined so that the largest distance a cloud particle could travel in one time step is not greater than one third of the length between two nodes. This is known as the Courant–Friedrichs–Lewy (CFL) condition (Courant, Friedrichs and Lewy, 1928.) and is necessary for convergence while solving partial differential equations numerically. Further, velocity and temperature boundary conditions are prescribed.

The code starts time stepping: surfaces are refined, thermal systems solved and the system adjusted according to current solutions. DOUAR performs linear (grid) iterations and nonlinear (velocity) iterations. First, linear iterations determine grid geometry (octree level, box refinement, and free surface position). Nonlinear iterations are used to calculate the velocity field. Both iterations need to converge before the code continues with the increment time step. After each step velocity, geometry and geothermal data is written out. After the last defined time step, the code cleans up and closes files.

CASCADE surface process model

In order to include climate response (e.g., erosion and sedimentation processes) DOUAR can be linked with the CASCADE surface process model. CASCADE was originally designed for river erosion and a detailed description of the software can be found in Braun and Sambridge (1997, 2001). In this study, river erosion is not used. Instead, I used the ability to simulate hillslope diffusion for the uppermost surface in test runs that included a freely moving upper surface. In these runs, diffusion processes were meant to prevent the formation of sharp and overly steep artefacts on the surface, which can lead to Delaunay triangulation errors or velocity field solution errors. Unfortunately, surface diffusion did not eliminate these artefacts, so the free surface was fixed in the experiments in this thesis.

3.2.2 Implementation geodynamic equations

The general equations of conservation have been briefly introduced in Chapter 3.1. Here, I describe how they are handled in DOUAR.

Incompressibility condition

Commonly, the lithosphere and underlying mantle are treated as highly viscous materials in geodynamic models. Deformation in these materials occurs at such slow rates that inertial forces are neglected. This means also that flow is normally laminar and thus the Reynolds number insignificant. Further, it is assumed that heat is conducted faster than it is dissipated by the viscous flow (infinite Prandtl number). However, as energy and momentum are preserved in the system, physical quantities such as velocity can be found using the Navier-Stokes equation (cf. Equation 3.11). In the code a simplified form (and condition $MA = 0$; Equation 3.12) is used:

$$-\operatorname{grad} p + \operatorname{div} \eta \left(\operatorname{grad} v + \operatorname{grad} v^T\right) = \rho g \tag{3.27}$$

where η is shear viscosity, p is pressure, ρ is density, v the velocity and g the gravitational acceleration.

The incompressibility assumption (cf. 3.1.1 Continuity equations) requires the divergence of the velocity to be zero:

$$\operatorname{div} v = 0 \tag{3.28}$$

However, in DOUAR an approximation for the incompressibility is made: the material is assumed to be *nearly* incompressible and a so called penalty factor λ is introduced:

$$-\lambda \operatorname{div} v = p \tag{3.29}$$

The penalty factor λ has the dimensions of viscosity ($Pa \cdot s$) and is commonly chosen to be by eight factors lager than the shear viscosity η; this ensures the nearly incompressible behavior for the material and also allows the pressure to be calculated directly from the velocity solution.

For high temperatures, the viscosity η is non-linear (i.e., non-Newtonian) and depends on the strain rate $\dot{\varepsilon}$ and temperature T:

$$\eta = \eta_0 \dot{\varepsilon}^{\frac{1}{(n-1)}} e^{\frac{Q}{nRT}} \tag{3.30}$$

where Q the activation energy and R the Boltzmann gas constant. The constant n is chosen according to (empirically) found material properties.

3.3 Strain partitioning at obliquely convergent margins

In the northern and central Andes, subduction zones with different geometries are present. In the northern part, the NVZ (5°N-3°S), subduction is oblique with a relatively steep subduction angle, a weakness present in the continent (e.g., the volcanic arc and/or major fault systems/shear zones) and strain partitioning is observed. In the Peruvian flat slab segment to the south, the PFSS (3°S-14°S), less oblique plate convergence is combined with a flat-slab style of subduction, a lack of volcanic activity or other well-defined continental weakness, and no significant strain partitioning is observed. Although the NVZ and the to the south adjacent PFSS both experience continental sliver movement, the strain partitioning in the NVZ is more pronounced with velocities twice as high (e.g. Noquet et al., 2014, Yepes, et al., 2016).

A schematic illustration of both of these cases, strain partitioning with sliver movement as observed in the NVZ and an oblique thrusting case as observed in the PFSS, is shown in Figure 3.5.

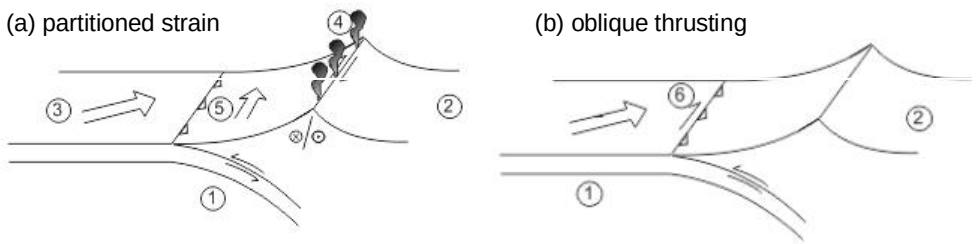

Figure 3.5. Dynamics in an oblique subduction zone: (a) Crustal strain partitioning above an oblique subduction zone. The subducting slab (1) slides underneath the continental plate (2) with movement oblique to the plate margin (3). On the continental side, oblique movement is divided into (right lateral) shear zones (4) and subduction (1). A volcanic arc (4) is observed in vicinity to the fault system. The division of motion is known as strain partitioning and results in a margin parallel moving sliver (5). (b) No partitioning case above an oblique subduction with oblique thrusting at the plate margin (6).

In previous studies, the occurrence of tectonic slivers owing to strain partitioning has been investigated (e.g. Nocquet et al., 2014). Clearly, there cannot be strain partitioning (strike-slip deformation) without oblique subduction, because of the lack of an oblique component in motion. However, an additional primary factor is the interplate coupling and the steepness of subduction of the slab (e.g. Jarrard, 1986; Wortel et al., 1991). The interplate coupling is influenced by many factors, e.g. the age of the plates, temperature regimes and the subduction dip angle. Shallow subduction on the pro-side of the subduction zone might be the cause for strain partitioning being observed in the forearc (accretionary prism) (Bourgois, 2013; Cediel et al, 2003). Even though water-rich sediments might be expected to have very low friction angles, the fault area is very large compared to the thickness of a vertical fault resisting horizontal shear motion because of the low subduction dip angle. This and the prevailing brittle deformation in this shallow depths increases the interplate coupling and the overlying wedge of the continental crust more easily detached from the plate. This is especially true for the sediments of the accretionary prism. Sliver formation in the accretionary prism is however not a matter of further investigation in this work.

In order to better understand the forces acting on the continental plate in an oblique subduction setting, four main shear stresses shown in Figure 3.6 are put in relation to the obliquity angle γ and the subduction angle α in Equations 3.31a-c. Refer to McCaffrey (1992) for a full derivation.

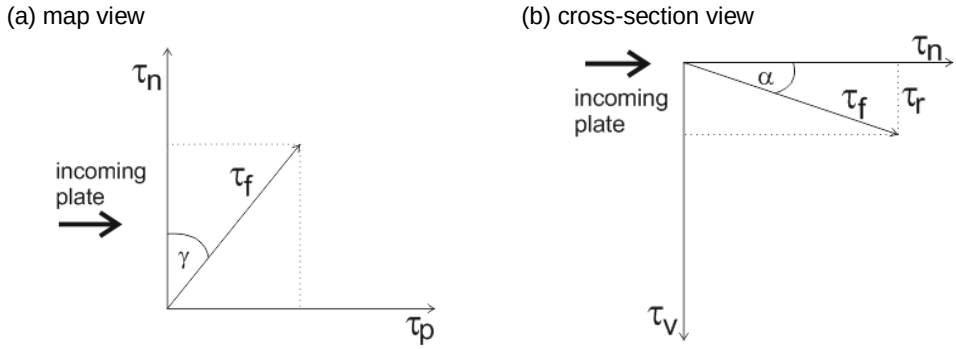

Figure 3.6. Shear stresses acting on the continental plate in an oblique subduction zone with obliquity angle γ and subduction angle α shown in (a) map view and (b) cross-section view. τ_f is the inter plate (or subduction) shear stress between plates, τ_p is the margin parallel shear

stress component, τ_h is the margin normal shear stress component, τ_v is the vertical shear stress component and τ_r is the rear shear stress resisting strike-slip movement in the continent.

With τ_f being the inter plate (or subduction) shear stress between the overriding continental plate and the subduction oceanic plate per unit length the following relations hold true for the margin – parallel (τ_p), the margin – normal (τ_n) and margin – vertical (τ_v) component of the τ_f.

$$\tau_p = \tau_f \cdot \sin\gamma \tag{3.31a}$$

$$\tau_n = \tau_f \cdot \cos\gamma \tag{3.31b}$$

$$\tau_v = \tau_f \cdot \sin\alpha \tag{3.31c}$$

Force is the product of shear stress and the area it acts on. Assuming that the faults resist slip over the same range and that the system is of infinite width, the fault areas (as sketched in Figure 3.7) can be expressed as

$$A_b = 1/\sin\alpha \tag{3.32a}$$

$$A_r = 1 \tag{3.32b}$$

where A_b is the area of the basal thrust and A_r the area of the vertical rear shear zone.

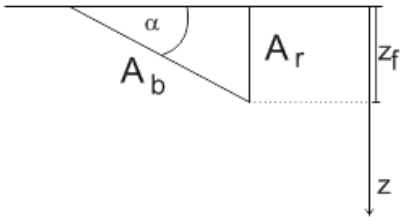

Figure 3.7. Fault areas in a subduction zone. Side view of a subduction zone: A_b is the area of the basal thrust, A_r the area of the vertical rear shear zone, α the subduction sip angle and z_f the depth range of the faults, which scales to unit length one.

With Equations 3.31a and 3.32 one gets the following expressions for the margin – parallel force F_p and the systems rear force F_r

$$F_P = \tau_p \cdot A_b = \tau_f \cdot \frac{\sin\gamma}{\sin\alpha} \tag{3.33a}$$

$$F_r = \tau_r \cdot A_r = \tau_r \tag{3.33b}$$

Slip on the rear shear zone will occur when the margin – parallel force F_P equals (or exceeds) the force resisting shear on the vertical fault system F_r:

$$F_p - F_r = 0 \tag{3.34}$$

The force balance (Equation 3.34) can be expressed with Equations 3.33 and one gets

$$\tau_f \cdot \frac{\sin\gamma}{\sin\alpha} = \tau_r \tag{3.35}$$

Let the angles of obliquity γ and subduction dip α always be between $0°$ and $90°$ and let the subduction and resisting shear stress τ_f and τ_r be arbitrary values for now. Then, one can distinguish two different cases:

(i) fixed obliquity angle γ
(ii) fixed subduction angle α.

Both cases require the system to fulfill Equation 3.35. Case (i) reduces Equation 3.33a to $F_p \propto \tau_f \cdot 1/\sin\alpha$, which means that with increasing subduction dip angle α decreases the force parallel to the margin and with this it decreases the probability for F_P exceeding F_R (Equation 3.34). In other words, sliver movement is less likely for increasing subduction dip angles. Case (ii) reduces Equation 3.31a to $F_p \propto \tau_f \cdot \sin\gamma$. This describes that the margin parallel force increases with increasing obliquity angle γ.

Let now the angles of obliquity and subduction be fixed with $\gamma, \alpha \in [0°, 90°]$. Cases

(iii) τ_r increases/decreases and
(iv) τ_f increases/decreases

describe situations where either the friction between the plates or the resistance at the rear end of the subduction zone in the continent change, for example by weakening of the slab or continental crust. Increase or decrease of the shear stresses τ_r, τ_f is equivalent to increase or decrease of the forces F_r, F_p. If τ_r increases under the assumption that τ_f is fixed (Case (iii)), it is less likely that the margin – parallel force overcomes the resistance. The opposite is also true. If τ_f increases (Case (iv)) Equation 3.33a would suggest an increase in margin parallel force. This however, needs to be considered carefully. Generally it holds true that if the interplate friction increases such that the system locks itself no movement is observed. If the

interplate friction reaches towards zero a sliver would possibly be held back only by the rear end resisting force. However, these considerations do not take any compression or extension forces into account neither weakening of larger areas due to heat transport or other thermo-mechanic processes.

In general and confirmed by above considerations optimal conditions for margin parallel movement are given in a subduction zone system with high obliquity angle γ, small subduction angle α and a small resisting shear stress τ_r.

In order to get a better estimate of the relation between the resisting shear stress τ_r and the subduction shear stress τ_f with regard to rock strength the following steps have been undertaken. Assumed that the forces are not exceeding the yield strength, τ_r and τ_f can be substituted by their maximum shear strength τ_{mR} and τ_{mf} (see Equation 3.24), respectively (Equation 3.35).

$$\tau_r = \tau_f \cdot \frac{\sin\gamma}{\sin\alpha} \tag{3.36a}$$

$$\Rightarrow \quad \tau_{mr} = \tau_{mf} \cdot \frac{\sin\gamma}{\sin\alpha} \tag{3.36b}$$

Now, employing the Mohr-Coulomb criterion with $\tau_{mr} = p_r \sin\varphi_r + c_r \cos\varphi_r$ and $\tau_{mf} = p_f \sin\varphi_f + c_f \cos\varphi_f$ (cf. Equation 3.24), respectively, as it is used in the model the friction angles of the continental crust φ_r and the subduction slab φ_f can be related to the obliquity angle γ of the system. Using values from the experiments presented in this study a friction angle $\varphi_f = 2$ and an obliquity angle varying in the range of $\gamma \in [10°, 50°]$ are assumed. Further, cohesion is only important in the uppermost 1 – 2 km and assuming a cohesionless case, the shear strength equation reduces to $\tau_{mr} = p_r \sin\varphi_r$ and $\tau_{mf} = p_f \sin\varphi_f$, respectively and leaves Equations 3.36b as

$$p_R \sin\varphi_R = p_f \sin\varphi_f \cdot \frac{\sin\gamma}{\sin\alpha} \tag{3.37}$$

Pressure will deviate from lithostatic pressure for different failure types, such as compression or tension (Whipp, et al., 2014) and pressure has been substituted by the shear pressure p_{SS}. Calculations are mainly following the considerations of Whipp, et al. (2014) and the therein established relation

$$p_{R,f} = p_{SS_{R,f}} = \frac{k_{R,f} + k'_{R,f}}{2} p_{lith_{R,f}}, \tag{3.38}$$

where $p_{lith_{R,f}} = \rho_{R,f} g h$ the lithostatic pressure and $k_{R,f}$, $k'_{R,f}$ are coefficients depending on the friction angle. $g = 9.81$ m/s^2 is the gravitational acceleration. Assuming further that the faults resist slip to the same depth, the lithostatic pressure term for the resisting p_{lith_R} and the friction force p_{lith_f} can be canceled out and one is left with

$$\frac{k_R + k'_R}{2} \cdot \sin \varphi_R = \frac{k_f + k'_f}{2} \cdot \sin \varphi_f \cdot \frac{\sin \gamma}{\sin \alpha} \tag{3.39}$$

For any given obliquity angle Equation 3.39 (derived from 3.36a) should hold true if sliver (margin parallel) movement is expected in the continental crust.

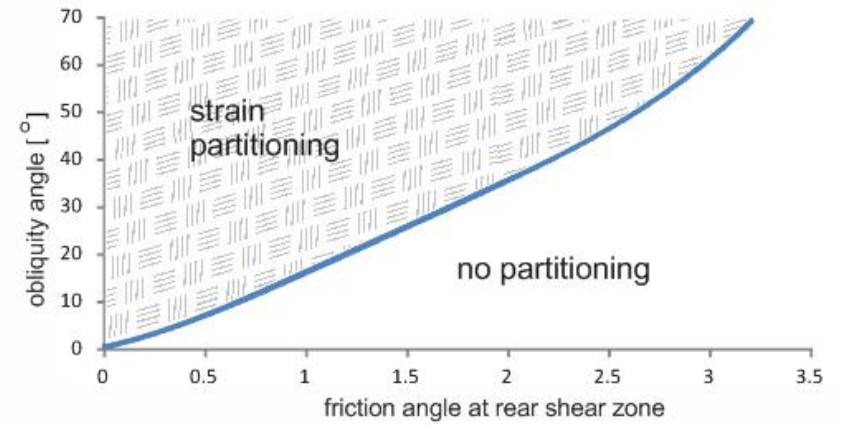

Figure 3.8. Force balance function $f(\varphi_R) = F_R - F_P$ in dependence of friction angle of continental crust φ_R. Sliver movement is expected for combinations of resisting friction angle and obliquity angle above the line. Representation for constant subduction dip angle $\alpha = 35°$ and obliquity angles $\gamma \in [10°, 70°]$.

The graph shown in Figure 3.8 shows that for increasing obliquity angles a weaker resisting shear zone (higher friction angle) is necessary for the margin parallel force F_P to overcome the shear resistance force F_R and to initiate strain partitioning. For an obliquity angle of $\gamma = 35°$ a friction angle of $\varphi_R \approx 2.2$ and less is necessary to initiate sliver movement in the continental crust. For an obliquity angle of $\gamma = 20°$ a noticeable weaker continental crust is necessary, the value reduces to $\varphi_R \approx 1.2$. However, one needs to keep in mind that these calculations are considering only two of the forces acting on the subduction zone and also exclude the influence of temperature. It is however a useful tool to approximate the weakness in the continental crust necessary to overcome resistance of sliver movement.

In order to determine the velocity of a sliver, one can delimit the maximum velocity, which is the velocity of a totally partitioned system. A simple vector calculation of the incoming velocity v_{in} and the obliquity angle γ, as shown in Figure 3.9a, gives the fully partitioned velocity pointing parallel to the margin v_p and the velocity component pointing northward of fully partitioned velocity v_n

$$v_p = v_{in} \cdot \sin(\gamma) \tag{3.40a}$$

$$v_n = v_p \cdot \cos(\gamma) \tag{3.40b}$$

The plot in Figure 3.9b shows the fully partitioned velocity components against obliquity angles for $v_{in} = 7cm/a$.

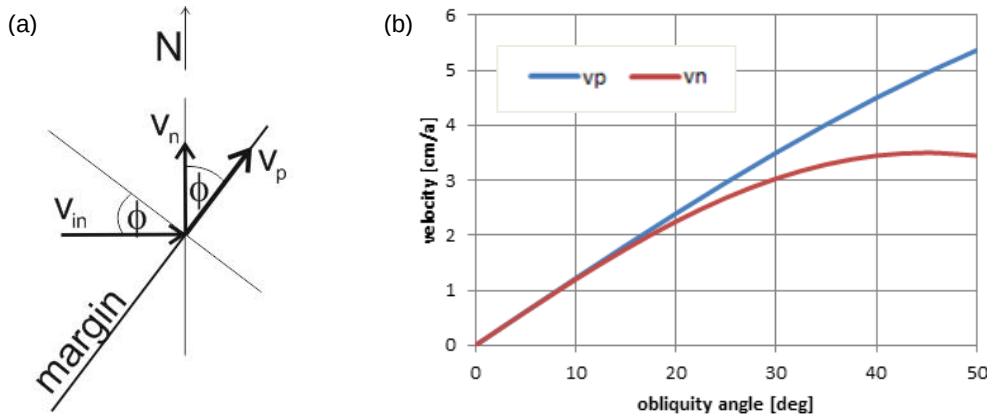

Figure 3.9. Velocities at an oblique plate margin: (a) velocity components in an oblique setting: v_{in} the total incoming velocity, v_p the margin parallel and v_n the northward pointing velocity component of a fully partitioned system; (b) diagram plotting velocity components of a fully partitioned system against obliquity angles for $v_{in} = 7cm/a$.

For a relative subduction velocity of 7cm/a and an obliquity angle of 40°, a fully partitioned system would be expected to show up to 3.5 cm/a of northward pointing and 4.5 cm/a margin parallel velocity components (Figure 3.9b). However, a fully partitioned system is based on observations (e.g. Nocquet, et al., 2014; Mora-Páez, et al., 2016) not expected for the NVZ nor the PFSS.

Case Study I – Mechanical modelling of oblique subduction in the Northern Volcanic Zone (5°N - 3°S)

In order to investigate the dynamics of the oblique subduction of the Northern Volcanic Zone (NVZ, 5°N - 3°S), a numerical model was designed to represent this study area. The main emphasis on this case study lies on 'how does a continental zone of weakness affect the dynamics of the overriding plate'. In addition, several experiments were conducted in order to make further conclusions over the relation between subduction angle, obliquity angle, weakness in the continental crust and strain partitioning.

The runs presented in this case study are performed as purely mechanical experiments. One reason for this is to keep the runs as simple as possible in order to understand the influence of geometric parameters first. The effects of temperature-dependent rock properties on oblique subduction and continental deformation are investigated in Case Study III.

1.1 Model design

The reference model is designed to represent the NVZ of South America with the continental weakness (e.g. a volcanic zone or predefined fault zone) and oblique as well as steep subduction. Figure 1.1 shows the cross section and the top view of this reference model design, defining initial slab geometry, topography, material and velocity boundary conditions.

The model measures a 1600 km times 1600 km base with 160 km depth. The topography is initially defined to coarsely resemble the Andes. This means, from defined land level at a model depth of 5 km the Andes rise with a gradient of 6% to form a 96 km wide to 4 km elevated stripe following the contour of the subduction margin at a distance of about 200 km. This uppermost surface is not allowed to move during any of the runs. This additional feature was tested but chosen to be left out because inclusion of the feature did not result in stable models (see further down: Model assumptions and restrictions).

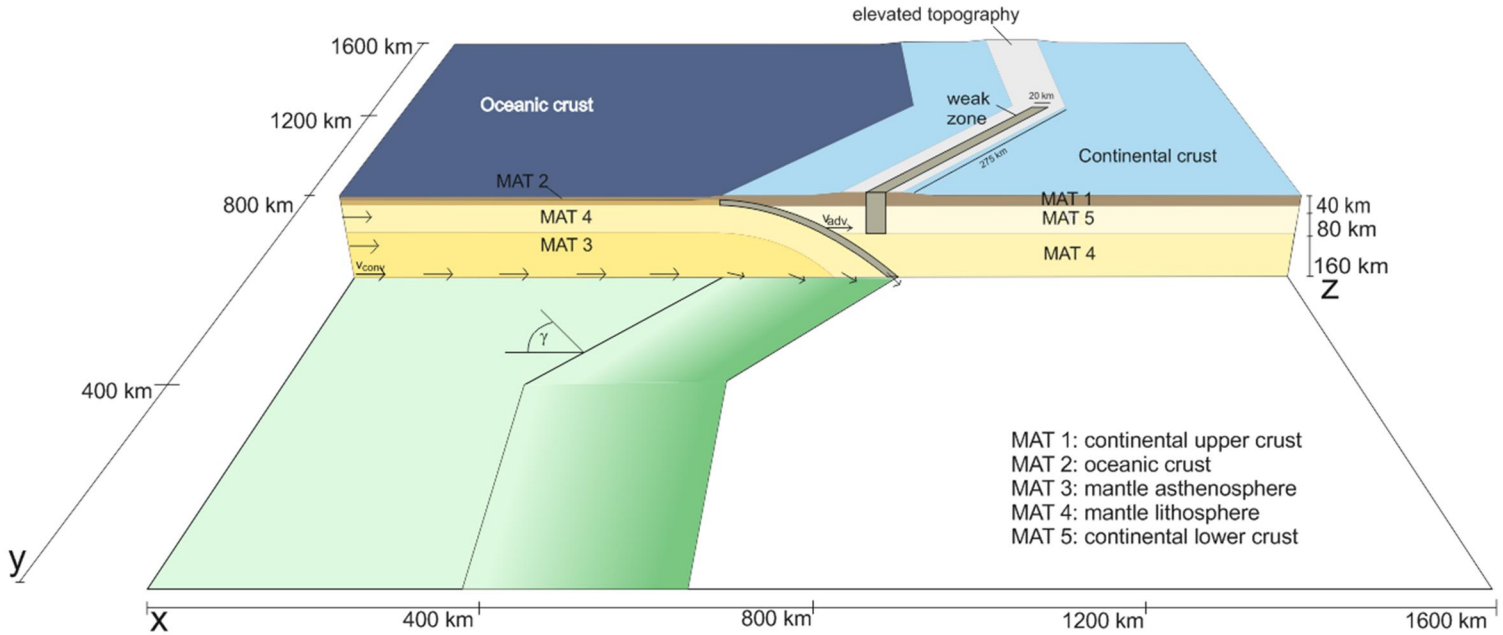

Figure 1.1. Schematic view of the model design. Cross section: advancing subduction (v_{adv} = 2cm/a) with total convergence velocity of v_{conv} = 7 cm/a. Material properties for materials one to five are given in Table 1. Upper surface: generalized topography of the study area including a continental weakness (e.g. volcanic arc) indicated with the grey box which corresponds to the grey zone in the side view. Basal surface: oblique (angle γ) zone of subduction between Nazca Plate and South American Plate. All grey zones have the same material properties as the host material except a friction angle of φ = 2° instead of φ = 4° (slab) and φ = 15°(continent), respectively. The green color represents the velocity field: constant influx velocity (v_{conv} = 7 cm/a) on the left (oceanic side), in agreement with the shape of the slab increasing downward velocity component in the subduction zone and zero velocity on the left (continental side).

Boundary conditions

The plate convergence velocity is v_{conv} = $7cm/a$. The subduction velocity is defined to be v_s = $5cm/a$, which results from v_{adv} = $2cm/a$ of subduction zone advance into South America. Defining the velocity boundary field like this, the margin of the two plates stays in the center of the modeling domain. The influx velocity along the left-hand side of the model is constant over the entire area and balanced by the out flux along the bottom of the model. The velocity field on the bottom is defined for the subduction geometry and drives subduction. A schematic velocity field of the reference model is shown in Figure 1.2.

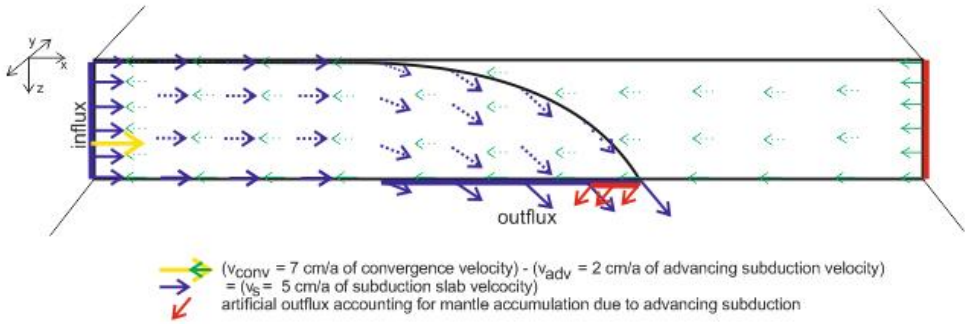

Figure 1.2. Cross section view of the reference model with a schematic representation of the velocity field. Only velocity vectors at the boundary of the domain are prescribed, the dashed vectors inside are illustrating a possible flow field. Blue arrows represent the subduction slab velocity fixed with v_s = $5cm/a$ at x=0; the influx area (left-hand side blue bold line) is balanced against the outflux area (bold line at base of model domain); green arrows are uniform over the entire area with v_{adv} = $2\ cm/a$ and represent the advancing character of the subduction zone; together with the slab velocity, the total plate convergence velocity is v_{conv} = $7cm/a$; red arrows represent the outflux of continental mantle required to balance the influx at x=1600 km.

Assuming crustal shortening only, mantle lithosphere is removed at the base of the model. For this, a mantle outflux velocity in front of the subducting slab is introduced. This is needed because otherwise the way advancing subduction is implemented in this model causes the mantle to pile up and to rise to the surface.

Material parameters and properties

Assigned material properties for the purely mechanical experiments, largely adopted from Currie, et al. (2015) and Beaumont, et al. (2006) as well as references therein, are shown in Table 1 below.

Table 1. Material properties used in the mechanical model

	Material 1 **continental upper crust**[*1] 0- ~30 km	**Material 2** **oceanic crust** [*1] 0-7 km	**Material 3** **mantle astheno-sphere**[*2] 80-160km	**Material 4** **mantle litho-sphere**[*2] ocean: ~20-80 km cont.: 80-160 km	**Material 5** **continental lower crust**[*1] ~30-80km
density (kg/m^3)	2800	3000	3250	3250	2900
viscosity pre-factor ($Pa\ s^{-1/n}$)	10^{29}	10^{29}	10^{20}	10^{29}	10^{29}
cohesion (MPa)	1	1	1	1	1
friction angle	15 (2)▪	4 (2)▪	– –	15	15 (2)▪
approx. rock rheology	Wet Quartzite	Dry Maryland Diabase	Olivine	Olivine	Dry Maryland Diabase

[*1] Currie, et al., 2015
[*2] Beaumont, et al., 2006

▪ friction angle in the material (friction angle in the weakened area within the material)

With these experiments being purely mechanical, the chosen nominal viscosity of the mantle and the Mohr-Coulomb criterion (cf. Chapter 3.2.2), together with the prescribed reference cohesion $c = 1$ MPa are used to define a threshold between plastic and viscous deformation. Material experiencing a strain smaller than the, to the reference material, corresponding strain, will be treated as plastic. This means practically, that most materials will deform with plastic behavior in these experiments. Two main sets of experiments are considered, one with and one without a weak zone in the continental crust (Figure 1.1). The actively subducting part of the slab is kept weak in both. These weak zones are implemented using a friction angle of $\varphi = 2^{\circ}$ in the subducting part of the slab and in the continental crust while other areas have a friction angle of $\varphi = 4^{\circ}$ (slab) and $\varphi = 15^{\circ}$(continent), respectively; these values are chosen based on general rock strengths (Chapter 3.1.5) and previous calibrating and spin up model runs.

Model assumptions and restrictions

The uppermost surface was chosen to be kept fixed after several attempts with a free surface, which led to numerical problems and/or unreasonable results including sinking or uprising of the surface out of proportion. To be able to compare results, the surface is fixed for all runs. A – properly – deforming uppermost surface would influence the isostasy and gravity of the

whole system. However, keeping the surface similar to the topography observed in the study area and especially maintaining a stable numerical solution is of necessary importance.

The models do not include a crustal root underneath the Andes. This too would influence the isostasy and velocity regime in the interior of the continental crust close to the plate margin due to crust reaching deeper down. Also, the thicknesses of the continental crust and mantle lithosphere are - especially with ridges influencing the age of the oceanic lithosphere in this particular area - supposedly much thinner than designed in the model. Focusing on deformation and strain partitioning in the continental crust, this thickness is not thought to be crucial for the results and thus this thickness has been chosen for reasons of simplicity.

The slab and its subduction path are predefined using the velocity boundary conditions instead of utilizing a gravitationally induced slab. This of course is an intervention which restricts the development of the subduction zone critically. However, because the model is only 160 km thick, the favorable gravitationally induced slab is difficult to realize numerically. Also, an identical slab for all runs allows for more accurate comparison between the different parameter selection for slab subduction angle and obliquity.

The continental weakness zone, which could be a volcanic arc or a pre-defined fault zone, and other features of the subduction system are treated as perfectly box-shaped, straight or parabolic. This is one drawback numerical models in general have. All shapes, boundary conditions, material properties, etc. are approximations of nature and can never perfectly mirror the nature. In all numerical models sacrifices of mimicking nature need to be made in order to maintain understandable, usable, reproducible and conclusive models.

The largest withdraw is the simplicity of these experiments regarding temperature dependence. In these experiments, no temperature calculations, and thus no temperature-dependent rock properties are accounted for. This means that no weakening of crust, lithosphere or subducting slab due to (partial) melting is accounted for. Weakening of subducting slab and a continental weakness might favor strain partitioning in the overriding plate. However, if heat of a convecting lithosphere in the mantle wedge would weaken the continental crust at the margin of the plate, the entire system would be weaker and possibly restrict strain partitioning. This question is taken up in Case Study III.

Run time

In order to achieve run times of geological significance, run times of at least 2 million years are desirable. For various reasons, the run times of the models do not exceed 800 ka or 1 Ma. This is not ideal, but acceptable. The run time of 800 ka is enough to make qualified statements as the model at time zero is representing the approximate shape of the present day Andes and further observation of the evolution until about 800 ka is not showing significant changes in the dynamics of the system, which makes one assume it would not change in the further run, unless the system becomes unstable. In that case, however, the run would stop or other numerical issues where to be handled with, instead of geophysical.

1.2 Results and Discussion

In order to keep track of the experiments presented in this part of the work, the chart shown in Figure 1.3 gives an overview of the experiments and how they relate to each other as well the research area:

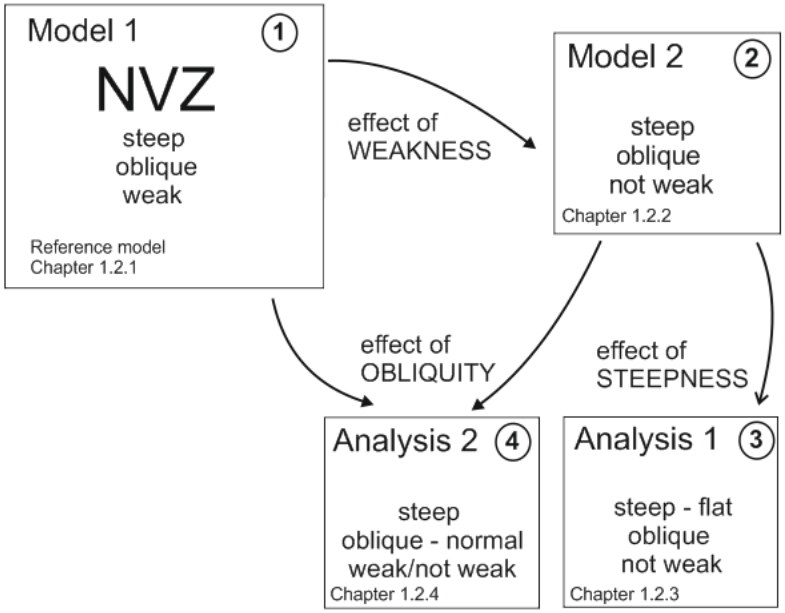

Figure 1.3. Flow diagram showing the procedure to investigate the influence of continental crustal weakness, subduction slab dip angle and subduction obliquity angle. The key steps are to compare *steep* (35°) and *flat* (25°) parabolic shaped subducting slab (Gutscher, et al., 1999; Stern, 2004; Ramos, 1999), *oblique* (40°; Velosa, et al., 2012; McNulty, et al., 2002) and *normal* (0° obliquity) as well as *weak* (continental crustal weakness) and *not weak* (no continental crustal weakness, i.e. uniform continental strength).

The reference model (Model 1) is designed to represent the NVZ, the characteristics of which are reduced and simplified to the following key points: 1) steep (35°) subduction angle, 2) obliquity angle of about 40° and 3) continental crustal weakness, which might be represented by a volcanic arc, pre-existing fault systems, or boundaries of stronger crustal blocks. In Chapter 1.2.1 this model is presented and discussed in order to get an understanding of the study area. Proceeding from this starting point, different characteristics are altered in order to study the effect they have on the dynamics of the continental crust. To investigate the influence of the weakness in the continental crust, an identical model without a weakness is compared to the reference model with a weakness in Chapter 1.2.2. The parabolic shape of the subducting slab means that the subduction angle is changing with depth. The influence of the subduction angle of the slab is discussed and analyzed in Chapter 1.2.3 and after interpreting a series of model runs with varying obliquity angles, the

combined influence of the geometry is evaluated in Chapter 1.2.4. The runtime for each experiment was between 800 ka and 1 Ma years and the output was reported after every 15 000 years.

1.2.1 The NVZ – Model 1 (Reference model)

Before presenting results, the appearance of the reference model at time step zero is shown in Figure 1.4, displaying the top surface with the elevation in km as well as materials and velocity vectors at the front side of the model domain.

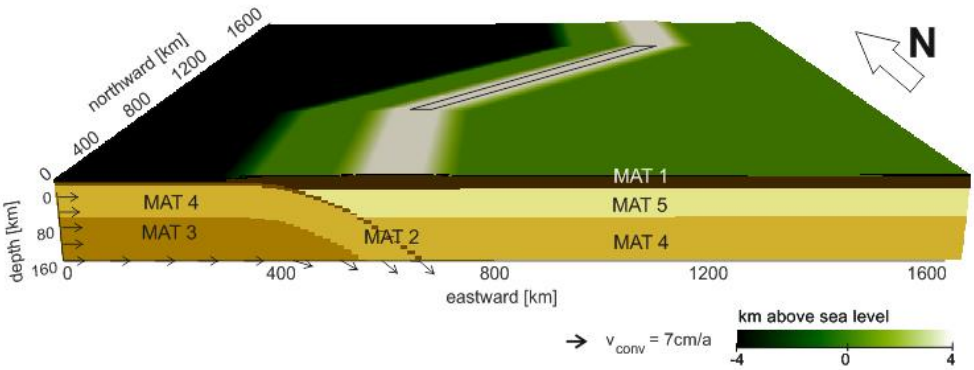

Figure 1.4. Initial experiment set up of the NVZ with continental weakness: top surface with topography [km above sea level] and the black contour indicating the position of the mechanically induced continental weakness; side view with material numbers 0 to 5 referencing to the listed materials in Table 1 and black arrows represent the velocity field.

The top surface in Figure 1.4 has a highest elevation of 4 km above sea level (white), which correlates to the Andes in Northern South America. The right-hand side of the model (green) domain is at about sea level and the left-hand side (dark green) about 4 km below sea level, which is a typical average depth for ocean basins. The model treats water as air, which means, that the mass and weight of the 'ocean' is heavily underestimated but including different domains for water and air would complicate the model unnecessarily.

The continental weakness was incorporated as a polygon as marked in Figure 1.4 and in the schematic drawing of the model geometry in Figure 1.1. The weak area stretches along the entire oblique segment with a width of 20 km and extends across the full thickness of the crust. Material properties are described in Table 1.

Results

As the top surface is kept fixed through the entire run, there is no uplift or change in the model topography as would be expected in nature. However, the code calculates the rate of rock uplift, which is immediately eroded/removed. This suppressed (or potential) rock uplift after 1 Ma is shown in Figure 1.5.

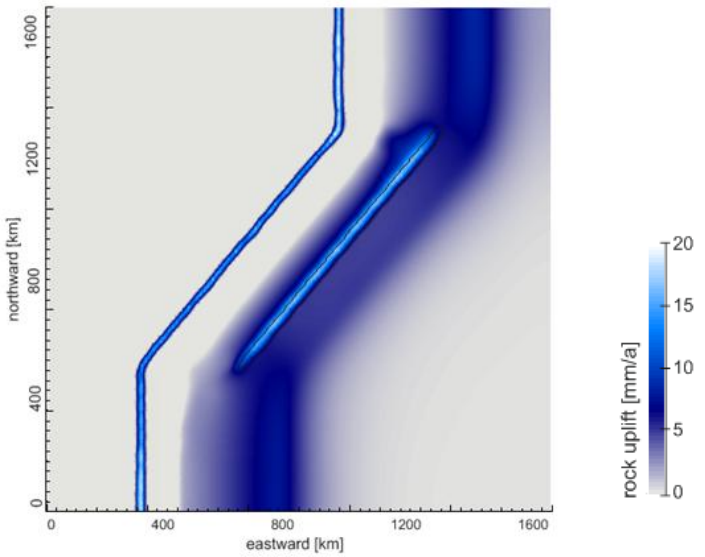

Figure 1.5. Potential rock uplift rate [mm/a] after 1 Ma run time with continental weakness. The area of continental weakness coincides with the area of highest uplift rate in the continent.

One sees that the rock uplift rate is between 10 mm/a and 15 mm/a in the assigned area of continental weakness and in the trench and about 7.5 mm/a in the area of elevated Andes. Uplift rates in this area have been estimated by investigation of paleobotanical (Gregory-Wodzicki, 2000) and fission-track (Mora, et al., 2008) data to be between 0.6 mm/a and 3 mm/a, which is around 35 to 7 times smaller than the uplift rates reached here. This mismatch can be explained by the fixed surface, which alters the natural surface mass balance. The uplift rates in the elevated area are expected due to the uplift pattern in subduction zones and the especially high uplift rate in the continental weakness occurs because of the weak material is easily deformed and uplifted. In a subduction zone, the accretionary prism is easily identified as uplift just by scraping sediments off the oceanic plate.

In order to survey the movement of the model layers in correlation to the velocity field and to see if the artificially suppressed uplift has an impact on the distribution of the lithosphere, Figure 1.6 shows the layers with material numbers and the vector field at the middle of the modeling domain. The lithosphere is lifting in the area between the plate margin and the

continental weakness as well as in the area of the continental weakness itself. This can be seen well in Figure 1.8. This movement is plausibly accounting for the shortening in the crust observed in subduction zones. There is no uplift in the mantle lithosphere (material 4) observed.

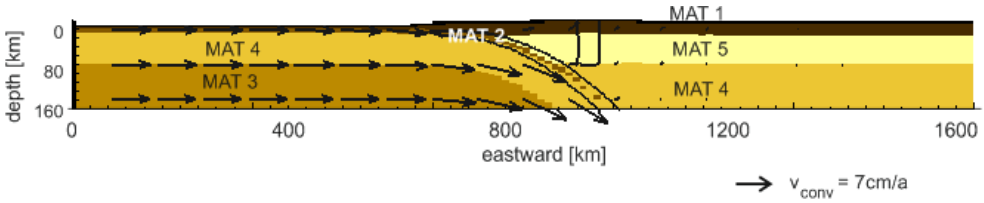

Figure 1.6. Cross-sectional view of the reference model after 1 Ma showing layers with materials 1 to 5 referencing to the listed materials in Table 1. Black arrows represent the velocity field and the black contour the mechanically weakened slab as well as the continental weakness. The cross section is positioned in the middle of the model domain (y = 80 km).

The uplift (cf. uplift rates Figure 1.5) in the Andes region is supported by the velocity vectors shown in the cross-sectional view (Figures 1.6 and 1.8). The vector field shows a clear uplift at the continental margin and at the location of the continental weakness. The upward component of the velocities has a magnitude of about 10 mm/a. The velocity vectors indicate slightly thrusting toward the continent.

The map view (both panels in Figure 1.7) of the model after 1 Ma reveals a coherent block of continental crust moving margin parallel. Figure 1.7 shows two different representations of the surface velocity: (a) the margin parallel velocity component and (b) the northward (y-axis) directed velocity component. In both panels the area between the continent margin and the continental weakness can be easily identified as moving coherently and detached from the continental plate. Margin-parallel velocities are 1 – 1.5 cm/a or 0.6 – 1.3 cm/a northward. This region is thus interpreted as a continental sliver and the velocities match very well the velocities (~1 cm/a) published by e.g. Nocquet, et al. (2014), Gutscher, et al. (1999) and Velosa, et al. (2012). Maximum values 2 cm/a (red) for the margin parallel component representation and 1.3 cm/a (green) for the northward directed component are in the vicinity of the margin.

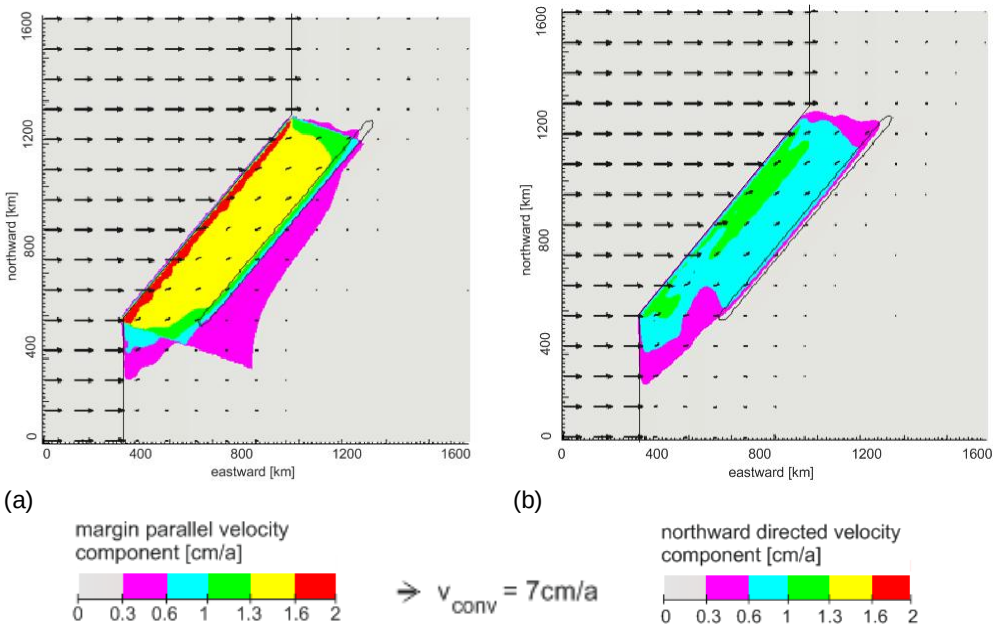

Figure 1.7. Velocity field (black arrows) at the top surface of the NVZ reference after 1Ma: **(a)** margin parallel component, **(b)** northward component. The black contour marks the position of the continental weakness and the black line the position of the continental margin.

The main difference between the two representations of the velocity field is the frame of reference. When looking at the margin parallel velocity component, one needs to consider the angle of obliquity (or the orientation of the boundary between the two plates). In that sense, the representation of the northward directed velocity component is universal for all plate boundary geometries. The difference in values between the two representations is rather small. The margin parallel velocity component representation is chosen for in the first two chapters (Chapters 1.2.1, 1.2.2) where the influence of a continental weakness is investigated with consistent obliquity angle. Both representations are shown for top view velocity plots in order to provide a comparison to the northward component velocity plots in the side views. In representations of experiments of varying subduction angle and consistent obliquity angle (Chapter 1.2.3), velocity plots show the northward directed velocity field. Also, in the subsequent chapters (Chapter 1.2.4) only the northward directed velocity component representation is chosen, as with varying obliquity angles, this representation offers a constant reference frame. The black arrows represent always the total velocity field.

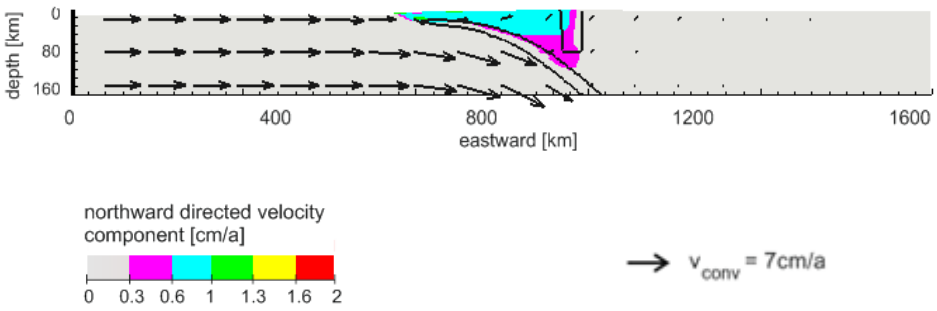

Figure 1.8. Velocity field after 1 Ma run time with continental weakness. Northward directed component of the velocity colored and black arrows representing the overall velocity field. The black contours mark the weak oceanic slab and the continental weakness. Cross-sectional view cuts through the middle of the model (y = 800 km).

In Figures 1.7 and 1.8 the sliver is clearly identified as being positioned between the plate margin and the continental weakness with a northward moving velocity of about 0.6 – 1.3 cm/a (green/blue color). The velocity of the wedge shaped sliver is decreasing with depth to 0.3 cm/a (purple color). The inter plate friction is increasing the force resisting shear motion at the plate boundary.

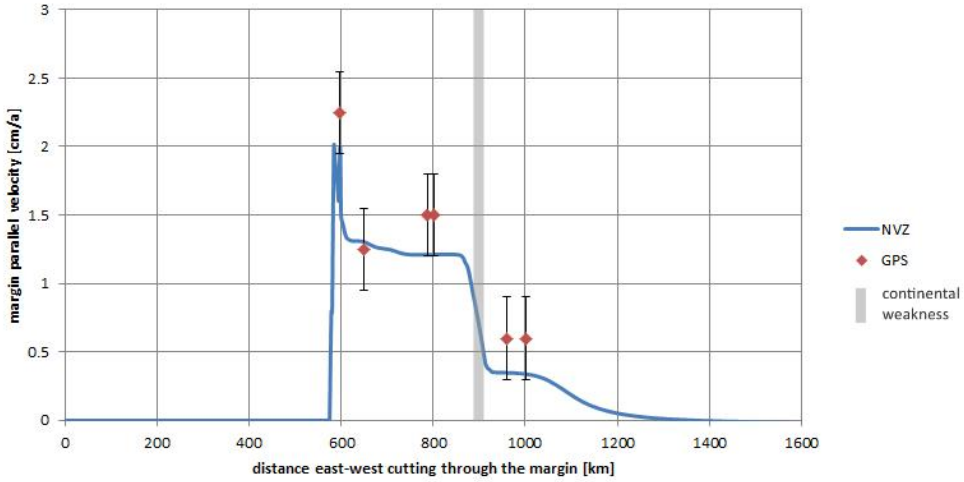

Figure 1.9. Margin parallel velocity component [cm/a] against the distance from the trench [km; x- axis in the model] for the NVZ model set up with a continental weakness and SW-NE GPS velocities observed in the area (Mora-Páez, et al., 2016; Veloza, et al., 2012 and references therein; error bars ±0.3cm/a). Grey bar indicates the position of the continental weakness.

The high velocity of the sliver is revealed in the velocity graph (Figure 1.9) showing the margin parallel velocity component [cm/a] against the distance through the model [km; east-west cutting]. At the position of the plate boundary on the continental side, margin parallel velocity component rises from zero to peak at about 2 cm/a. This is due to the very low subduction angle in the close vicinity of the plate margin. The velocity decreases to about 1.3 cm/a and flattens out for around 200 km inland, where the continental weakness (grey bar in Figure 1.9) is positioned. The velocity decreases and drops to zero. GPS velocities transferred from UNAVCO and GeoRed GPS databases by Mora-Pàez et al. (2016) (Figure 1.9) and Veloza, et al. (2014) (Chapter 2.1: Figure 2.2) are in good agreement with the velocities calculated in the numerical experiment.

Figure 1.10 shows the strain rate in the oblique segment with continental weakness. Mainly two major zones of high strain rates are observed. Those are – not surprisingly – the weak subducting slab and the continental weakness. In these areas, the strain rate goes up to about $13 \cdot 10^{-15}$ 1/s when is compared to $41 \cdot 10^{-16}$ 1/s found in studies using earthquake data (Corredor, 2003) an acceptable value.

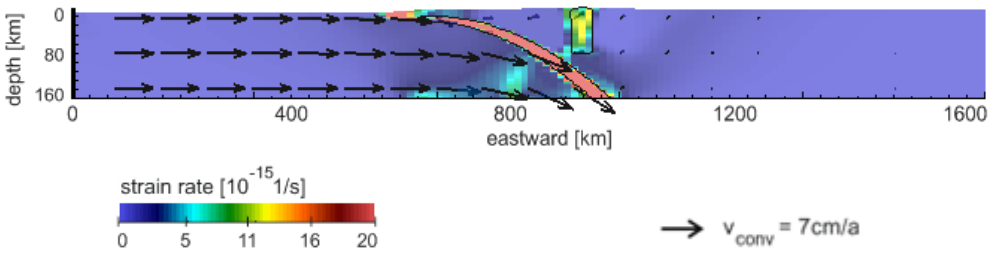

Figure 1.10. Strain rate after 1 Ma run time NVZ model with continental weakness. The velocity field is represented with black arrows and the black contour lines mark the position of the weak oceanic slab and the continental weakness. Cross-sectional view cuts through the middle of the model (y = 800 km).

In summary, this reference model is – in accordance with the appearance of the NVZ sliver as described by e.g. Nocquet et al. (2014) – showing a strong northward trending sliver with velocities of up to 1.3 cm/a. Velocities resulting from the model experiment are ranging from slightly higher (1.3 cm/a) than observed measured values (approx. 1 cm/a; Nocquet et al., 2014) to marginally smaller (1.5 cm/a; Mora-Páez, et al., 2016) and are thus acceptable when compared to these observed velocity values. Sliver movement and continental weakness are well constituted and the NVZ nicely represented.

1.2.2 Effect of a weak zone in the continental crust – Model 2

The influence of the continental weakness on the dynamics of the system is investigated in the following. Here, a model with a homogenously strong continental crust is presented. The continental weakness of the reference model has been removed. This design of the experiment is labeled as Model 2 in the flow diagram (Figure 1.3). The simulated time is again 1 Ma.

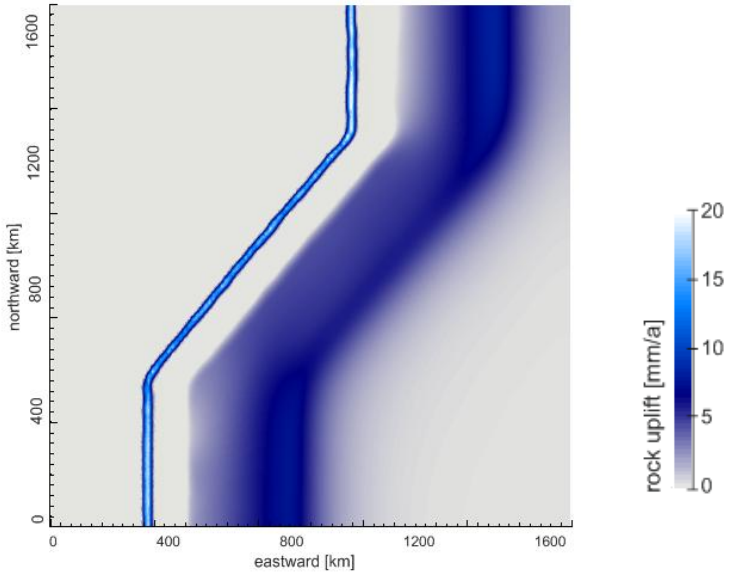

Figure 1.11. Potential rock uplift rate [mm/a] after 1 Ma run time NVZ model without continental weakness.

The rock uplift pattern for Model 2 without a continental weakness (Figure 1.11) looks similar to the rock uplift pattern of the NVZ with continental weakness (Figure 1.5). The rapid uplift rate (15 – 20 mm/a) in the trench is the same, as well as the overall (~7.5 mm/a) in the elevated region in the continent. However, in Model 2 with a homogeneously strong continental crust, there is no region of rapid uplift rate as it was observed in the model with a continental weakness present. This is not surprising, as the weak and easily deformable material is missing here. Still, uplift rates overestimate observed uplift rates (Gregory-Wodzicki, 2000; Mora, et al., 2008).

In order to monitor the movement of the layers Figure 1.12 shows the velocity field and the materials (numbers referring to Table 1). There is only one minor, although explainable difference between this material uplift pattern and the one in the reference model: in the reference model a small amount of uplift of the lithosphere in the area of the continental weakness is observed, which is not seen here. This is explained by the continental weakness being an easier path for uprising material compared to a homogeneously strong crust.

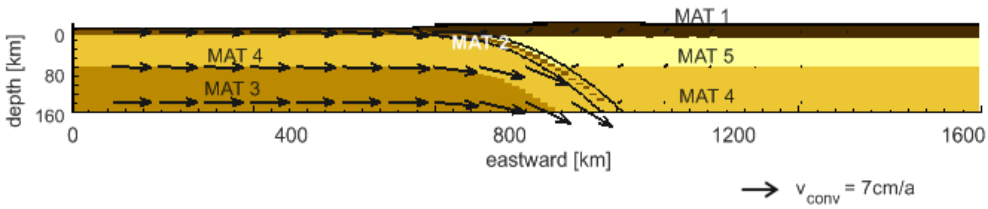

Figure 1.12. Cross-sectional view of the NVZ model without a continental weakness after 1 Ma showing layers with materials 1 to 5 referencing to the listed materials in Table 1. Black arrows are the velocity field and the black contour outlines the mechanically weakened slab. The cross section is positioned in the middle of the model domain (y = 80 km).

The map view (both panels in Figure 1.13) of the model run after 1 Ma does not show a clear sliver movement. Again, the panels show (a) the margin parallel velocity component and (b) the northward directed velocity component together with a set of representative velocity vectors (black arrows).

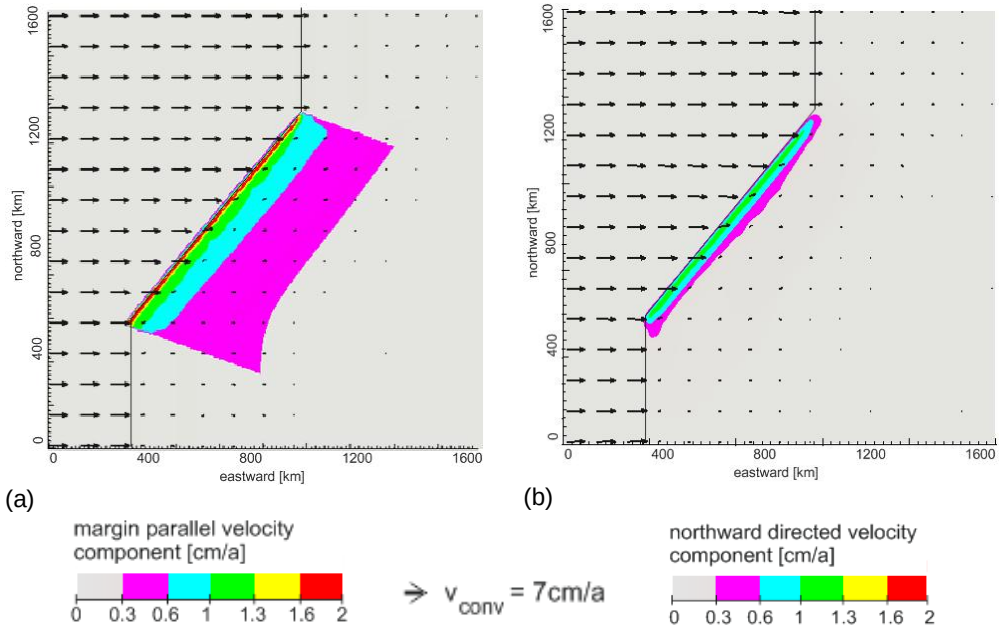

Figure 1.13. Velocity field (black arrows) at the top surface of the NVZ model without a continental weakness after 1Ma: **(a)** margin parallel component, **(b)** northward directed component. The black line marks the position of the continental margin.

The margin parallel velocity component is slightly higher than the northward directed component but this is partly due to the fact, that the margin parallel component includes eastward velocity component, which is the dominating direction of motion. It is clear to see, that the continental crust does not experience high northward or margin parallel velocities,

i.e. there is no sliver movement and with this there is a clear difference to the velocity fields of the reference model.

A narrow zone of rapid northward velocity in the continental plate is observed in direct vicinity of the plate boundary. The highest velocity in the reference model was also observed at the same location. This is resulting from the very shallow subduction dip angle in close vicinity to the plate margin (cf. Chapter 1.2.3). However, Model 2 shows clearly that without a continental weakness, northward directed velocity components are only up to 0.6 cm/a across the area where a sliver might be expected.

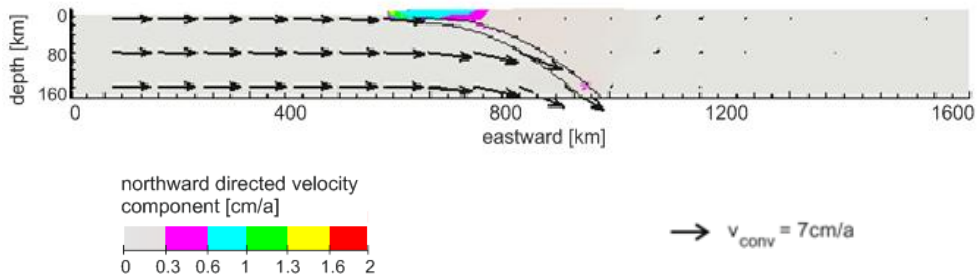

Figure 1.14. Velocity field after 1 Ma run time NVZ model without continental weakness. Northward directed component of the velocity colored and black arrows representing the velocity field. The black contour marks the weak oceanic slab. The cross-sectional view cuts through the middle of the model (y = 800 km).

The map view (Figure 1.13) together with the cross-sectional view (Figure 1.14) of Model 2, make it clear that only the continental crust in close proximity to the margin is affected by the oblique subduction. There, the subduction dip angle is to shallow to allow the upper plate to move independently from the subsiding plate and the upper plate is dragged with about 0.6 – 1 cm/a northward.

The velocity graph (Figure 1.15) emphasizes the influence of the continental weakness on the development of a continental sliver. At the margin, both velocities increase into a peak of almost the same value (Model 1: ~2 cm/a and Model 2: ~1.8 cm/a). After that the velocity of Model 2 decreases nearly exponentially to flatten out at around 0.5 cm/a approximately 200 km inland from the trench and reaches zero around 700 km inland from the trench. This is a notable contrast between the reference model and Model 2: in the reference model the region of northward movement is about 300 km wide with velocities up to 1.3 cm/a and rather sharply bordered, while in Model 2 the rapid northward movement stretches over a smaller area and average northward directed velocities are of about 0.6 cm/a.

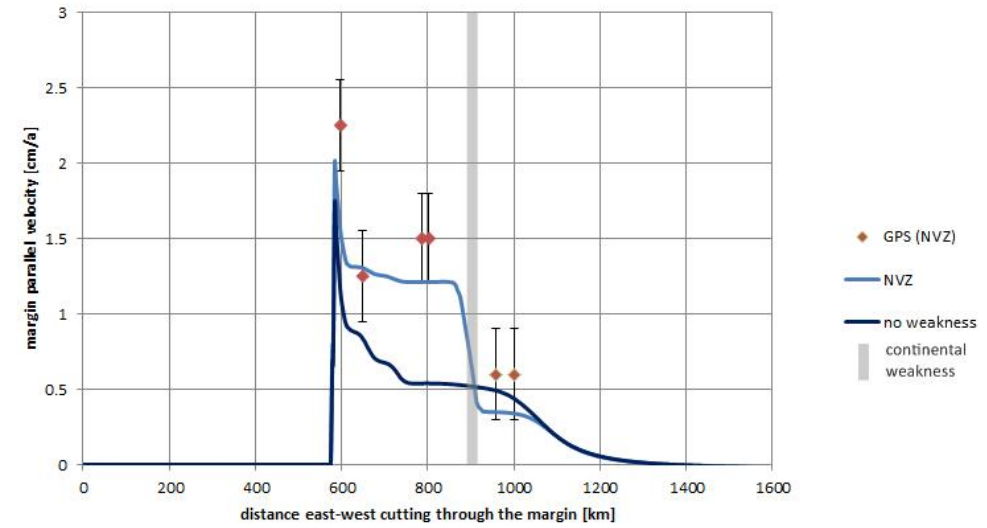

Figure 1.15. Margin parallel velocity component [cm/a] versus distance from the trench [km; x- axis in the model] for the NVZ model set up without (dark blue) and with (light blue) a continental weakness and SW-NE GPS velocities observed in the NVZ study area (Mora-Páez, et al., 2016 and Veloza, et al., 2012 and references therein; error bars ±0.3cm/a). Grey bar indicates the position of the continental weakness.

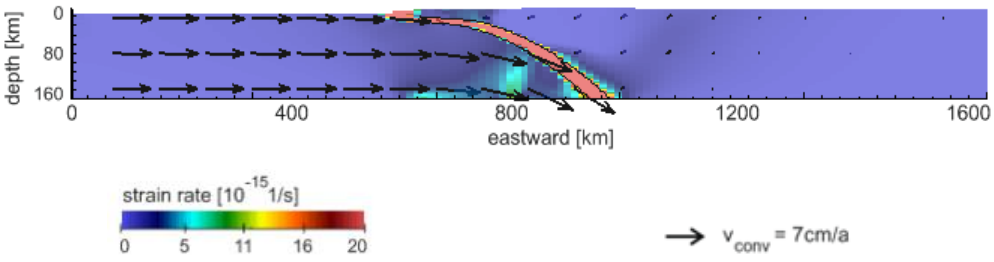

Figure 1.16. Strain rates after 1 Ma run time for the NVZ model without continental weakness. The velocity field is indicated by black arrows and the black contour outlines the position of the weak oceanic slab. The cross section cuts through the middle of the model (y = 800 km).

The strain rate pattern of the model with uniformly strong continental crust (Figure 1.16) and the reference model with continental weakness (Figure 1.10) only differ in the presence or absence of the weakness itself and the high strain rates in the weakness (Model 1) or homogeneous strain rates in the continental crust (Model 2). The slab experiences the same strain rate in both models.

To summarize, the model without continental weakness arc does not – contrary to the reference model with a continental weakness – show significant strain partitioning or sliver movement. A slightly higher margin parallel velocity (approx. 0.8 cm/a) appears in close vicinity of the margin. This however, is limited to the area equivalent to that of the accretionary prism. The accretionary prism is in oceanic subduction zones usually composed of the oceanic sedimentary layer which gets scraped off when the oceanic crust pushes beneath the continent. Partitioning in the accretionary prism is not considered as continental strain partitioning, as movement is limited to the region proximal to the margin and thus not considered here. The subduction angle of the slab might influence this tendency to develop strain partitioning in the forearc region. The slab, being defined as a parabola, is quite flat in the immediate vicinity of the margin and this aspect makes a frictional influence resulting in strain partitioning (i.e. margin parallel movement) inevitable. The influence on the initiation of sliver movement by a flat subduction angle is further investigated below in Chapter 1.2.3.

1.2.3 Effect of changes in the subduction angle

The subduction angle was changed in order to investigate its effect on the behavior of the continental crust proximal to the margin. The idea is that strain partitioning or the formation of a continental sliver in response to oblique subduction is inevitable in the brittle regime of the uppermost 10-15 kilometers of the crust: the shallow angle of subduction is the reason why margin parallel movement is observed in close vicinity to the margin (Bourgois, 2013, Cediel et al., 2003). Shear resisting force between the oceanic and continental crust is high for very shallow subduction angles and thus is a margin-parallel movement favored. If the slab is subducted at a shallow angle it remains in the brittle regime farther into the continent and thus forms a wider sliver compared to a steeply sinking slab. The latter one reaches depths in the ductile regime closer to the margin. In that case, the total frictional force is reduced and a continental sliver is less likely to form.

For a slab of a parabolic geometry, the subduction angle changes along the length of the slab. In order to quantify this effect, subduction angles were approximated using a triangular equivalent of the subducting slab's geometry. The effective angle is in reality smaller at the margin and larger at the bottom of the model domain, but difficult to determine for a parabolic geometry. Figure 1.17 shows a schematic illustration of how the subduction angle is defined for this dip angle analysis.

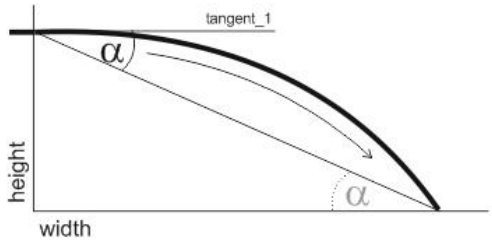

Figure 1.17. Schematic illustration of how the subduction angle α is defined for this dip angle analysis.

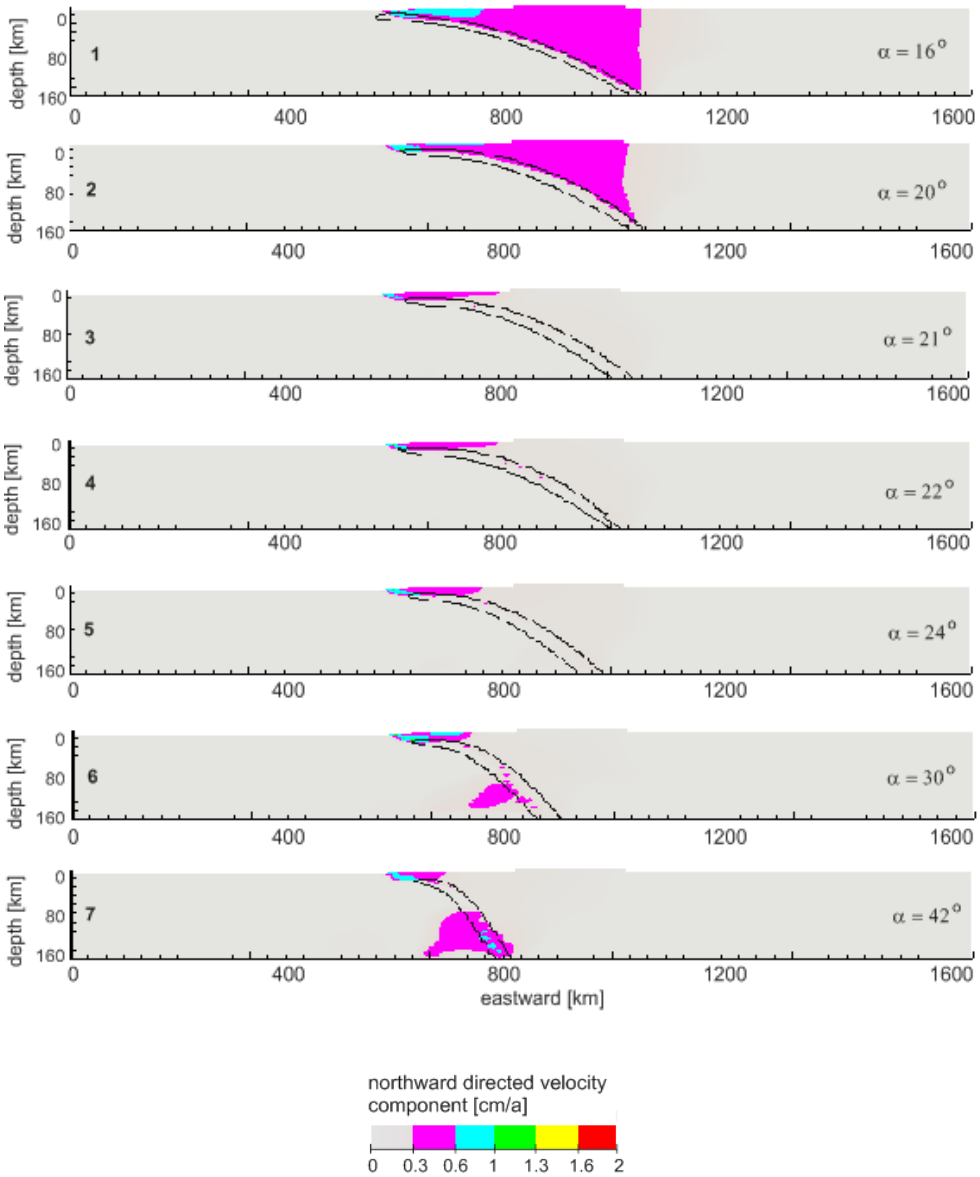

Figure 1.18. Seven models with different subduction angles α (from shallow (16°) to steep (42°); top (panel 1) to bottom (panel 7)). All models lack a continental weakness. The weak oceanic crust is marked by a black contour line. Cross-sectional views cut through the middle of the model (y = 800 km).

Figure 1.18 illustrates the negatively proportional influence of the subduction angle on the width of a forming continental sliver in a setting with homogeneously strong continental crust. Models with small angle (16° and 20°) (Figure 1.18, panels 1 and 2) are not

representative as the continental sliver area is touching the bottom of the model domain and thus may be influenced by the boundary conditions. However, the remaining panels of Figure 1.18 show that the width of the sliver decreases with increasing subduction slab angle as predicted.

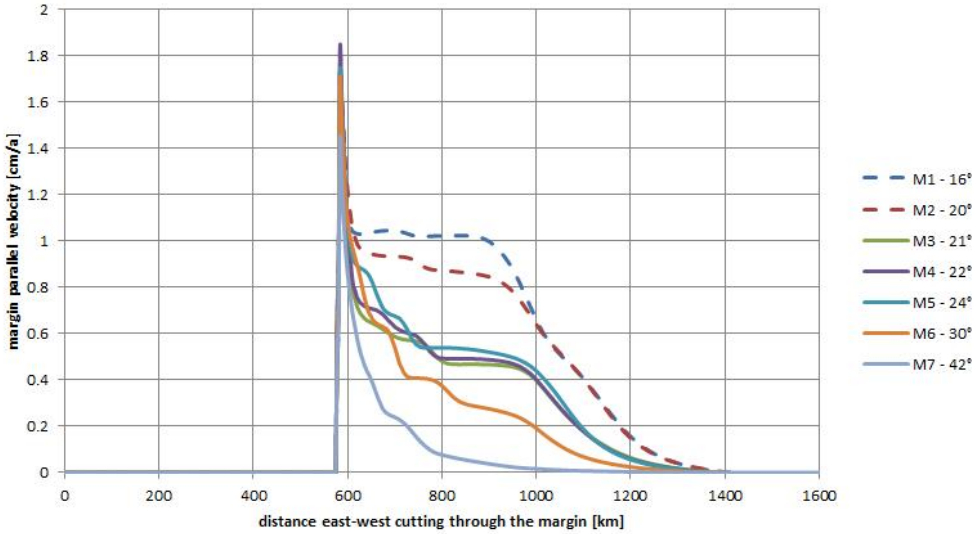

Figure 1.19. Margin parallel velocity component against the distance from the trench [km; x-axis in the model] for the NVZ model set up without a continental weakness with subduction angles from 16° to 42°. Panels M1 to M7 compare to Figure 1.18. Curves for subduction angles 16° and 20° are plotted for comparison with dashed lines, but are possibly not representative.

The velocity of the slivers peaks at the plate margin and decreases exponentially inland as shown in Figure 1.19. In addition, a more rapid exponential decrease is observed for higher subduction slab dip angles. For smaller dip angles, where the slab moves in brittle domains for longer paths, the velocities are stable with around 0.5 cm/a over a distance of around 200 km roughly 100 km inland from the margin. M5 is equivalent to the previously seen Model 2 in Table 1, the NVZ model set up without continental weakness.

To summarize the results of this Case Study to this point, one sees that the models show a good agreement to observations of nature. The reference model is representing the formation of the NVZ continental sliver well (Chapter 1.2.1). The presence of a continental weakness definitively favors the initiation of a well-developed and coherent sliver (Chapter 1.2.2). The influence of the subduction angle is crucial for the width of the partitioning part of the continental crust and the experimental series of subduction angles shows that a sliver is likely to develop even in a homogenous crust only in a much weaker and not as sharply defined manner (Chapter 1.2.3).

In order to further investigate the influence of a change in obliquity angle and how a combination of subduction and obliquity angle effect sliver formation, the next chapter presents two sets of obliquity experiments based on the NVZ models.

1.2.4 Effect of changes in the obliquity angle

The obliquity angle should undoubtedly be the main influence on strain partitioning. If the obliquity angle is zero or very small, the oblique component of the motion disappears and strain partitioning in the continental crust can consequently not be initiated. When the oblique component of the motion increases and possibly exceeds the shear strength of the continent, strain partitioning is initiated if the coupling between the two plates (in this case the subducting slab and the overriding continental crust) is strong enough. In this Chapter the influence of the obliquity angle is investigated in a series of different obliquity angles $\gamma = 10 - 50°$ in models with and without a continental weakness. The slab geometry is that of the reference model (Chapter 1.2.1), for ease of comparison. In the later part of this Chapter a combination of obliquity angle and subduction angle is studied.

Range of obliquity angle

The first experiments in this section are carried out keeping the slab geometry as in the reference model (Figure 1.1) and only changing the obliquity angle in the range of $\gamma = 10°$ to $\gamma = 50°$. This series is run for both models with and without a continental weakness. Figure 1.20 shows the top map views of the respective models and Figure 1.21 the corresponding cross sectional views.

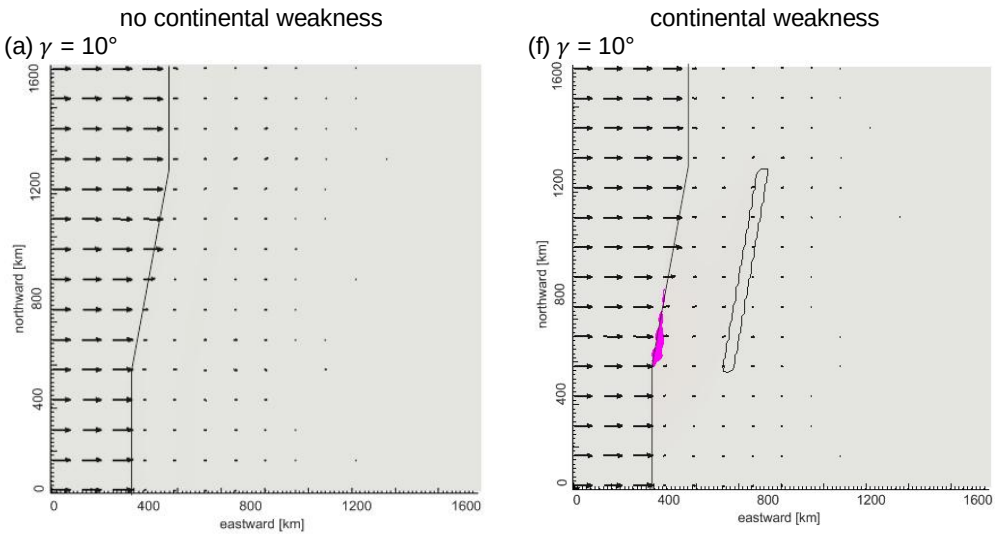

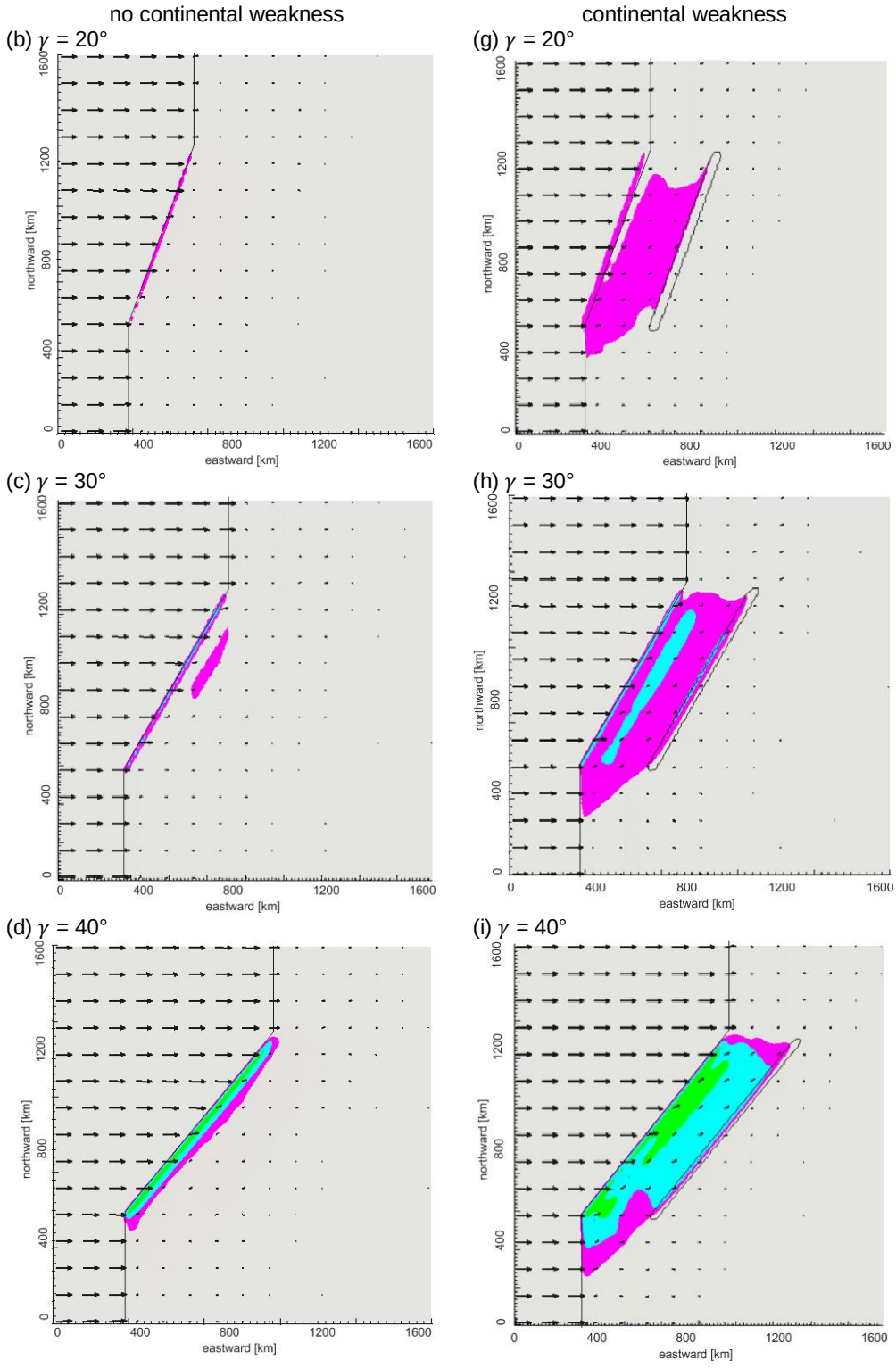
no continental weakness
continental weakness
(b) γ = 20°
(g) γ = 20°
(c) γ = 30°
(h) γ = 30°
(d) γ = 40°
(i) γ = 40°
northward [km]
eastward [km]
0
400
800
1200
1600

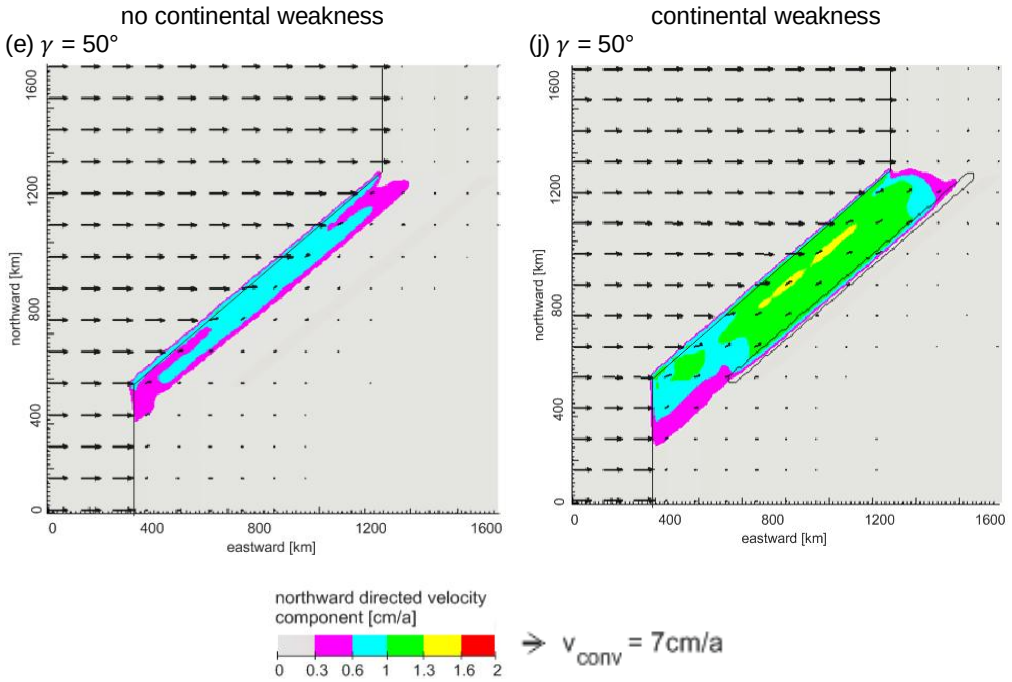

Figure 1.20. Map view of the velocity solution of the experiment sets with obliquity angles varying in increments of tens from γ = 10° to γ = 50°. Panels (a) – (e) show results for experiments without a continental weakness and panels (f) – (j) include a continental weakness. A black contour line in the continental weakness models shows the position of the weakness; the black line marks the position of the plate margin and black arrows are representing the overall velocity field.

Figure 1.20 shows, the influence of the obliquity angle and continental weakness on strain partitioning. Sliver formation is clearly enhanced in the cases that include a continental weakness. In these experiments the sliver formation begins at an obliquity angle of γ = 20° (Figure 1.20, panel g). The velocity is rather small (between 0.3 and 0.6 cm/a) but for an obliquity angle of γ = 30° the entire area between the plate margin and the continental weakness is part of the sliver. In contrast, the model without the continental weakness does not show any sliver movement at 30° obliquity angle. In the experiments without the continental weakness sliver movement is only observed for an obliquity angle of γ = 50°. In cases with smaller angles, the northward directed velocity component is only high in the trench region. This is due to very shallow subduction angle proximal to the margin and was already looked at in Chapter 1.2.3.

no continental weakness

(a) γ = 10°

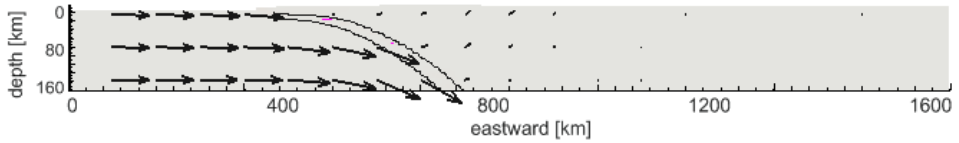

(b) γ = 20°

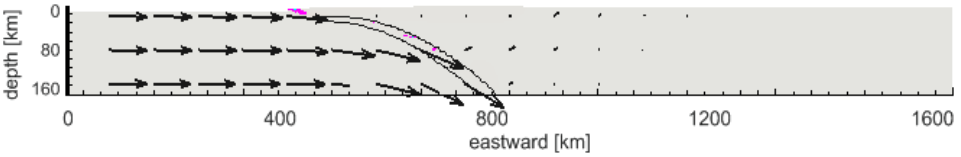

(c) γ = 30°

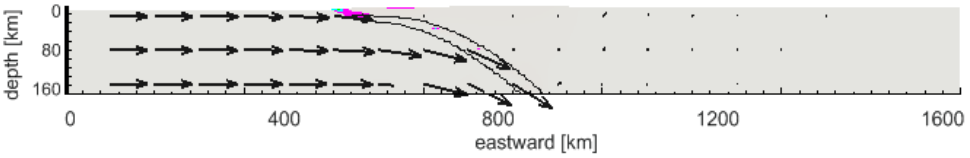

(d) γ = 40°

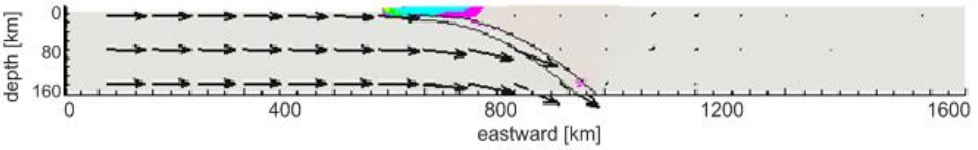

(e) γ = 50°

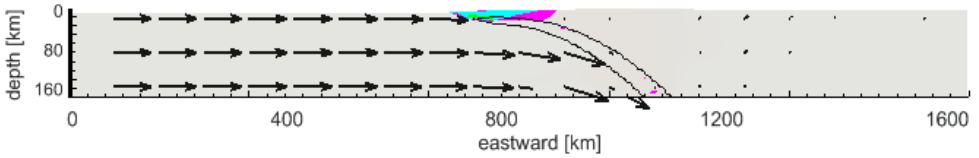

continental weakness

(f) γ = 10°

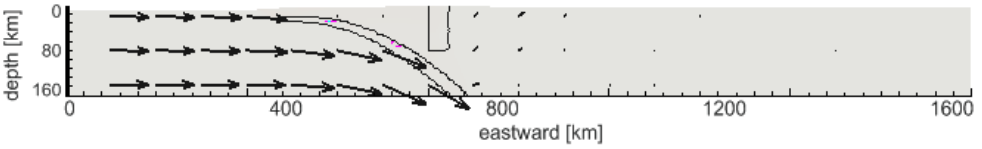

(g) γ = 20°

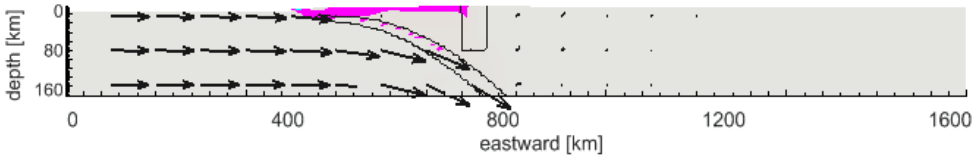

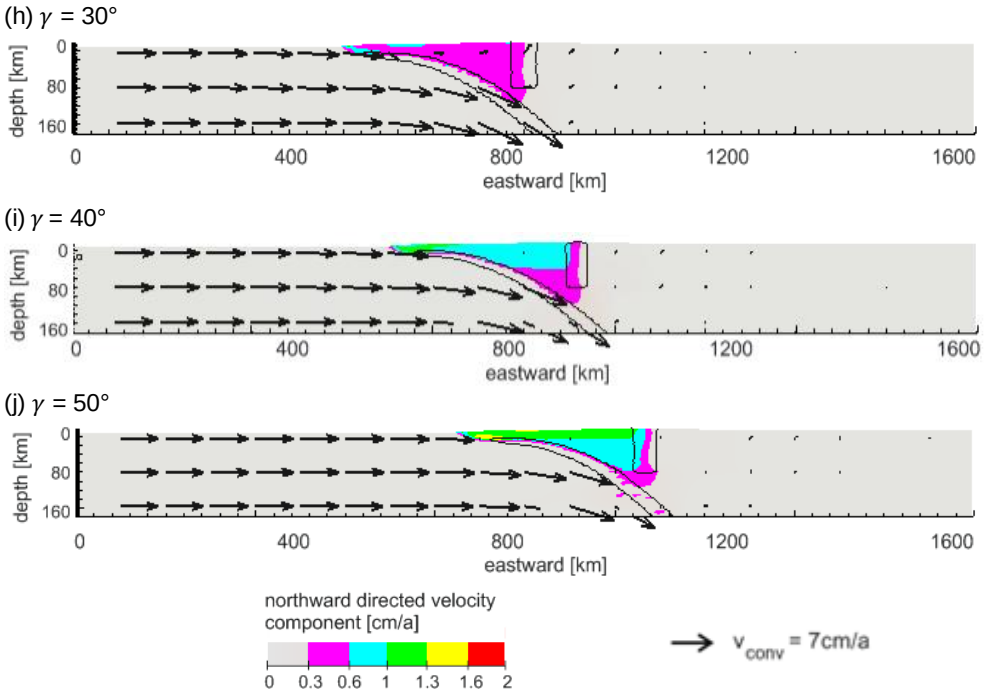

Figure 1.21. Cross-sectional view of the velocity solution of the experiment sets with obliquity angles varying in increments of tens from γ = 10° to γ = 50°. Panels (a) – (e) show results for experiments without a continental weakness and panels (f) – (j) include a continental weakness. Black contour line in the continental weakness models shows the position of the weakness; the black line marks the position of the plate margin and black arrows are representing the velocity field. Cross-sectional views cut through the middle of the model (y = 800 km).

The cross-sectional views (Figure 1.21) of the obliquity angle series is confirming what the map view revealed. For low obliquity angles no sliver movement is observed and the presence of a continental weakness enhances sliver formation.

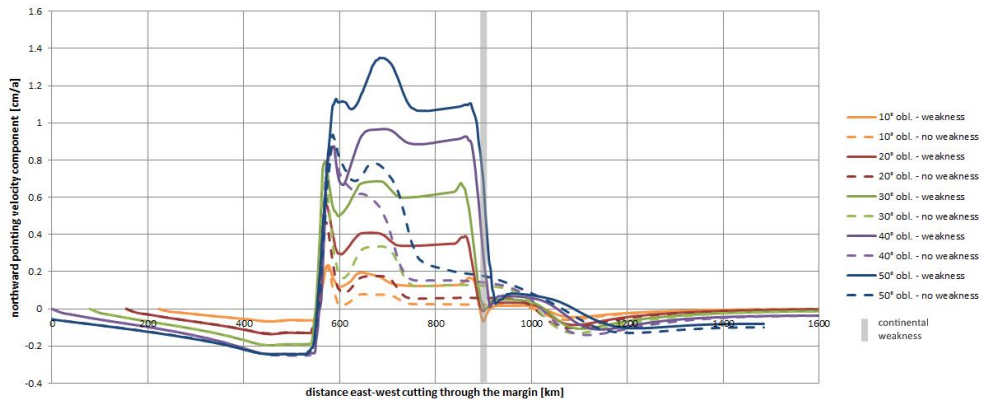

Figure 1.22. Northward velocity component [cm/y] against the distance from the trench [km; x- axis in the model] for the NVZ model set up with and without a continental weakness and obliquity angles from γ = 10°(orange) to γ = 50° (blue) (dashed curves no continental weakness). The curves were shifted to line up at the margin of the 40° obliquity. Grey bar indicates the position of the continental weakness.

The velocity component peaks in all cases of this experiment set at the plate margin as shown in Figure 1.22. Velocity peaks are higher with an increasing obliquity angle. In the cases where no continental weakness is present the velocity drops almost immediately across the plate margin. In the cases of a continental weakness present, the velocity remains high over several hundred kilometers and over the entire area between the plate margin and the continental weakness (grey bar in Figure 1.22) for obliquity angles larger than 20°.

Effect of changes in obliquity angle and subduction angle

The second set of experiments in this analysis is carried out in order to investigate the influence of the combination of obliquity and subduction angle. As seen in the analysis of the subduction angle (Chapter 1.2.3) the subduction angle is of importance for the strength of coupling between the subducting slab and the overriding plate. In the following analysis of the obliquity angle it was clear that the obliquity angle is of particular importance. In the cases where the oblique component is too low (10°) to initiate strain partitioning (Figure 1.20, panels a and f), the margin parallel movement is not even developed in the near-margin zone of shallow subduction (Analysis 1, Chapter 1.2.3). The obliquity angle has a positive correlation (stronger strain partitioning in settings with larger obliquity angles), whereas the subduction angle has a negative correlation (shallower subduction angle results in a wider zone of strain partitioning). This raises an important question: is the effect of the obliquity angle more significant than the effect of the subducting dip angle?

The question of which parameter is more significant in the initiation or enhancing of strain partitioning is discussed in this section and demonstrated using a series of model experiments with a shallow subduction dip angle combined with small obliquity angles varying in steps of 5° from 10° to 25°. All runs exclude a continental weakness. Chapter 1.2.2 already showed that the continental weakness is enhancing the initiation of a sliver but the following analysis shows that the obliquity angle has the stronger influence than the continental weakness (no strain partitioning in a weak crust with low obliquity angle). Figure 1.23 shows the map views and Figure 1.24 the cross-sectional views of the experiments in this combined analysis with about 20° subduction angle and no continental weakness.

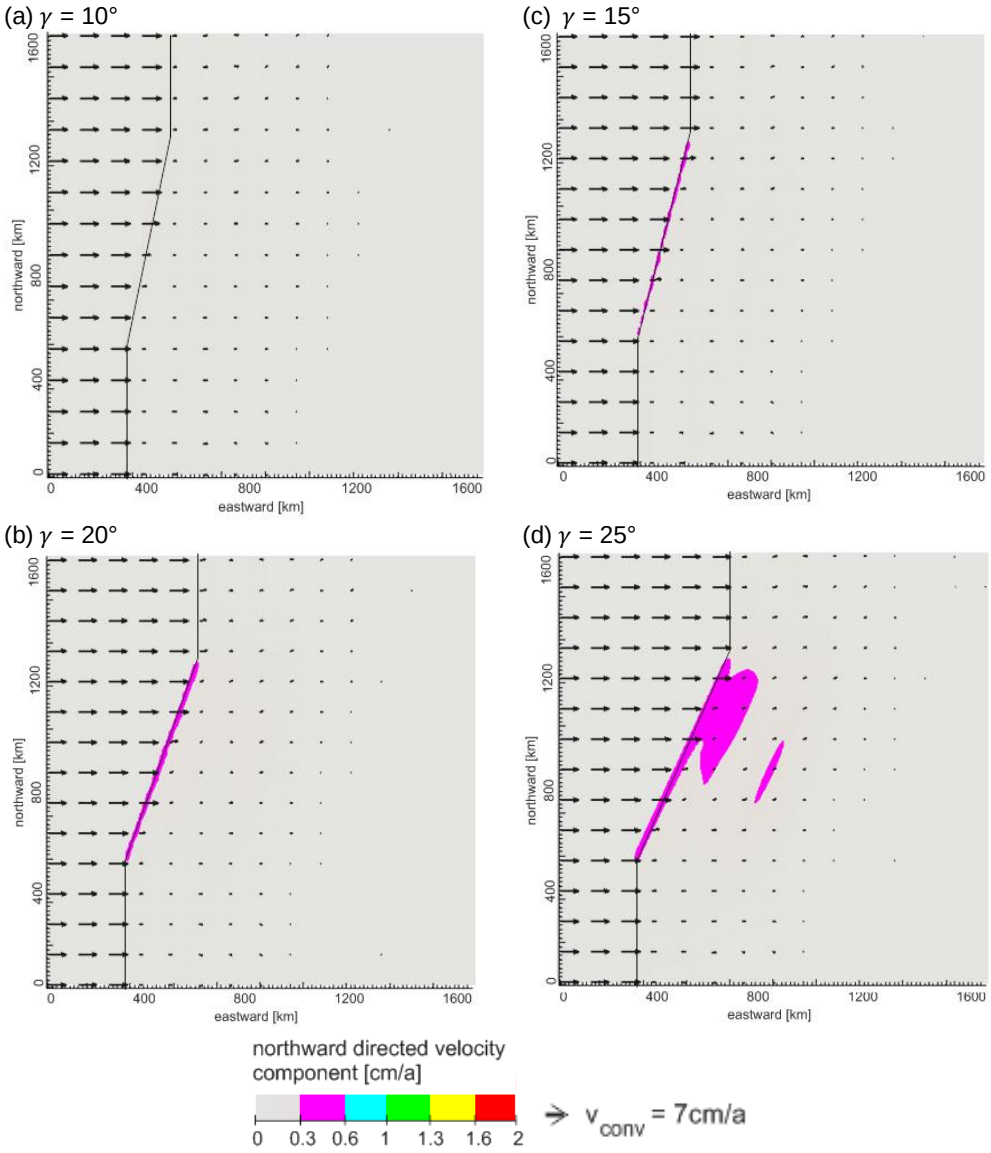

Figure 1.23. Map view of the set of obliquity angle changes in shallow subduction angle environment: the obliquity angle varies in increments of five from γ = 10° to γ = 25°. The black line marks the margin between the two plates and black arrows are representing the velocity field.

The map views (Figure 1.23) show that sliver movement is about to be initiated at an angle of 25° (panel d). The velocity is in this case not very rapid, only up to 0.6 cm/a, but the width of the sliver exceeds the immediate vicinity of the plate margin and reaches into the continent.

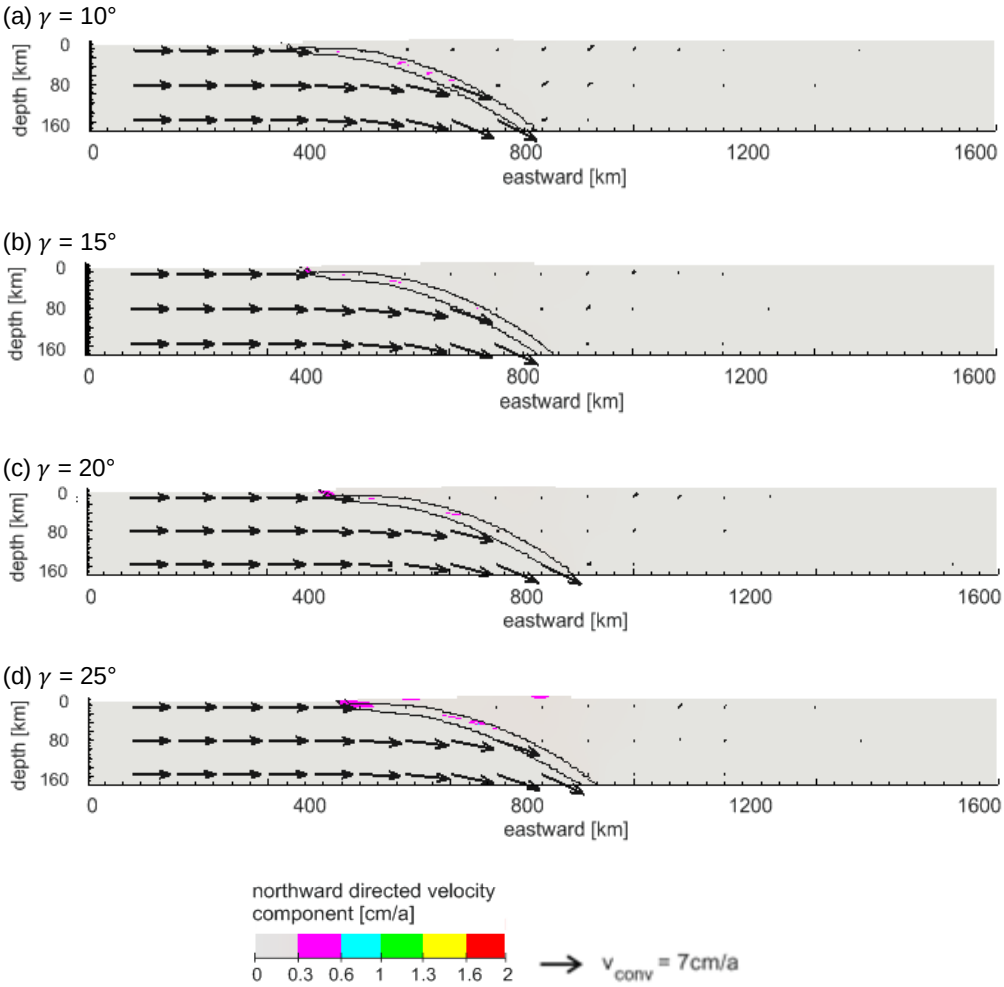

Figure 1.24. Cross-sectional view of series of obliquity angle changes in shallow subduction angle environment: the obliquity angle varies in increments of five from γ = 10° to γ = 25°. A black contour line shows the position of the weak oceanic slab and black arrows are representing the overall velocity field. Cross-sectional views cut through the middle of the model (y = 800 km).

Comparing the cross-sectional view (Figure 1.24) of this result with the corresponding experiment with the same subduction angle (20°) from the subduction angle series (Figure 1.18, panel 2) one sees that the smaller obliquity angle prevents sliver movement.

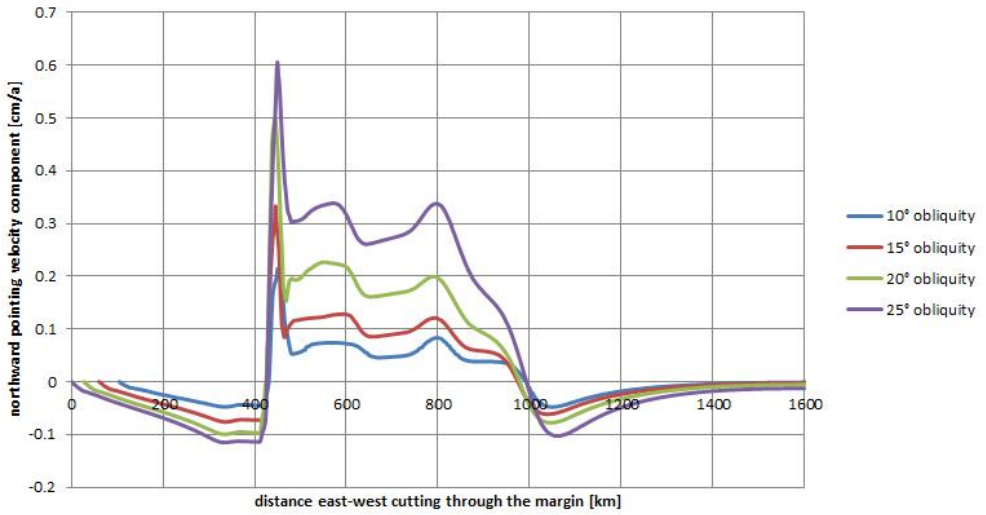

Figure 1.25. Northward directed velocity component [cm/y] against the distance from the trench [km; x- axis in the model] for the NVZ model set up in flat slab angle setup (20°) without a continental weakness and obliquity angles from γ = 10° to γ = 25°. The curves are shifted such that they align with the 25° obliquity margin.

As observed in earlier chapters, the velocity peaks at the plate margin. Here (Figure 1.25), the velocity decreases almost immediately, which has also been observed earlier in cases without a continental weakness. Also, the velocity components peak higher for larger obliquity angles.

With the preceding experiments of Case Study I, it can be concluded that the geometry of the subducting slab as well as of the plate margin and the strength property of the continental crust influence the dynamics of the subduction zone. As expected, the obliquity angle is the major factor: considering a case of no to very small obliquity angle, no strain partitioning is observed in the continental crust regardless of the other parameters subduction dip angle or continental crustal weakness (Figures 1.15, 1.22, 1.25). For an increasing obliquity angle also the width of the sliver increases (Figures 1.22, 1.25). The presence of a continental weakness is favoring the sliver formation and enhancing the width exceeding from the plate margin to the continental weakness (Figure 1.20). The probably least influence on wide sliver formation has the subduction dip angle in the setting of a normal, parabolic subduction. It holds true that a very shallow subduction angle at the plate margin is resulting in strain partitioning and margin parallel high velocities (Figures 1.18, 1.19). This area at the plate margin is however equivalent to that of the accretionary prism and strain partitioning here is not accounted for as continental crustal sliver movement. The increase of subduction dip angle more likely reduces the area of strain partitioning to the accretionary prism (Figures 1.18, 1.19). Overall, Case Study I gives good insight on subduction zone dynamics in a normal subduction setting.

Case Study II – Oblique subduction and continental deformation in the Peruvian Flat Slab Segment (3°S - 14°S)

In Case Study II I present numerical experiments, designed to represent the oblique subduction zone of the Peruvian Flat Slab Segment region (PFSS, 3°S - 14°S) and to investigate the dynamics of the continental plate. The main emphasis of this case study lies on how the dynamics of the continental crust are influenced by a flat, step-shaped subducting slab. In particularly this regards the development of a continental sliver. Additionally, I present a set of experiments investigating the effect of varying the plate convergence obliquity angle in this setting.

As in Case Study I, the runs presented in this case study are performed as purely mechanical experiments. The effects of temperature-dependent rock properties on continental deformation in an oblique subduction setting are investigated in the succeeding Case Study III.

2.1 Model design

The reference model is set up to represent the PFSS of South America with a step-shaped subducting slab, moderate convergence obliquity and homogeneously strong continental crust. Figure 2.1 shows the reference model design, defining the initial slab geometry, topography, material properties and velocity boundary conditions.

The model dimensions as well as the surface geometry are the same as in Case Study I. The model has a 1600 by 1600 km base with a 160 km thickness. The topography is again initially defined to coarsely resemble the Andes. The Andes rise from land level to form a 96 km wide to 4 km elevated plateau following the contour of the subduction margin at a distance of about 200 km. This uppermost surface is not allowed to move during neither of the runs, which means that erosion and sedimentation are artificially suppressed.

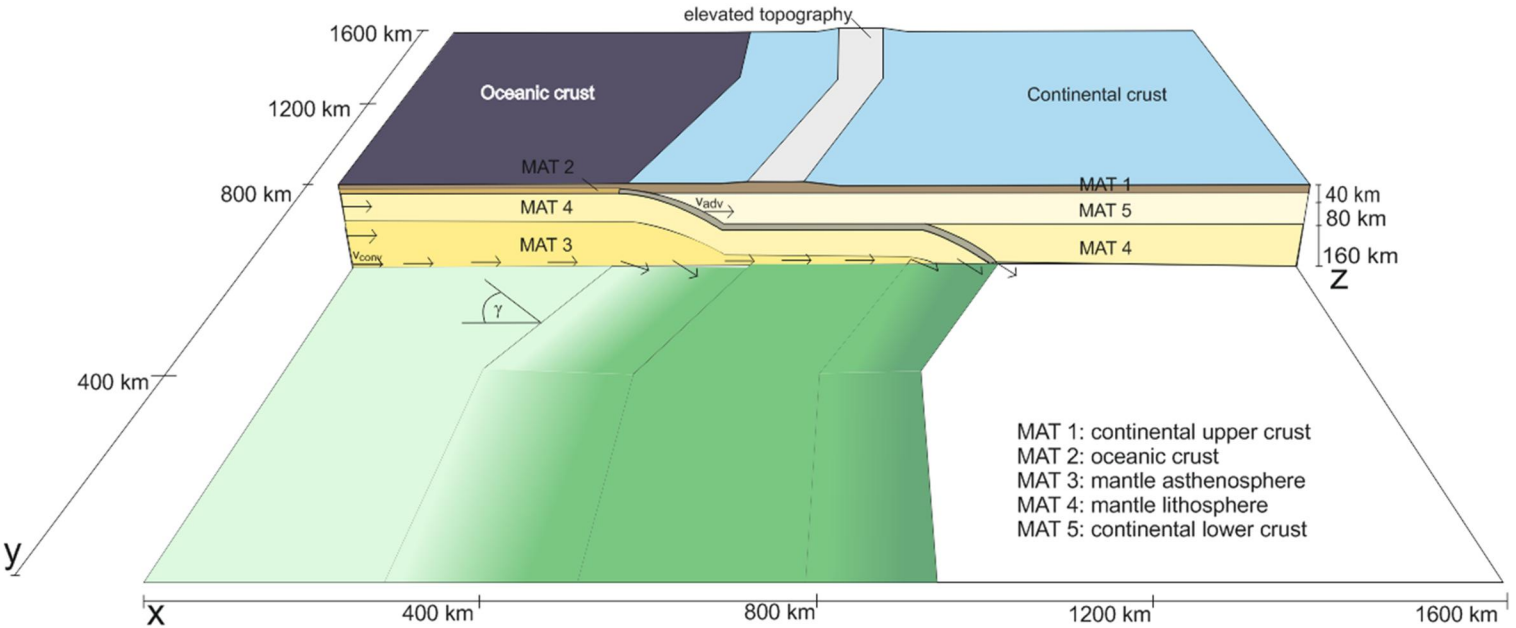

Figure 2.1. Schematic view of the model design. Cross section: advancing subduction (v_{adv} = $2 cm/a$) with total convergence velocity of v_{conv} = $7\,cm/a$. Material prperties for materials one to five are given in Table 2. Upper surface: generalized topography of the study area. Basal surface: oblique (angle γ) zone of subduction between Nazca Plate and South American Plate. The grey zone (slab) has the same material properties as its host material except a friction angle of φ = 2° instead of φ = 4°(slab) and φ = 15°(continent), respectively. The green color represents the velocity field: constant influx velocity (v_{conv} = $7\,cm/a$) on the left (oceanic side), in agreement with the slab geometry increasing downward velocity component where the slab bends and zero velocity on the right (continental side).

Boundary conditions

The velocity boundary conditions are very similar to the NVZ experiments in Case Study I. The plate convergence velocity is v_{conv} = $7cm/a$. The subduction velocity is defined to be v_s = $5cm/a$, which results from the plate convergence velocity being reduced by v_{adv} = $2cm/a$ of subduction zone advance into South America. This way, the margin of the two plates stays in the center of the modeling domain. The influx velocity along the left-hand side of the model domain is constant and balanced by the outflux at the bottom of the model domain. The model base has a velocity field designed to produce flat-slab subduction (Figure 2.1) and is the controlling factor for the subduction. Material is removed along the base of the model beneath the first descent of the slab following its parabolic shape and beneath the second descent, where the slab exits the model domain. A schematic velocity field of the reference model is shown in Figure 2.2.

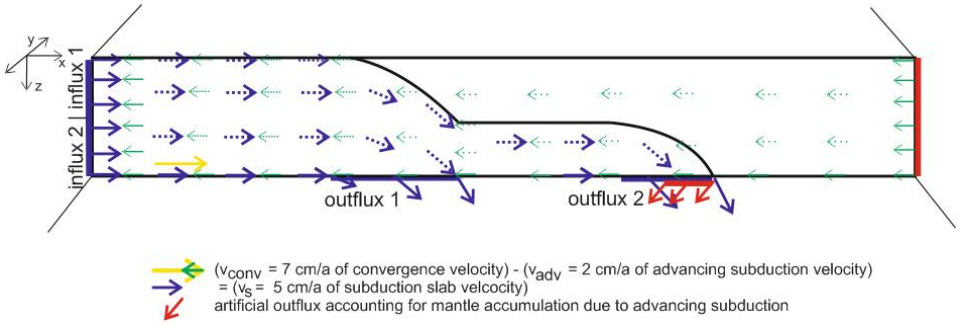

Figure 2.2. Cross section view of the PFSS model with a schematic representation of the velocity field. Only velocity vectors at the boundary of the domain are prescribed, the dashed vectors inside are illustrating a possible flow field. Blue arrows represent the subduction slab velocity fixed with v_s = $5cm/a$ at x=0; the influx areas (left-hand side blue bold lines) are balanced against the outflux areas 1 and 2 (blue bold line at the base of the model domain); green arrows are uniform over the entire area with v_{adv} = $2\ cm/a$ and represent the advancing character of the subduction zone; together with the slab velocity, the total plate convergence velocity is v_{conv} = $7cm/a$ (e.g., Stern, 2004; Gutscher et al., 2000; Nocquet et al., 2014); red arrows represent the outflux of continental mantle required to balance the influx at x = 1600 km.

Under the assumption of crustal shortening only, mantle lithosphere is removed at the base of the model. This is done by introducing a mantle outflux velocity in front of the subducting slab. This is needed because otherwise the way advancing subduction is implemented in this model causes the mantle to pile up and to rise to the surface.

Material parameters and properties

Case Study II is like Case Study I based on purely mechanical experiments and also material properties are similar in both case studies. The assigned material properties shown in Table 2 are largely adopted from Currie, et al. (2015) and Beaumont, et al. (2006) as well as references therein.

Table 2. Material properties used in the mechanical model

	Material 1 **continental upper crust**[*1] 0- ~30 km	**Material 2** **oceanic crust** [*1] 0-14 km	**Material 3** **mantle astheno-sphere**[*2] 80-160 km	**Material 4** **mantle litho-sphere**[*2] ocean: ~30-80 km cont.: 80-160 km	**Material 5** **continental lower crust**[*1] ~30-80km
density (kg/m^3)	2800	3000	3250	3250	2900
viscosity pre-factor (Pa s$^{-1/n}$)	10^{29}	10^{29}	10^{20}	10^{29}	10^{29}
cohesion (MPa)	1	1	1	1	1
friction angle	15 (2)▪	4 (2)▪	– –	15	15 (2)▪
approx. rock rheology	Wet Quartzite	Dry Maryland Diabase	Olivine	Olivine	Dry Maryland Diabase

[*1] Currie, et al., 2015
[*2] Beaumont, et al., 2006

▪ friction angle in the material (friction angle in the weakened area within the material)

As in Case Study I, the plastic and viscous behavior of the materials is controlled by the nominal viscosity and the previously described Mohr-Coulomb criterion (cf. Chapter 3.2.2). The cohesion is prescribed with $c = 1$ MPa for all frictional plastic materials. In this case study, the reference experiment is the PFSS with a homogeneously strong continental crust (cf. Figure 2.1). The part of the slab actively being subducted is kept weak using a friction angle of $\varphi = 2^{\circ}$. Other areas have a friction angle of $\varphi = 4^{\circ}$ (slab) and $\varphi = 15^{\circ}$(continent); these values are chosen based on general rock strengths (Chapter 3.1.5) and previous calibrating and spin up model runs.

Model assumptions and restrictions

As in Case Study I is the uppermost surface fixed for the entire run also in the experiments presented in Case Study II. This is a simplification of the models necessary due to numerical

problems the free surface was causing. A properly deforming uppermost surface would influence the isostasy and gravity of the whole system. However, keeping the surface similar to the topography observed in the study area and especially maintaining a stable numerical solution is of necessary importance.

The thickness of the oceanic crust has been doubled compared to the NVZ model (Case Study I). The model was not able to detect the weak slab in the horizontally traveling part of the subduction zone for a thickness of two elements only (two elements correspond to ~7 km thickness) and the thickness needed to be increased to four elements (corresponds to 14 km). This is especially important in the thermo-mechanical models of Case Study III, where the slab is also marking the interface between warmer continental lower crust and mantle lithosphere and the cold oceanic slab. For consistency, this thickness is employed in all PFSS experiments.

As in the previously shown case study, subduction is driven by the basal velocity boundary condition and not gravitationally, which restricts the free development of the subduction zone. Still, subduction initiation is not in the focus of this study but rather the deformation and dynamics of the continental crust. Because kinematic subduction (the basal velocity field) is ensuring slab subduction even though the buoyancy required for subduction may not exist in these models, simplifications regarding the lithospheric layer thickness are not crucial to the model results.

This case study is purely mechanical and thus the largest drawback is the simplicity regarding temperature dependence. No temperature calculations and thus no temperature-dependent rock properties are included. Thermal weakening of the slab might cause better developed continental sliver movement. Especially, as in the PFSS the slab is shielding the continental crust from mantle heat flux, strain partitioning might be enhanced as the crust itself stays rather strong. A second, contradicting possibility is that the thermo-mechanical properties weaken the crust such that there will be no sliver movement at all. These questions are taken up in Case Study III.

Run time

The run time of the experiments presented in this study is 1 Ma. As mentioned in Case Study I, longer run times of at least 2 Ma would be desirable in order to achieve run times of geological significance. However, as the models at time zero are roughly representing the shape of the present day Andes and the velocity field is approximating the mechanical solution of a subduction zone, qualified statements on the purely mechanical model experiments can be made even after geological short run time.

2.2 Results and Discussion

The chart shown in Figure 2.3 shows the two main topics of this case study, how they relate to each other and to the research area:

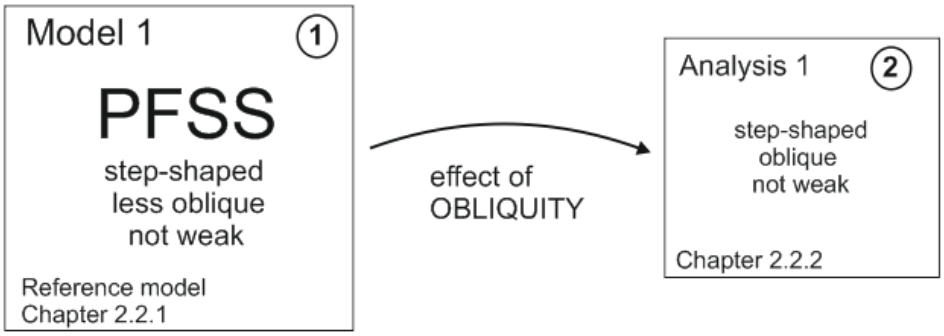

Figure 2.3 Chart showing the main experiments of Case Study II: Model 1 (the reference model) represents the PFSS and Analysis 1 is investigating the obliquity angle in this setting. The key steps are to compare *step-shaped* subducting slab (Gutscher, et al., 1999), *less oblique* (20°; Yepes, et al., 2016; Ramos, 1999) and *oblique* (25°-40°; Velosa, et al., 2012; Mc Nulty, et al., 2002) as well as *not weak* (no continental crustal weakness, i.e. uniform continental strength).

The reference model (Model 1) is designed to represent the PFSS, which is characterized by a flat, step-shaped subducting slab, an obliquity angle of about γ = 20° (e.g. Yepes, et al., 2016; Ramos, 1999) and no dominant continental crustal weakness, e.g. in form of a volcanic arc. The slab reaches down to a depth of about 80 – 90 km with a subduction angle of about 35° (Gutscher, et al., 1999), and flattens out to travel almost horizontally between 300 km and 700 km to finally bend down again. In Chapter 2.2.1 this model is presented and discussed. To investigate the influence of the debated (cf. PFSS, Chapter 2.3) obliquity angle in the PFSS, Chapter 2.2.2 discusses the results of a set of experiments with varying obliquity angle.

Note that the model design and the study area are axisymmetric to each other. While the study area, the PFSS, is oblique 20° to the south and sliver movement would be observed southward, the model design is 20° oblique to the north and sliver movement is expected to be observed northward. The general findings in this Case Study are directly transferable.

2.2.1 The PFSS – Model 1 (reference model)

The PFSS is described having an obliquity angle of 20° (e.g. Yepes, et al., 2016; Ramos, 1999) and a slab bending down with normal subduction angle and moving straight underneath the continental at a depth of about 90 km for about 300 km (Gutscher et al., 1999) as shown in described in Chapter 2.3. Figure 2.4 shows the initial condition of the model before deformation.

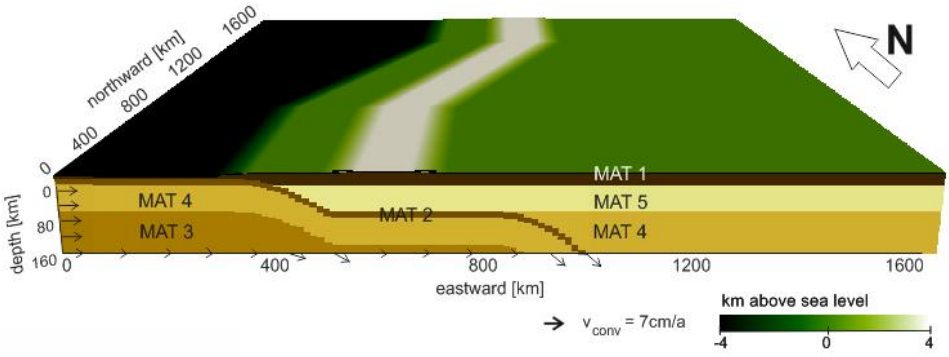

Figure 2.4. Initial experiment set up of the PFSS reference model. Upper surface: model topography. Side view: material numbers 0 to 5 referencing to the listed materials in Table 2. Black arrows represent the velocity boundary conditions.

Results

In the PFSS experiment no significant strain partitioning or continental sliver movement is noticeable. In the following velocity plots and strain rate plots after 1 Ma run time are shown to analyze the experiment.

Figure 2.5 shows the northward directed velocity component of the PFSS model in two color schemes: panel (a) for 0 – 2 cm/a to allow comparison with the other experiments and panel (b) for 0 – 0.3 cm/a to allow further interpretation.

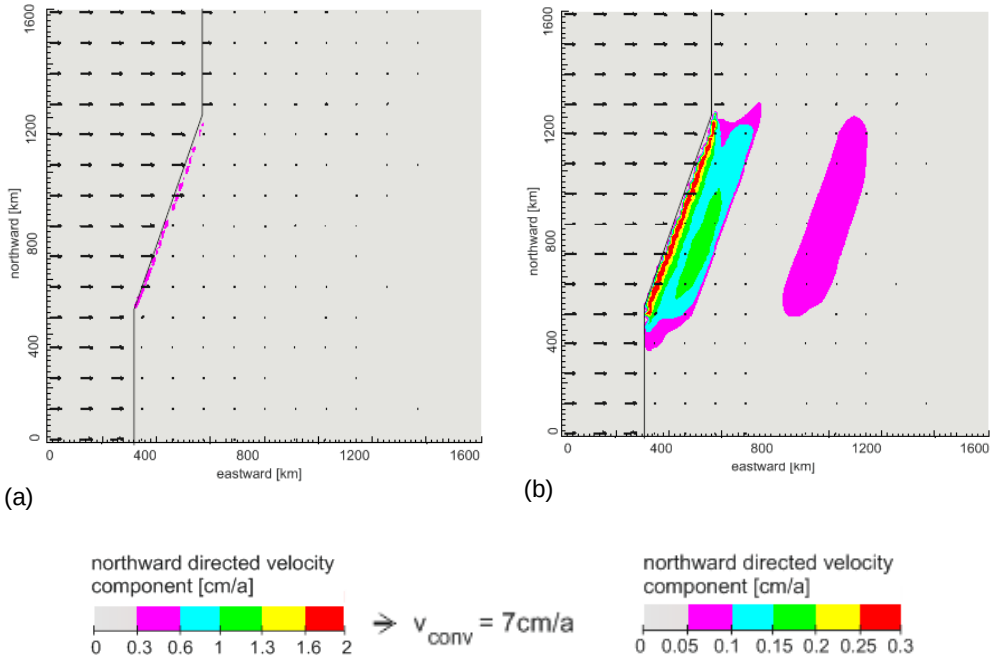

Figure 2.5. Top View of the northward directed velocity component in the PFSS slab environment: (a) color scheme from 0 to 2 cm/a (b) zoomed color scheme from 0 to 0.3 cm/a. The black line marks the margin between the two plates and black arrows are representing the overall velocity field.

The northward directed velocity component has almost vanished in the PFSS experiment compared to the pronounced sliver movement in the NVZ experiments of previous case study (Chapter 1.2.1).

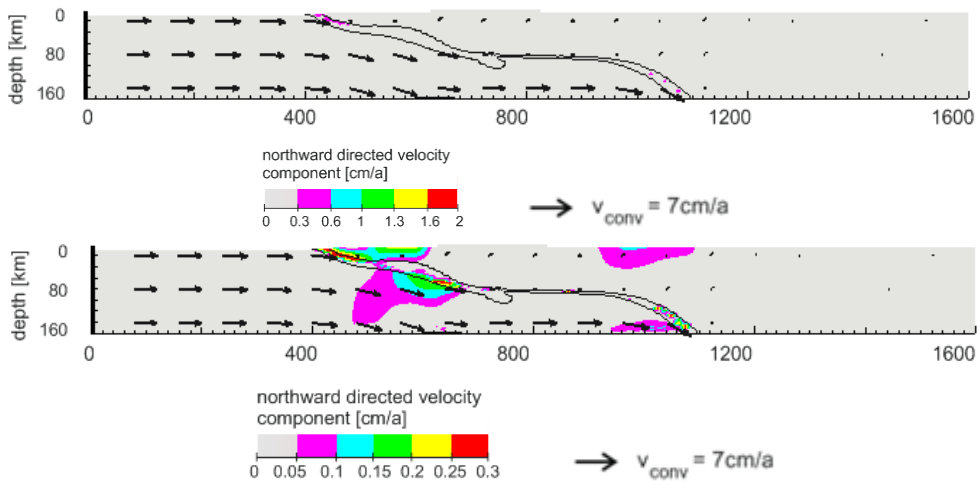

Figure 2.6. Side view of the northward directed velocity component in the PFSS slab environment: (a) color scheme from 0 to 2 cm/a (b) color scheme from 0 to 0.3 cm/a. The black contour marks the weak oceanic slab and black arrows are representing the total velocity field.

From both the previous figures (Figures 2.5 and 2.6) one sees that the northward motion in the PFSS is restricted to the area above the slab and to the area above the onset of the second descend of the slab, in the latter part of its horizontal part. Northward velocities of 0.1 to 0.2 cm/a are slightly smaller than observed GPS velocities of around 0.5 cm/a (Figure 2.7; Nocquet, et al., 2014).

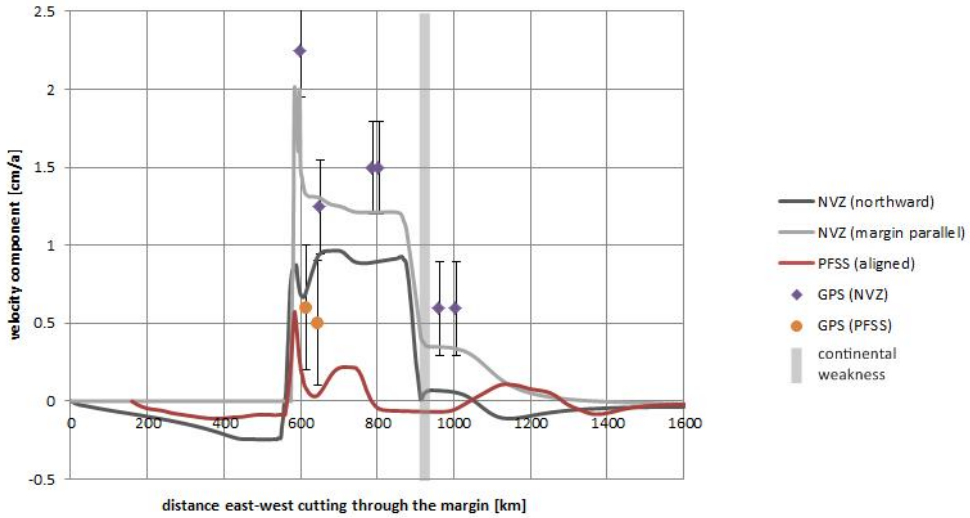

Figure 2.7. Velocity components [cm/a] against the distance from the trench [km; x- axis in the model] for the NVZ (northward (dark grey) and margin parallel (light grey) velocity component) and SW-NE GPS velocities (purple) observed in the area (cf. Case Study I, Figure 1.15; Mora-Páez, et al., 2016 and Veloza, et al., 2012 and references therein; error bars ±0.3cm/a) and for the PFSS model (red) (the curve representing the northward directed velocity component is shifted such that the margin is aligned with NVZ curve) and GPS velocities (orange) (approximately NW-SE) observed in the area (Veloza, et al. 2014; error bars ±0.4cm/a). Grey bar indicates the position of the continental weakness.

Figure 2.7 summarizes the essence of Case Studies I and II: moderate strain partitioning is interrelated with oblique subduction and a weak zone in the continent parallel to the margin; and weak, distributed margin-parallel mass transport is consistent with a lower obliquity and uniformly strong continent. The NVZ velocity profile shows a clear sliver movement for the

area between the plate margin and the continental weakness (grey bar in Figure 2.7), while the PFSS velocity profile (curve is shifted such that the plate margin is aligned with the NVZ model) has despite directly at the margin two small velocity peaks close to the margin and above the latter part of the flat slab. Velocity predictions obtained in the experiments are within the uncertainty in the observed GPS velocities (Figure 2.7) or slightly smaller.

First of all, the results suggest, that the obliquity angle is the main influence on the formation of strain partitioning in the continental crust. This is reasonable, as without oblique motion there is no oblique component triggering division of velocity components. Secondly, a weak zone, be it in the continental crust itself (NVZ) or in form of a flat slab (PFSS) enhances strain partitioning. However, the obliquity angle in the PFSS experiment is possibly too small to cause sliver movement in the continental crust, even though the flat horizontal slab offers a weak zone to break the otherwise homogenously strong continental crust. Analogue models have shown that models with a homogeneous crust do not experience strain partitioning unless the obliquity angle is about 45° (Burbidge and Braun, 1998). It is also noticed in the cross-section views (e.g. Figure 2.6; 2.8) that the first parabolic shaped slab flattens out in the uppermost tens of kilometers. This is possibly a direct result of the velocity field being only defined at the base of the model and not prescribing the path of the slab within the model. This alteration is however only small and thus only insignificantly influencing the dynamics of the overriding plate.

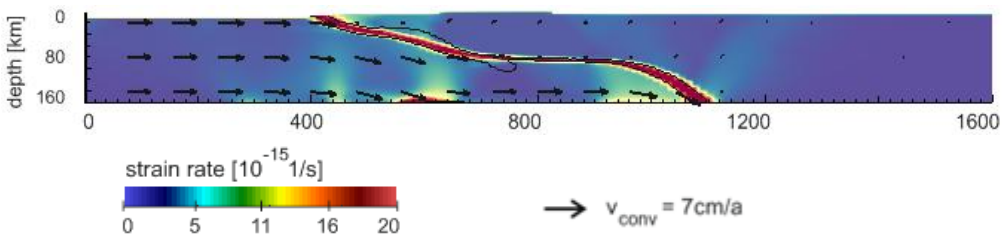

Figure 2.8. Strain rate after 1 Ma run time PFSS model. The strain rate is colored between 0 and 20 · 10^{-15}1/s. The velocity field is represented with black arrows. Side view cut through the middle of the model (y = 800 km).

Strain rates shown in the cross-sectional (Figure 2.8) are only high in the slab itself and not in the continental crust above. This means, deformation mostly takes place in the subducting slab and its close vicinity. However, the magnitude of the velocity field is decreasing from the plate margin toward the interior of the continent (black arrows in Figure 2.8). This indicates some degree of shortening in the continent, which relates to the formation and uplift of the Andes.

2.2.2 Effect of changes in the obliquity angle

In the following the effect of changes in the obliquity angle in the PFSS subduction setting is investigated. In Chapter 2.2.1 the PFSS slab geometry was designed with an obliquity angle of 20°. According to literature, however, the obliquity varies between γ = 10° and γ = 20° (e.g. Knezevic Antonijevic, et al., 2015; Yepes, et al., 2016) and may be up to γ = 40° (e.g. Ramos, 1999; Velosa, et al., 2012; Pulido, et al., 2014). For this reason, a short series of experiments regarding the effect of obliquity in the PFSS is presented and discussed.

Keeping the model design of the PFSS (Figure 2.1) and gradually increasing the obliquity angle from 25° to 40° (Figures 2.9 and 2.10) leads through different possible configurations of the PFSS.

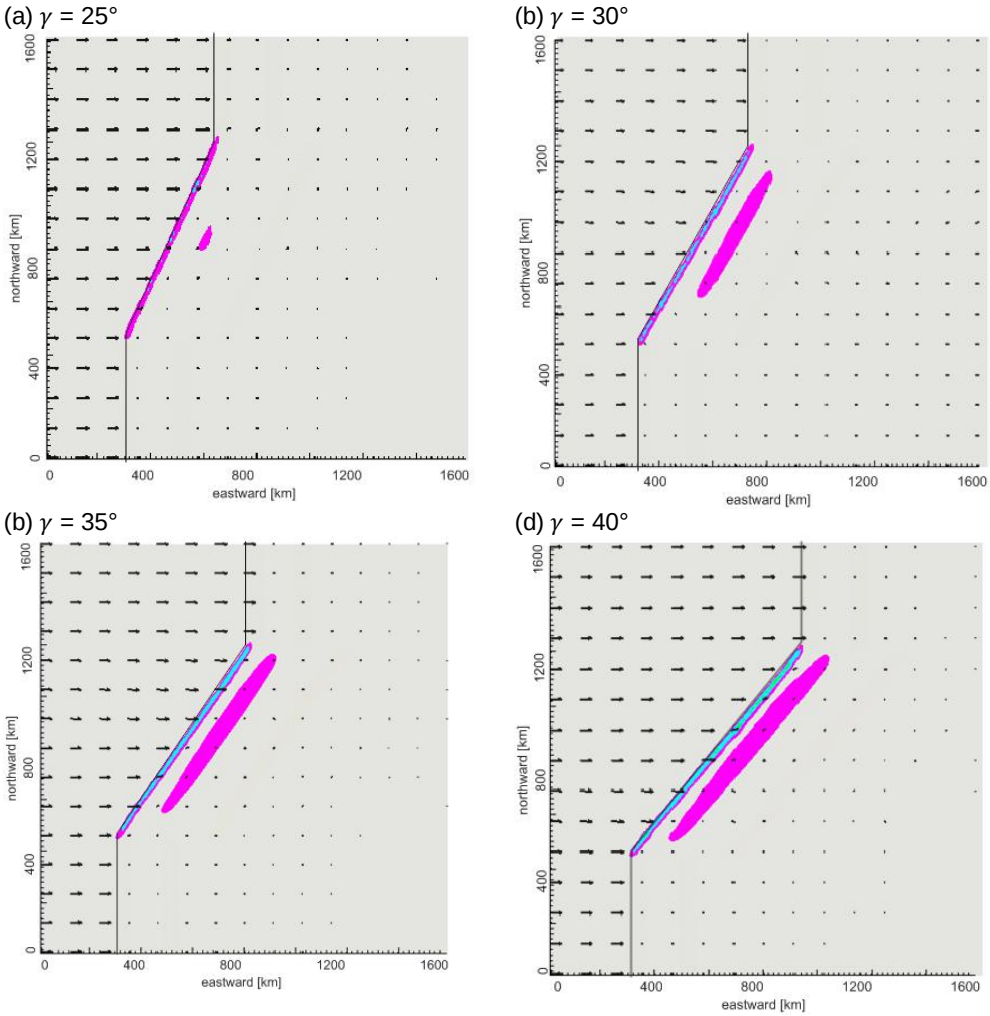

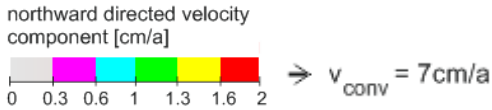

Figure 2.9. Top View of series of obliquity angle changes in the PFSS slab environment. The obliquity angle varies in increments of 5° from γ = 25° (panel a) to γ = 40° (panel d). The color scheme is indicating the positive northward directed velocity component. The black line marks the margin between the two plates and black arrows show the velocity field at the surface.

(a) γ = 25°

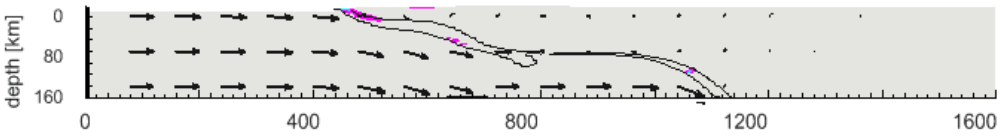

(b) γ = 30°

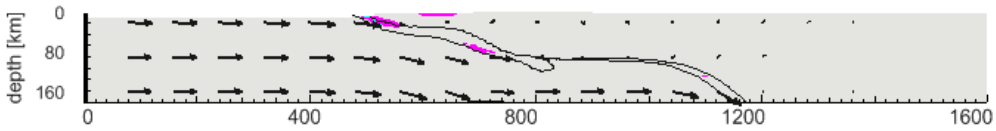

(c) γ = 35°

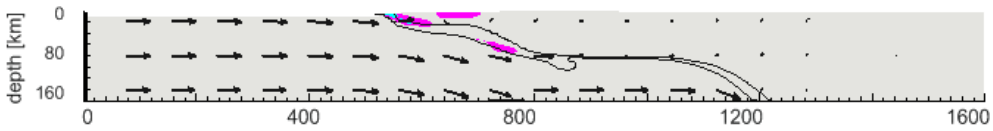

(d) γ = 40°

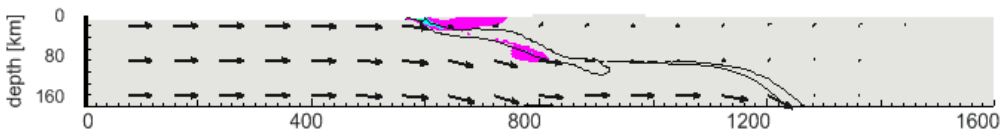

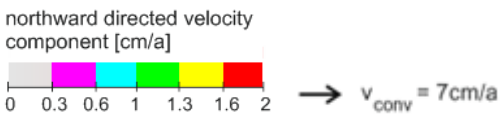

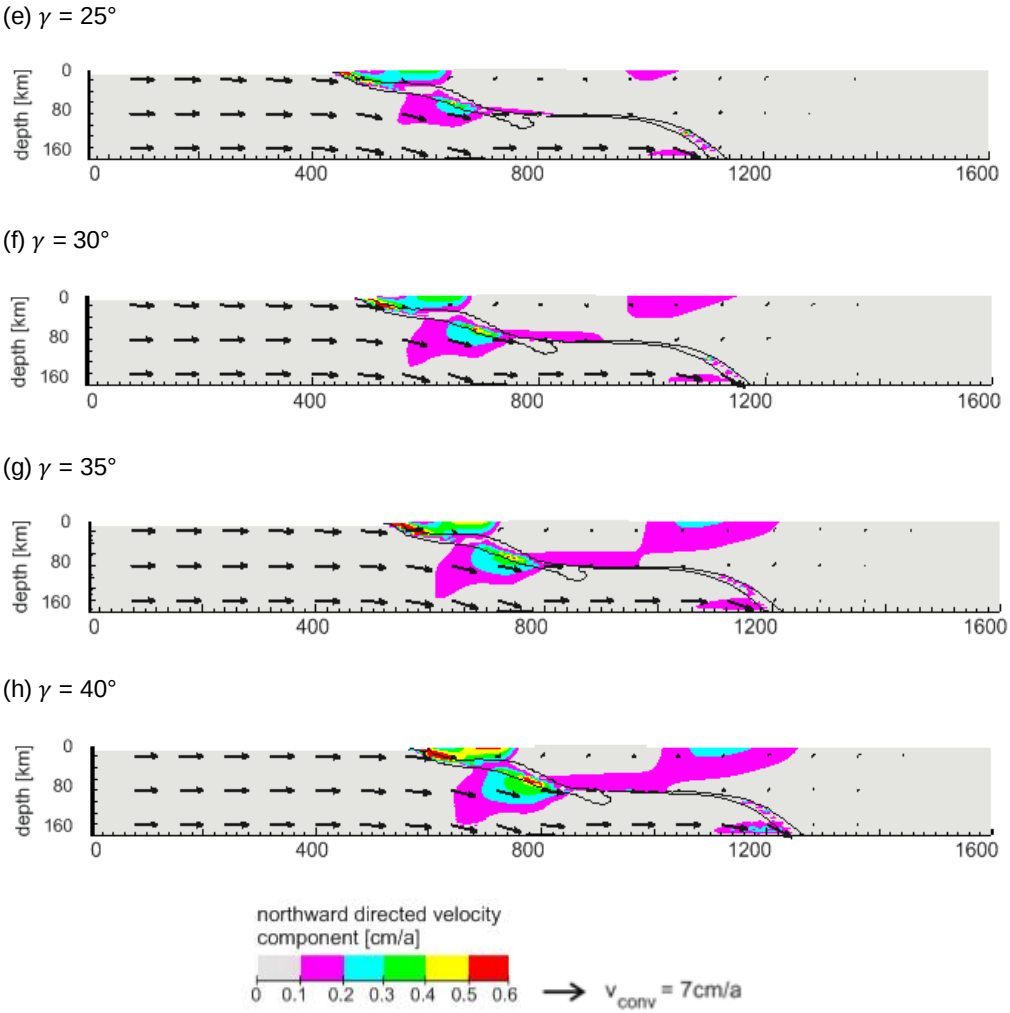

Figure 2.10. Cross-sectional view of a series of obliquity angles in the PFSS slab environment. The obliquity angle varies in increments of 5° from γ = 25° (panel a) to γ = 40° (panel d). The color scheme indicates the positive northward velocity component. Panels (e) to (h) display the same runs from γ = 25° (panel e) to γ = 40° (panel h) in a color scheme ranging from 0 cm/a to 0.6 cm/a. A black contour line shows the position of the weak slab and black arrows show the overall velocity field.

The main area of strain partitioning is observed above the slab close to margin. This area increases with increasing obliquity angle and velocities up to 0.6 cm/a are observed (Figure 2.10, panels (a) – (d)). Additionally, sliver movement is observed above the latter part of the horizontal section of the subducting slab for obliquity angles larger than 35° (Figure 2.10, panels (e) - (h)). Here, the magnitude is reaching around 0.3 cm/a. It can be suggested that the weak slab travelling horizontally defines a predefined breaking point similar to a weakness in the continental crust. The continental crust would more likely take up the

oblique motion from the incoming plate and a sliver move margin parallel above the slab. Also, the size of the basal shear zone is increased compared to the normally subducting slab of the NVZ and strain partitioning is prompted at lower obliquity angles. Secondly, with decreasing obliquity, overall strain partitioning or sliver movement is significantly decreasing, too. In the 40° obliquity case (Figure 2.9 and 2.10, panel (d), or. 2.10 (h)) velocities up to 0.9 cm/a, 0.55 cm/a and 0.25 cm/a are achieved at the margin, close to the margin and above the horizontally traveling slab, respectively. In the small obliquity angle (25°) case (Figure 2.9 and 2.10, panel (a) or. 2.10 (e)), however, the area of northward movement is vanishingly small and maximal up to 0.6 cm/a, 0.35 cm/a and 0.15 cm/a.

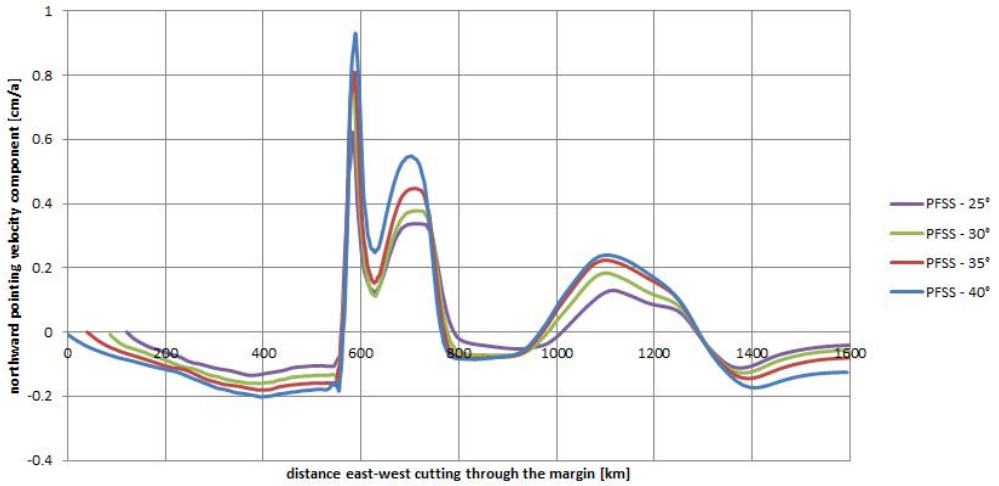

Figure 2.11. Northward directed velocity component [cm/a] as a function of the distance from the trench [km; x- axis in the model] for the PFSS models without a continental weakness. Obliquity angles vary from 25° (purple) to 40°(blue) in 5° steps. The curves are shifted such that the margins align with the 40° obliquity case.

Note that Figure 2.11 plots the northward directed velocity for the different obliquity angles in the PFSS setup against the distance, cutting east-west through the model. This underestimates the magnitude of the margin parallel velocity component but is in order to have one reference frame (north) for all obliquity angles. One can clearly see, that the velocity profile of all four models follow the same shape: at the margin, the velocity increases to peak between 0.6 cm/a and 0.9 cm/a for obliquity angles between 25° and 40° and decrease to a minimum where the slab bends to travel horizontally. Above the flat zone, the northward velocity component increases to 0.15 cm/a - 0.25 cm/a to subsequently decrease to zero where the slab sinks deeper into the mantle. The weak horizontal slab influences the sliver movement but the decreasing obliquity angle has the superior influence.

Comparing these results to observations in nature, with sliver movement of around 0.5 cm/a, the model results are consistent with an obliquity of 30° or less.

Case Study III – Effects of temperature-dependent rock properties on oblique subduction and continental deformation, Northern Volcanic Zone (5°N - 3°S) and Peruvian Flat Slab Segment (3°S - 14°S) of the Andes

In order to advance the understanding on the dynamics of oblique subduction zones gained through mechanical numerical experiments (case Studies I and II), this Case Study is revisiting the Northern Volcanic Zone (5°N - 3°S) and the Peruvian Flat Slab Segment (3°S - 14°S) of the Andes with a thermo-mechanical model. The thermo-mechanical models include temperature-dependent rock properties and couple temperature field and heat flow calculations with purely mechanical calculations.

3.1 Model design

The general design (including the size of the model domain, the geometry of the plates and the velocity boundary conditions) of the reference models of this case study is identical to those used in the mechanical model of Case Study I (Figure 1.1) representing the Northern Volcanic Zone (NVZ) and in Case Study II (Figure 2.1) representing the Peruvian Flat Slab Segment (PFSS). In order to be able to set different material properties for the mantle lithosphere in the oceanic versus the continental part, the continental mantle lithosphere is assigned a new material number. Instead of five, there are now six material domains (see Figure 3.1) which are described in Table 3. The velocity boundary conditions of the purely mechanical models in the previous chapters and these temperature-dependent models are the same: The plate convergence velocity is $v_{conv} = 7cm/a$ and subduction velocity is defined to be $v_s = 5cm/a$, which results in $v_{adv} = 2cm/a$ of subduction zone advance into South America. See Figure 1.2 (NVZ) and Figure 2.2 (PFSS) for the velocity boundary conditions.

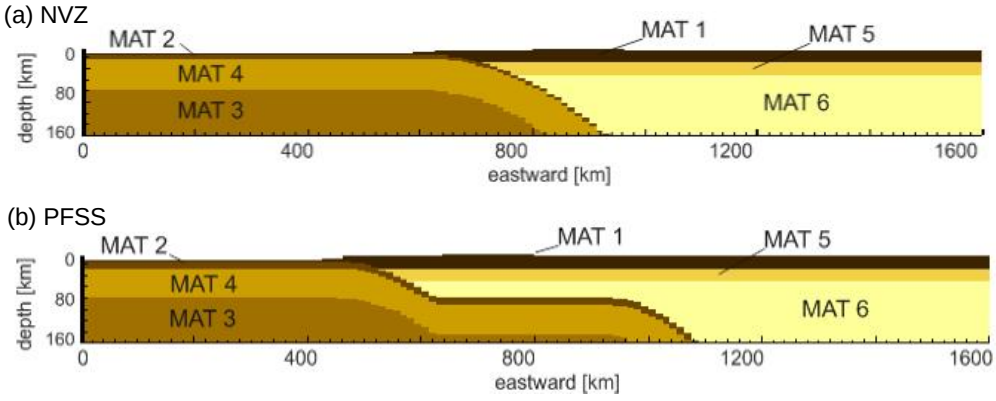

Figure 3.1. Material domains for the (a) NVZ and the (b) PFSS experiment. MAT 1: continental upper crust, MAT 2: oceanic crust, MAT 3: mantle asthenosphere, MAT 4: oceanic mantle lithosphere, MAT 5: continental lower crust, MAT 6: continental mantle lithosphere. The material properties are described in Table 3.

Thermal model

The initial temperature fields are based on analytical solutions and are shown in Figure 3.2. On the oceanic side of the subduction zone, the geotherm corresponds to the temperature field of a roughly 10 Ma old cooling oceanic lithosphere, which agrees approximately with ages of the oceanic lithosphere at the plate margin (Cobbold and Rossello, 2003). To calculate the geotherm a cooling half-space model (Stein and Stein, 1992) was used. The geotherm of the continental side is based on the steady-state temperature field of an old continental lithosphere (Chapman, 1986). Both calculations are using thermal properties shown in Table 3. This measure is significantly reducing the run time necessary to reach reasonable (i.e., comparable to nature) temperature fields. The temperature at the base is initially 1300 °C on both sides (on the oceanic side this is defined through the half-space cooling model and on the continental side temperatures of the steady state field reach to 1286 °C). These temperature fields described above are applied at the far ends of the subduction zones. Underneath the slab, isotherms follow the shape of the subducting slab and temperatures increase from a pivot point along the normal to the slab surface. This pivot point is in the NVZ model (Figure 3.2a) at the base of the model directly underneath the onset of subduction. In the PFSS model (Figure 3.2b) there are two pivot points, one underneath the margin at depth where the slab travels horizontally and one at the base underneath the zone where the slab begins to subduct again beyond the flat-slab segment. Underneath the horizontal part of the slab, isotherms are horizontal and temperature is increasing towards the base of the model. This adjustment in temperature field is realized by discretizing the temperature field for steps in depth of ~12 km for simpler implementation.

Additionally, in the NVZ model a hot (900 °C) area was included in the upper part of the continental crust (around 20 km beneath the surface and 150 km form the margin) to simulate a magma chamber underneath the volcanic arc of the NVZ. The position from the plate margin is a typical position for subduction zone volcanism (e.g. Stern, 2002). The implemented magma chamber is permanent and continuing over the whole distance of the oblique segment and is thus one end-member for a volcanic arc implementation, but only used as an example to demonstrate its effect.

A constant basal heat flux boundary condition of 20 mW/m^2 beneath the continent was defined (see Figure 3.2).

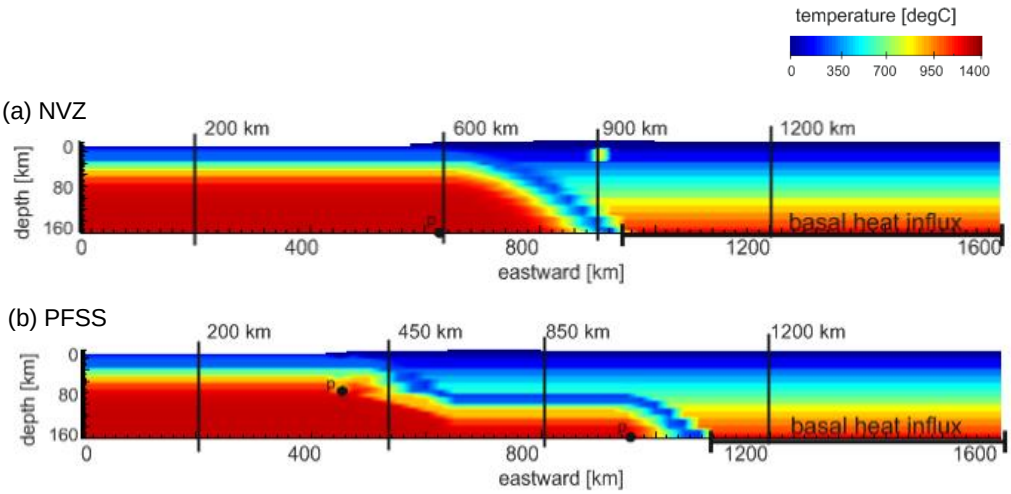

Figure 3.2. Initial temperature field for the (a) NVZ and the (b) PFSS experiment. Pivot points for initial temperature field alteration are indicated with p. Vertical lines indicate the positions of strength profiles shown throughout this Case Study. The bold black line indicates the area in which a basal heat influx of 20 mW/m^2 is applied. Side views cut through the middle of the model domain (y = 800 km).

In order to evolve model temperatures with the combined effects of heat conduction and advection from the initial temperature field (especially around the magma chamber), a temperature spin up is implemented. For this, temperature field calculations and velocity field (mechanical) calculations are decoupled from each other after the initial model spin up time. This means that an initial velocity solution is calculated at the start of the experiment, but then fixed while the temperature field iterates through 20 Ma of heat transfer. After this, the temperature and velocity field calculations are coupled again. Figure 3.3 illustrates this procedure, which saves not only computational power, but also a large amount of run time. The total run time for the coupled thermo-mechanical part of the experiment is about 1 million years. This is the time referred to in the time specification in the temperature and velocity plots.

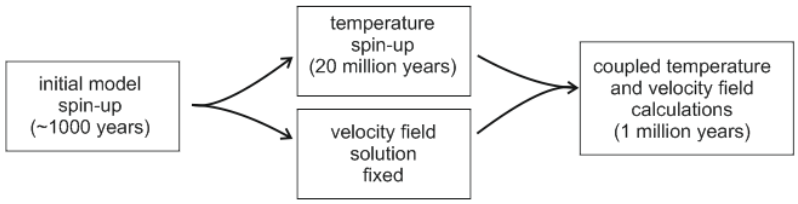

Figure 3.3. Temperature spin-up procedure implemented in the code in order for the initial temperature field to reach towards a geophysically consistent state within reasonable long run times.

Material parameters and properties

In contrast to the purely mechanical experiments presented in Case Studies I and II, temperature dependent rock properties are defined for this experiment. Assigned material properties (Table 3) are largely adopted from Currie, et al. (2015) and Beaumont, et al. (2006) as well as references therein, and are based on test runs adjusted in order to achieve reliable results. None of the material properties shown in Table 3 are temperature dependent themselves. They either represent a fixed average value (e.g., the thermal conductivity) or are themselves not temperature dependent (e.g., the viscosity is affected by the temperature field and its evolution in time, but the viscosity pre-factor is not).

Material 1, the continental upper crust, is given the rheological properties of wet quartzite (Gleason and Tullis, 1995). A viscosity pre-factor (or 'scaling factor') $f = 5$ approximates stronger composition than pure wet quartzite. The oceanic crust, material 2, is defined with dry Maryland diabase properties (Mackwell, et al., 1998), although $f = 0.1$ accounts for a weaker hydrated crust. The continental lower crust, material 5, a dry Maryland diabase rheology, with a lower density and a strength coefficient of $f = 0.1$. Material 6, the continental mantle lithosphere, is defined with an olivine rheology (Chopra and Paterson, 1984) with $f = 250$ (NVZ), $f = 5$ (PFSS), respectively. Higher values of f reflect dehydration and melt depletion of mantle lithosphere during deformation. The high scaling factor of the mantle lithosphere for the NVZ experiments has been shown in test runs to be necessary in order to prevent horizontal flow of material toward the South American continent at the base of the model domain.

The oceanic mantle materials, material 3 (mantle asthenosphere) and material 4 (oceanic mantle lithosphere), are defined with olivine rheologies as well, but are, however, set to be independent of temperature. With activation energy 0 kJ/mol is the viscosity power law (see Equation 3.30 in Chapter 3) only dependent on the viscosity pre-factor. This has shown to be the only measure to keep the velocity field of the slab and the oceanic part of the subduction zone reasonable. As the materials listed are not changing under temperature and the material is still conducting heat this is no severe violation.

Table 3. Material properties used in the thermo-mechanical experiments

	Material 1 **continental upper crust**[*1] 0- ~30 km	**Material 2** **oceanic crust**[*1] NVZ: 0-7 km PFSS: 0-14 km	**Material 3** **mantle asthenosphere**[*2] 80-160km	**Material 4** **oceanic mantle lithosphere**[*2] NVZ: ~20-80 km PFSS:~30-80 km	**Material 5** **continental lower crust**[*1] ~30-50km	**Material 6** **continental mantle lithosphere**[*2] 50-160 km
power law exponent n	4	4.7	1 △	1 △	4.7	4.48
density (kg/m^3)	2900	3000	3250	3250	2900	3250
viscosity pre-factor (Pa s$^{-1/n}$)	$2.92 \cdot 10^6$	$1.91 \cdot 10^5$	10^{29} △	10^{29} △	$1.91 \cdot 10^5$	$7.75 \cdot 10^4$
cohesion (Pa)	10^6	10^6	10^6	10^6	10^6	10^6
friction angle	15	4(2)■	--	--	15	15
viscosity scaling factor f	5	0.1	5	5	0.1	NVZ: 250 PFSS: 5
therm. conductivity (W/mK)	2.5	3.2	3.2	3.2	3	3
heat capacity (J/kgK)	750	800	800	800	750	750
vol. heat roduction (µW/m^3)	1	0	0	0	0	0
diffusivity (m/s^2)	$1.14 \cdot 10^{-6}$	$1.3 \cdot 10^{-6}$	$1.3 \cdot 10^{-6}$	$1.3 \cdot 10^{-6}$	$1.37 \cdot 10^{-6}$	$1.2 \cdot 10^{-6}$
activation energy (kJ/mol)	223	485	0 △	0 △	485	485
approx. rock rheology	Wet Quartzite	Dry Maryland Diabase	Olivine	Olivine	Dry Maryland Diabase	Olivine

[*1] Currie, et al., 2015
[*2] modified from Beaumont, et al., 2006

■ friction angle in the material (friction angle in the weakened area within the material)
△ materials 3 and 4 are linear viscous with temperature independent viscosity

Two main sets of experiments are considered: one representing the NVZ (Chapter 3.2.1) and one the PFSS (Chapter 3.2.2). The oceanic crust of the subducting slab is kept weak in both experiments with a friction angle of $\varphi = 2^{\circ}$. Other parts of the slab have a friction angle of $\varphi = 4^{\circ}$. The previously mechanically (via friction angle; see Case Study I and II) induced continental weakness in the NVZ model is now thermally induced with the described hot magma chamber (see Figure 3.2a).

Lithospheric strength envelopes have been calculated from the material properties shown in Table 3 using 2D Mohr-Coulomb frictional plastic (Equation 3.24) and Power-law viscous (Equation 3.30) strength. The plots for the initial conditions are presented in Figure 3.4 for both, the NVZ and the PFSS models. The envelopes are from the middle of the model domain (y = 800 km) and positioned in the oceanic (eastward x = 200 km) and continental (eastward x = 1200 km) part of the numerical model, respectively. See Figure 3.2 for the position of the strength profiles.

(a) NVZ (200 km – ocean)

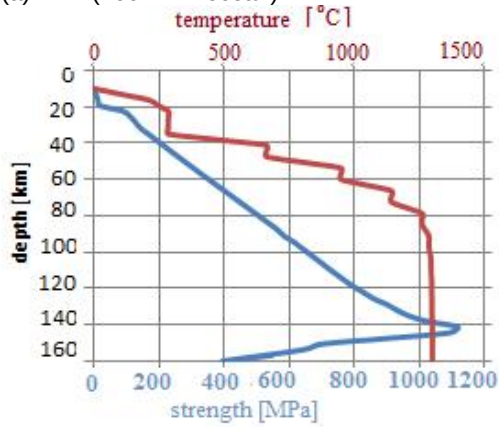

(b) NVZ (1200 km – continent)

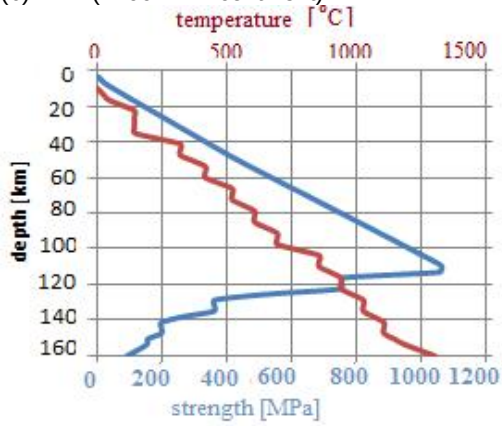

(c) PFSS (200 km – ocean)

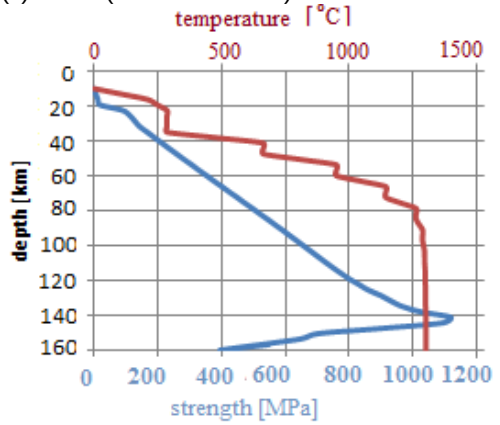

(d) PFSS (1200 km – continent)

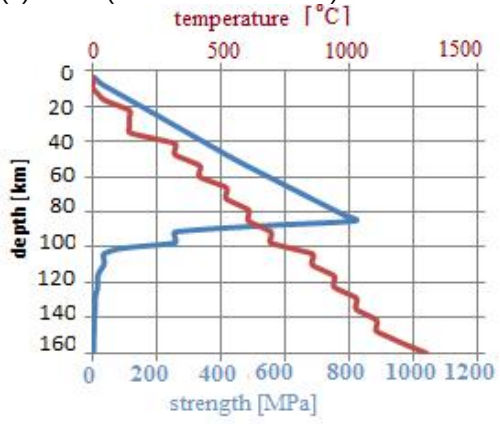

Figure 3.4. Initial strength envelopes (blue, scaling at the bottom axis) and geotherms (red, scaling on the top axis) for NVZ and PFSS model on the oceanic and continental side of the subduction zone, respectively. (a) NVZ, eastward 200 km (oceanic) (b) NVZ, eastward 1200 km (continental), (c) PFSS, eastward 200 km (oceanic) and (d) PFSS, eastward 1200 km (continental). Note different scale of strength [MPa] for the panel oceanic strength versus continental strength.

The material properties in the NVZ and PFSS experiments are the same except for the viscosity scaling factor f in the continental mantle lithosphere, which is strengthened in the NVZ experiment by employing $f = 250$ instead of $f = 5$ as in the PFSS experiment (see Table 3). The otherwise identical design of both experiments results in the same strength profile on the oceanic side and a similar on the continental side. On the oceanic side, frictional plastic strength (not influenced by the viscosity scaling factor f) reaches a strength of around 20 MPa in the crust. Beneath the crust, strengths of the modified olivine theologies (see Table 3) reach maximum values of 1100 MPa at 140 km depth (Figures 3.3a and c). On the continental side (Figure 3.3b and d), frictional plastic strength reaches to the depth of around 110 km (NVZ) and 80 km (PFSS), respectively, where deformation transitions to ductile. Strength reaches around 1100 MPa (NVZ) and 800 MPa (PFSS), respectively. The difference in strength is because of the different scaling factor.

Despite the alteration in the oceanic mantle lithosphere and mantle asthenosphere, the strength profiles are overall representing typical values (e.g. van der Pluijm and Marshak, 2004; Stüwe, 2007; Turcotte and Schubert, 2014).

Note that the strength profiles cut through the whole depth of the model domain, such that the sea level and land level (not elevated) are at 10 and 5 km model depth, respectively. Also, the oceanic crust is not weakened by application of a lower friction angle at 200 km eastward of the western model boundary. This is only applied in the subducting part of the oceanic crust (eastward of the plate margin). Figure 3.4 shows the initial strength profiles and due to the initial temperature field discretization the geotherms are “bumpy” in the beginning. This smoothens out during the 20 Ma temperature spin-up.

Model assumptions and restrictions

The model assumptions and restrictions are generally the same as in the previous case studies. Still, the upper most surface is fixed during the entire run. Further is subduction driven kinematically and not initiated gravitationally due to the depth range of the numerical experiments.

In these models however, heat flux and temperature field derivations are included in the experiments. This means, that lithosphere and crust are weakening as a result of heat transport. A weakened slab and a thermally induced continental weakness can possibly increase the sliver movement observed in the continental plate due to decreasing sliver

resisting force. However, as the heat flux is not restricted to the pre-defined weak zones, it could heat up the surrounding lithosphere, which in turn might weaken the entire continental crust from the margin to the pre-defined weakness. In this entirely weakened and near jelly-like crust deformation and shear zone formation would be less localized, which probably would result in reduced sliver movement.

In order to initialize the temperature field, analytical solutions based on the material properties given in Table 3 are implemented. As mentioned above, the geotherm on the oceanic side resembles a temperature field of an about 10 Ma old oceanic lithosphere, whereas the geotherm on the continental side is a steady-state solution. These pre-calculated temperature fields reduce the run time, since they approximate what is observed in nature, but are a step away from a fully self-evolving, complete thermo-mechanical model. The initial implementation of the geotherms is not a smooth curve and even though properties (e.g. surface heat flux) are initially correct, evolution of the temperature fields through run time (i.e. leveling out initial bumps) might cause deviations form expected values. The initial geotherms rather underestimate than overestimate temperature, which might cause a colder temperature regime in the uppermost crust. This is not believed to influence the dynamics of the continental crust significantly. For one, a colder crustal layer is heating up during the temperature spin up and secondly, the uppermost tens of kilometers are deforming in a plastic manner.

Test runs have shown that the mantle lithosphere on the continental side is too weak in the NVZ experiment with the model design. Material along the base of the model is horizontally moving into the continent, shifting the entire subduction zone about 300 – 400 km inland. A scaling factor $f = 250$ increases the viscosity of the mantle lithosphere (see Table 3). This and the temperature field being adjusted to the geometry of the slab (see Figure 3.2a), together with the temperature spin up (see Figure 3.3) avoid this behavior. Test runs have also shown that the altered viscosity properties in the oceanic mantle lithosphere and mantle asthenosphere are necessary to keep the overall velocity field of the slab reasonable (this means, generally horizontally towards the subduction zone). This modification is not ideal, but necessary because of the size of the model domain. Upper-mantle-scale models with gravitationally driven subduction, for instance, may not need these adjustments. Importantly, I believe these model design choices do not change the first-order upper crustal dynamics in the overriding plate, and thus having the proper velocity field is prioritized over the material properties of the mantle lithosphere.

Run time

The run time of the in this case study presented experiments is 1 Ma for the NVZ and PFSS experiments. This means, the run time of the coupled (temperature and velocity field) thermo-mechanical model. A separate temperature field spin up time of 20 Ma is interposed (see Figure 3.3). The system is designed to resemble the topography of the modern Andes. This initial geometry, the temperature field adjusted to the geometry of the subducting slab

as well as the temperature spin up allow qualified statements even after in geological time scale short run times.

3.2 Results and Discussion

This case study is investigating the influence of temperature dependent rock properties on the dynamics of the subduction zones of the NVZ and PFSS (Figure 3.5).

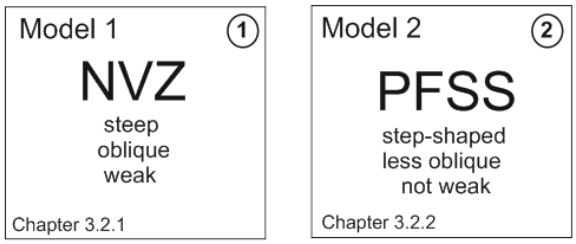

Figure 3.5. Chart showing two main experiments of Case Study III: Model 1 is representing the NVZ and Model 2 is representing the PFSS. The key words compare *steep* (35°) parabolic shaped subducting slab (Gutscher, et al., 1999; Stern, 2004; Ramos, 1999), *step-shaped* subducting slab (Gutscher, et al., 1999), *oblique* (40°; Velosa, et al., 2012; Mc Nulty, et al., 2002) and *less oblique* (20° obliquity; Yepes, et al., 2016; Ramos, 1999) as well as *weak* (continental crustal weakness) and *not weak* (no continental crustal weakness, i.e. uniform continental strength).

Model 1 is designed to represent the NVZ (cf. Case Study I), which characteristics are reduced and simplified to the key points steep (35°) subduction angle, obliquity angle of about 40° and the presence of a continental crustal weakness, which might be represented by a volcanic arc, pre-existing fault systems, or boundaries of stronger crustal blocks. Model 2 is representing the PFSS (cf. Case Study II) which is characterized by a flat, step-shaped subducting slab, a smaller angle of obliquity (20°) and no continental crustal weakness.

3.2.1 The NVZ – Model 1

At time step zero, the model is the same as in the previous Case Study I (cf. Figure 1.4). The initial temperature field is shown in Figure 3.2a. Only, the continental weakness is now induced thermally not mechanically.

Running the experiment

The coupled thermo-mechanical model of the NVZ is run for 1 Ma years (see Figure 3.3). Temperature and velocity fields as well as strength profiles of the experiment are presented below.

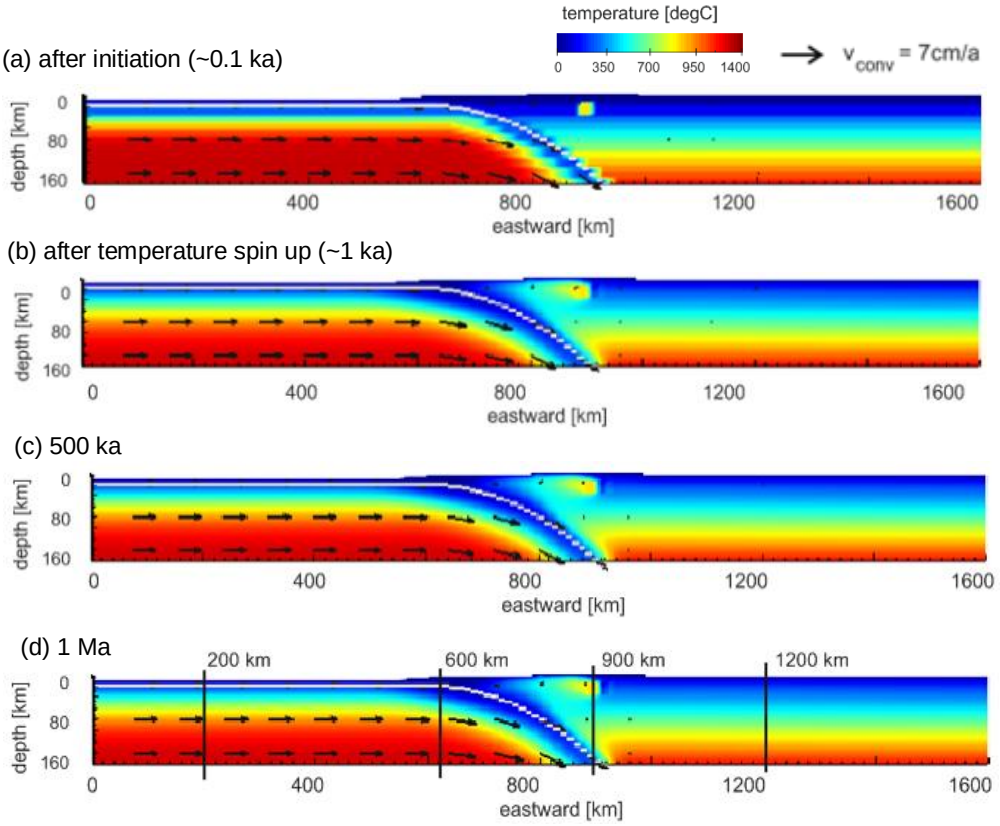

Figure 3.6. Temperature profile and velocity field of the NVZ model after (a) initiation (~0.1 ka), (b) temperature spin up (~1 ka), (c) 100 ka and (d) 1 Ma coupled run time. White band outlines the oceanic crust. Panel d indicates positions for strength profiles shown in Figure 3.7. Side view cut through the middle of the model (y = 800 km).

The initially defined temperature field was already adjusted to the temperature field of an oceanic lithosphere, a continental lithosphere and the subduction zone (compare Figure 3.2a and Figure 3.6a). This means that the slab is traveling in a cold environment. This is usually observed in subduction zones. After the temperature spin up (Figure 3.6b) the temperature field is smoothened (especially in the slab and around the magma chamber). The initially sharply bounded magma chamber is diffusing out, towards the slab.

The temperature field in the continental side is not expected to change much, since the input geotherm is based on a steady-state solution. Still, heat advection from the magma chamber

imposed onto the steady state solution, the implemented heat production in the crust and the basal heat flux contribution are expected to alter the temperature field. The oceanic side is expected to cool down. Starting from a geotherm corresponding to an about 10 Ma old oceanic lithosphere, running the experiment (temperature spin-up) for 20 Ma results in an about 30 Ma old lithosphere and thus cooler environment (Figures 3.6c and d). The difference is, however, relatively small and instead of in the temperature plot, better observed in Figure 3.7, which shows the geotherm and strength envelope of the model after 1 Ma coupled run time.

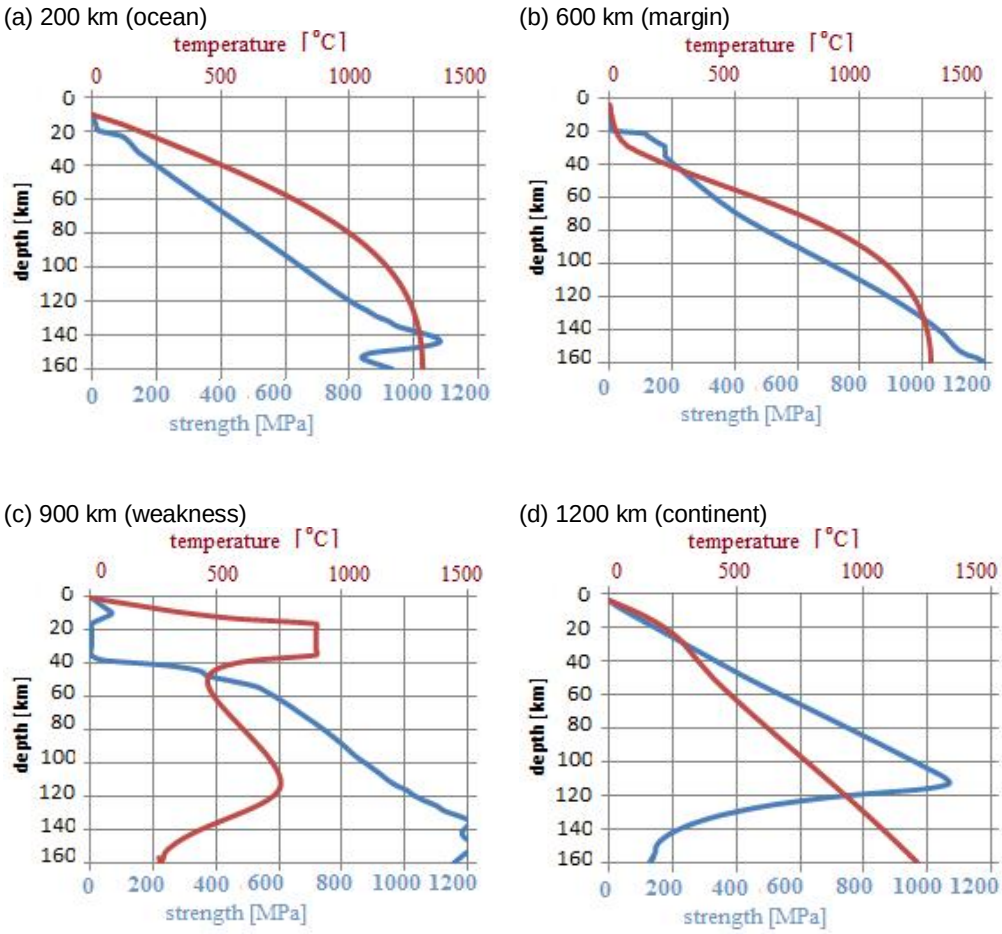

Figure 3.7. Strength envelopes (blue, scaling at the bottom axis) and geotherms (red, scaling on the top axis) of the NVZ experiment after 1 Ma coupled run time. All profiles are from the middle of the model (y = 800 km) and in positions (a) 200 km, (b) 600 km, (c) 900 km and (d) 1200 km (see Figure 3.6d).

The strength in the oceanic part of the subduction zone (Figure 3.7a) does not change much; maximum strength of 1100 MPa is reached at about 140 km depth. The temperature is slightly decreasing, which is expected for an aging and cooling oceanic lithosphere. The strength of the continental part (Figure 3.7d) has not changed significantly either. Maximum strength of ~1050 MPa is still reached at around 110 km depth. The geotherm is altered in the uppermost ~30 km, the continental upper crust is beginning to warm up as a combined effect of heat advection from basal heat influx, heat production in the continental upper crust and the magma chamber. Even though the initial temperature field is including heat production, the "bumpy" steady state initialization (Figure 3.4) is only an approximation and the system needs run time to reach a "smooth" steady state. In the margin (Figure 3.7b) frictional behavior comparable to the oceanic crust (Figure 3.7a) is observed. Here, underneath the slab, the oceanic regime is prevailing (compare mantle lithosphere in Figure 3.7a). The strength profile cutting through the continental weakness, magma chamber, (Figure 3.7) clearly shows the abrupt increase in temperature between depths of 15 and 35 km, where the magma chamber is positioned. The temperature below is increasing along the geotherm of the continental lithosphere until the profile cuts through the slab and decreases. The strength profile is showing frictional behavior of the crust. Strength is abruptly decreasing in the area of the magma chamber due to high temperature. The strength profile is following the continental lithospheric strength profile (compare Figure 3.7d) underneath the magma chamber and when cutting through the slab and reaching into the oceanic lithosphere strength decreases accordingly. Maximum strengths reach 1200 MPa at around 140 km depth, where the profile cuts through the slab (low temperature). The strength profiles reflect the high strength of the continental mantle lithosphere needed to avoid the basal shearing and flow into the continent (Table 3).

Generally, strength profiles of the continental and oceanic plate (Figure 3.7a and d) are not changing much from the initial state (Figure 3.4a and b) and are thus still in good agreement with what is generally expected (e.g. van der Pluijm and Marshak, 2004; Stüwe, 2007; Turcotte and Schubert, 2014).

The velocity plots (Figure 3.8 and 3.9) show that a well-defined sliver develops in the entire area between the margin and the continental weakness (magma chamber) reaching from the surface to the slab. Sliver movement is initiated close to the margin and expands into the continent, such that a uniform velocity field is obtained shortly after the temperature spin-up of the run (Figure 3.8c, 3.9c). The magnitude of the sliver movement stabilizes during the run and a well-defined, homogenous and high velocity sliver movement with velocity around 1.2 cm/a is observed (Figure 3.8d) above the slab and between the continental margin and the continental weakness.

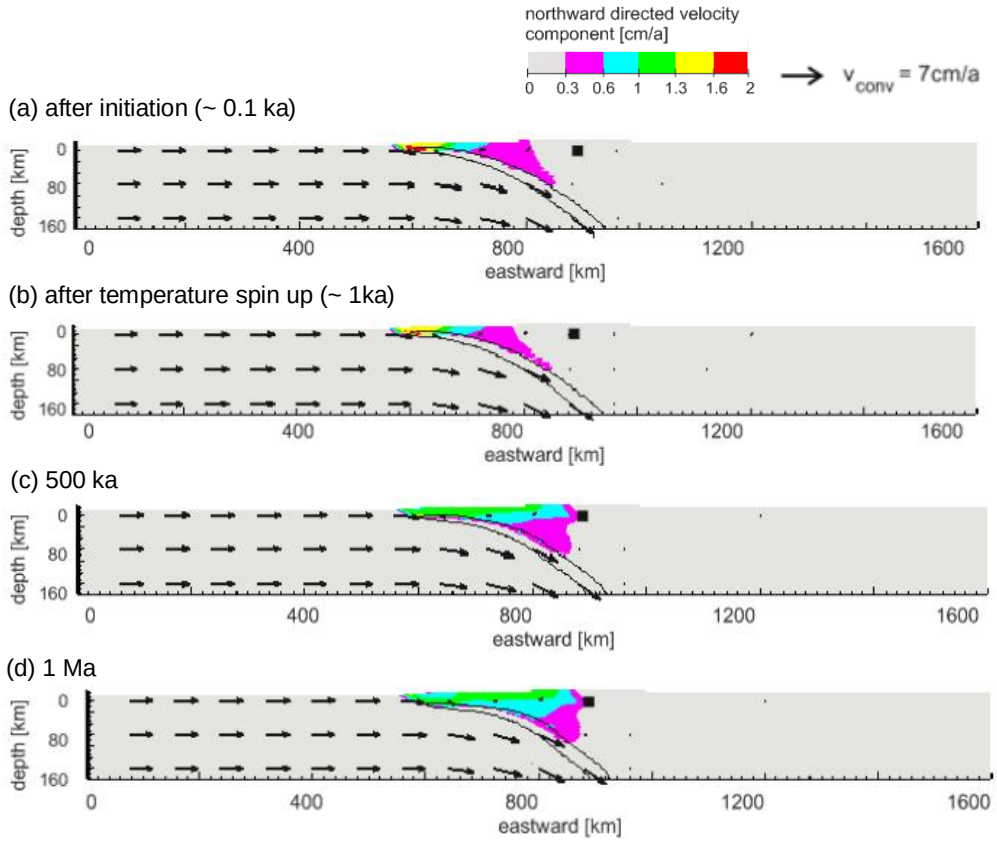

Figure 3.8. Side view of the velocity field (black arrows) and northward directed velocity component (colored for the interval 0 cm/a to 1 cm/a) of the NVZ model after (a) initiation (~0.1 ka), (b) temperature spin up (~1ka), (c) 500 ka and (d) 1 Ma. Black contour line indicates the weak continental slab and the black square the crustal weakness (magma chamber) in the continent.

The total velocity field (black arrows, Figures 3.6, 3.8 and 3.9) shows that the oceanic plate is traveling horizontally until reaching the continental plate margin. It then subducts homogeneously underneath the stationary overriding plate.

In map view of the velocity field (Figure 3.9), the horizontal extent of the sliver at the surface becomes visible. The entire area between the plate margin and the continental weakness is occupied by the homogeneous sliver movement already after short coupled run time (about 500 ka; Figure 3.9a). Staying in this area velocity steadies to 1.2 cm/a in less than 1 Ma run time (Figure 3.9d).

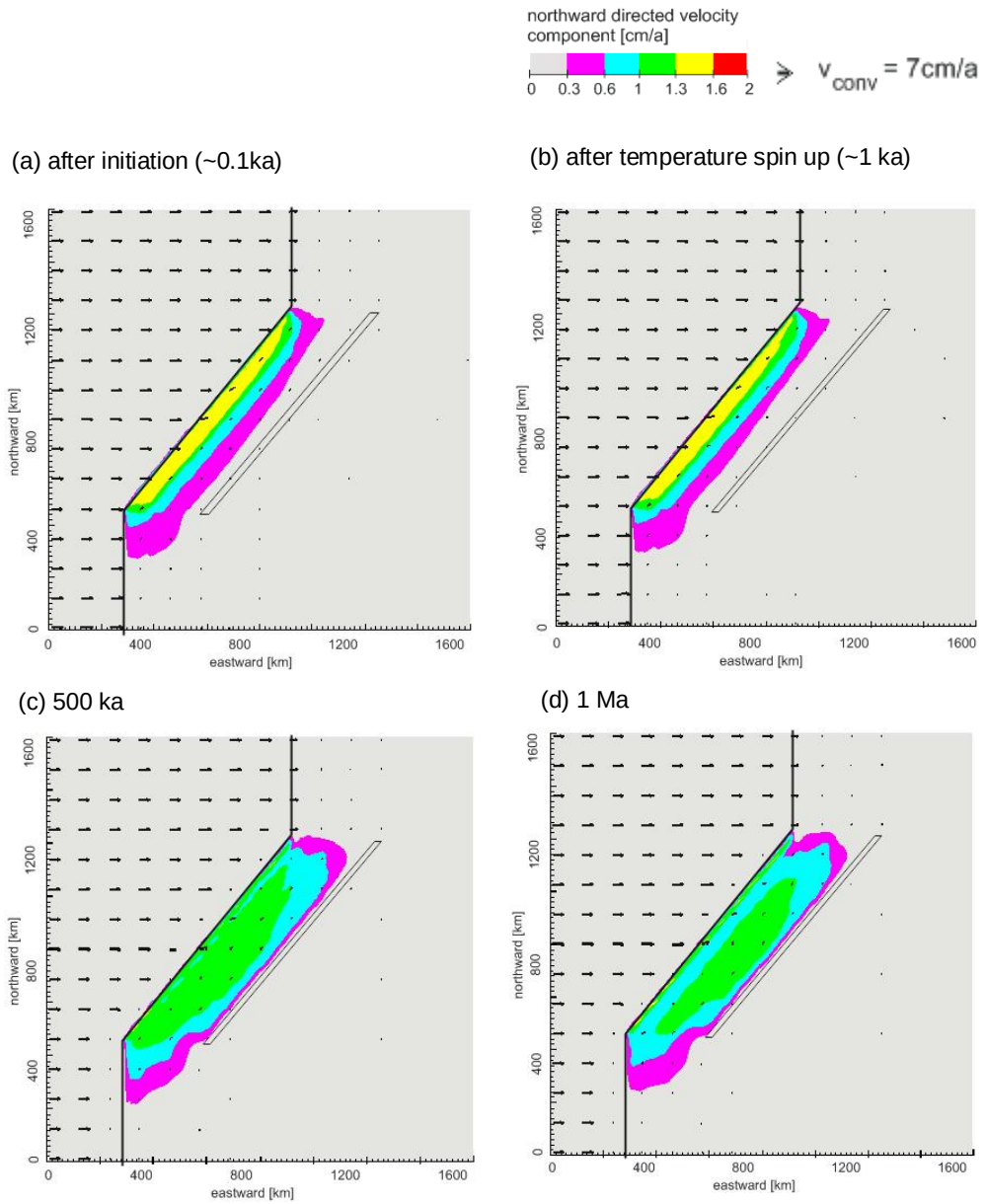

Figure 3.9. Top view of the velocity field (black arrows) and northward directed velocity component (colored for the interval 0 cm/a to 1 cm/a) of the NVZ model after (a) initation (~0.1 ka), (b) temperature spin up (1 ka), (c) 500 ka and (d) 1 Ma coupled run time. Black bold line indicates the plate margin and the contour line marks the approximate position of the continental weakness (magma chamber) below the surface.

The observed sliver movement is in very good agreement with results from the purely mechanical experiments in Case Study I. The spatial extent as well as the velocity magnitude of the sliver is the same in both experiments (compare Figure 3.9 to Figure 1.7b).

Figure 3.10 shows the surface heat flow after 1 Ma year runtime calculated from (near) surface temperatures using Fourier's law. Heat flow values in the far field of the subduction zone are around 60 mW/m^2 on the oceanic and about 44 mW/m^2 on the continental side. Surface heat flow is decreasing towards the margin and increases above the continental weakness. Here the magma chamber is positioned and a peak of heat flux is expected.

Generally, surface heat flow is in good agreement with expected values (e.g. Pollack and Chapman, 1977; Peacock, 1996; Stein, 2003). The values on the oceanic side correspond well to analytical values of a ~30 Ma old oceanic lithosphere (cooling half-space model). The values on the continental side are a bit low. Setting the basal heat flow to 20 mW/m^2 and including a heat production value in the (30 km thick) continental crust of 1 $\mu W/m^3$, we expect values around 50 mW/m^2. This discrepancy might be due to the rough initial implementation of the temperature field. As described earlier, initially correctly obtained values would alter due to leveling of the geotherm during the experiment and deviate from expected outcome. In case this has an effect on the surface heat flow, it does not influence the dynamics of the overriding plate significantly, since the uppermost tens of kilometers are deforming in a frictional plastic manner.

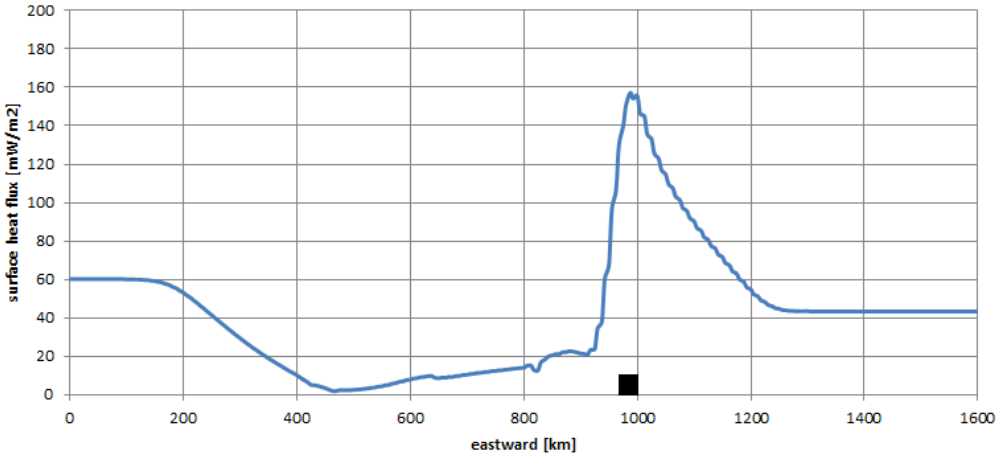

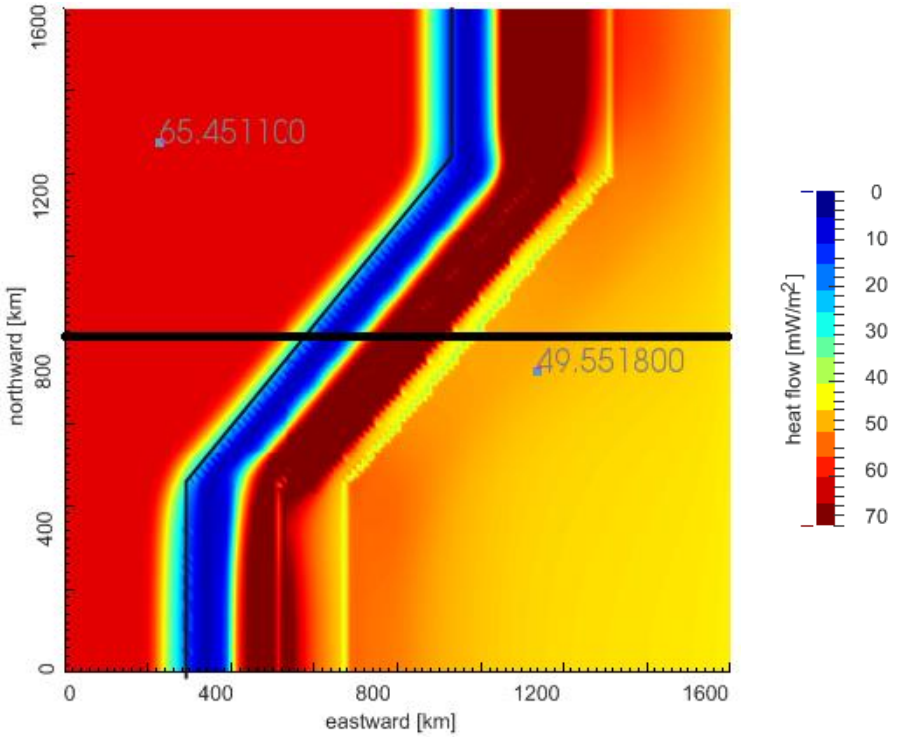

Figure 3.10. Heat flow [mW/m^2] calculated Fourier's law at 1 Ma run time. (a) Surface heat flow graph through the middle of the model (y = 800 km), black square marks approximate position of the magma chamber, (b) map view of surface heat flow with black line indicating the plate margin and bold black line marking the position of the heat flow graph.

The adjusted initial temperature as well as a modified mantle lithosphere and mantle asthenosphere has improved the model results. The implemented magma chamber is a good thermal substitute for the previously only mechanically induced continental crustal weakness. Sliver movement is clearly activated. Strength profiles and overall heat flow pattern are in good agreement to the expected outcome and show consistency of the model. The development of sliver movement in this thermo-mechanical model agrees well with results from the purely mechanical models (Case Study I). This suggests that the purely mechanical models are already a good representor of dynamics in the overriding plate of a subduction zone and that the mechanical calculations work well also in experiments with temperature dependent material properties. With the emphasis on continental crustal deformation is this here presented thermo-mechanical model of the NVZ a satisfying representation of nature and a step towards a fully coupled, freely evolving thermo-mechanical model.

3.2.2 The PFSS – Model 2

The general design of this thermo-mechanical model of the PFSS study area is the same as in Case Study II (see Figure 2.4). The material allocation and the initial temperature field for the PFSS experiment are shown in Figures 3.1b and 3.2b. Table 3 describes the material properties. Note again, that the study area and the model are axisymmetric to each other and potential northward sliver movement in the model corresponds to southward sliver movement in nature. The coupled PFSS experiment runs for 1 million years.

Running the experiment

As the main difference to the purely mechanical experiments presented in Case Study II, this experiment includes temperature calculations. As already noticed in the NVZ thermo-mechanical study is the implementation of temperature dependent material properties while keeping the general mechanical solution of the subduction zones much more difficult than one might expect. While the mechanics of the normal subduction in the NVZ (Chapter 3.2.1) can be retained by manipulating the material properties, is the complicated slab geometry of the PFSS causing artefacts, which cannot be fixed within the approach of kinematically driven plate movements (as done in this study), but would require major changes in model design. In the following, the temperature field, velocity field and strength evolution of the PFSS are presented. Observed anomalies and model design issues are discussed later in the Discussion chapter.

The evolution of the temperature field is shown in Figure 3.11. The initial temperature field (see Figure 3.2b) is accounting for a cooling oceanic lithosphere of ~10 Ma and a continental lithosphere at steady-state, as well as roughly approximating the geometry of the slab. This includes a cold slab, which travels in relative cold environment.

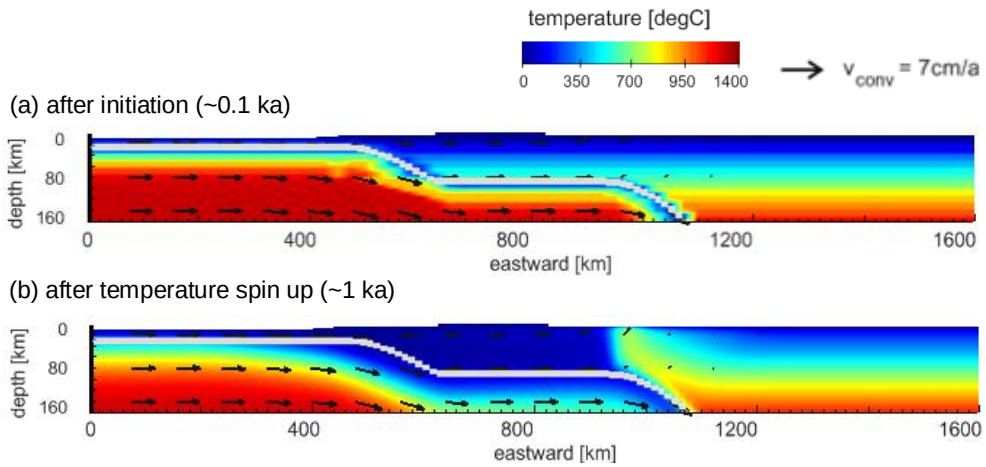

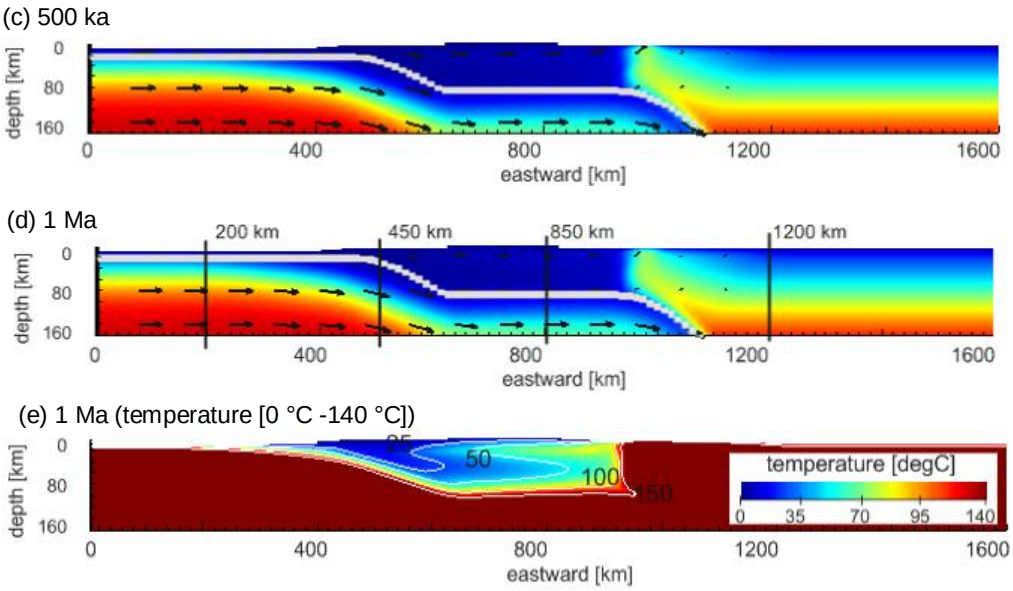

Figure 3.11. Temperature and velocity fields for the PFSS model after (a) initiation (~0.1 ka), (b) temperature spin up (~1 ka), (c) 500 ka and (d) 1 Ma coupled run time. The grey band outlines the oceanic crust. Panel (e) shows the temperature field after 1Ma within the range of 0 °C to140 °C. Contour lines mark the 25 °C, 50 °C, 100 °C and 150 °C borders. Positions for strength profiles shown in Figure 3.12 are indicated in panel (d). The cross sections are located in middle of the model (y = 800 km).

The temperature spin-up is generally smoothing the temperature field. In the continental side (far field) only little change is observed. This is expected, since the input geotherm is based on a steady-state solution. However, temperature field adjustments caused by the rough initial approximation, heat advection from implemented heat production in the crust and the basal heat flux contribution are expected to alter the temperature field. These changes are better observed in the strength and geotherm plots shown in Figure 3.12. The temperature field of the oceanic lithosphere is, at most, cooling slightly in the uppermost kilometers. That is consistent with an aging and thus cooling oceanic lithosphere. The environment around the initially cooler slab shows previously mentioned anomalies in the temperature field. Figure 3.11e underlines that temperatures of only up to 50 °C are observed in depth to ~80 km. A vertical temperature gradient through the area above the horizontal slab is an expected pattern and temperatures are expected to be low (e.g. English, et al., 2003). They are, however, too low. The total velocity field (black arrows in Figure 3.11 and 3.13) is indicating that the overriding plate is not detached from the slab. The continental upper and lower crustal material is dragged along into the continent and a collision-like pattern is observed above the second region of subduction of the slab. This collision causes rock uplift in the

collision zone, which leads to anomalously high temperatures in the continental crust (Figure 3.11) and affects the surface heat flow (see Figure 3.15).

The strength envelope of the model after 1 Ma coupled run time is shown at positions eastward 200 km (oceanic part), 450 km (plate margin), 850 km (horizontal part of subducting slab) and 1200 km (continental part) for the middle of the model (y = 800 km) in Figure 3.12. See Figure 3.2 or 3.11d for positions of the strength profiles.

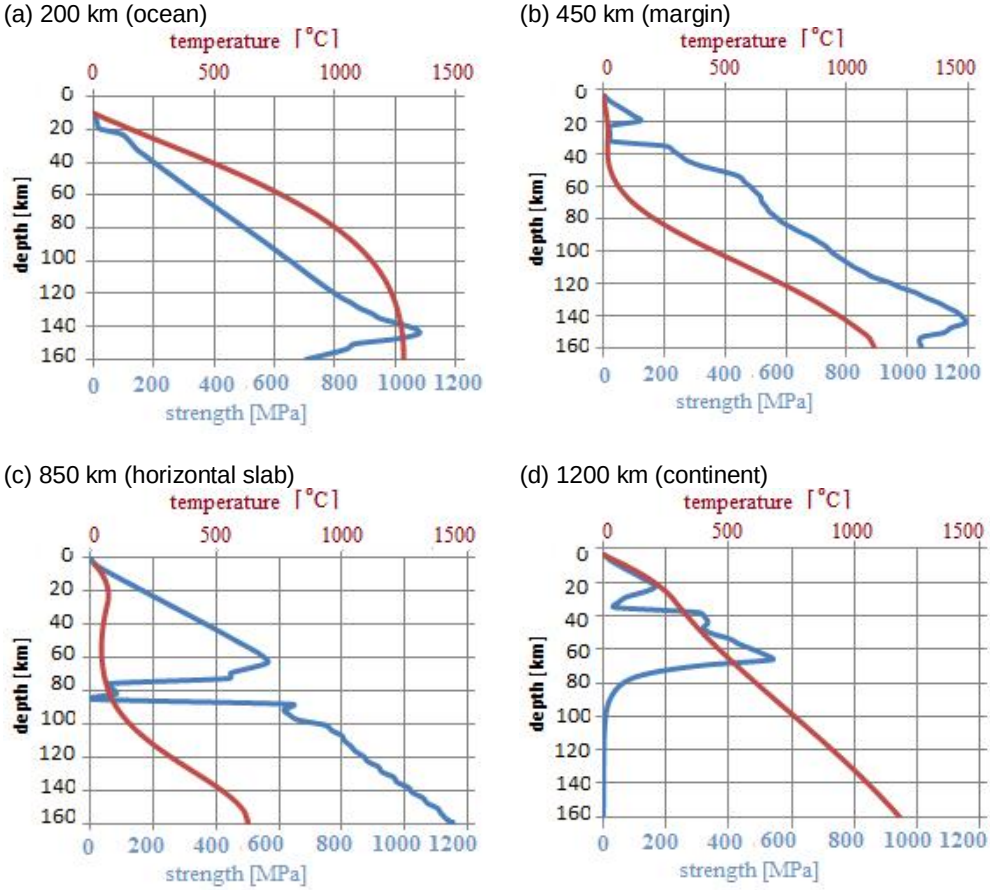

Figure 3.12. Strength envelopes (blue, scaling at the bottom axis) and geotherms (red, scaling at the top axis) of the PFSS model after 1 Ma coupled run time. All profiles are from the middle of the model (y = 800 km) and in positions eastward (a) 200 km, (b) 450 km, (c) 850 km and (d) 1200 km (see Figure 3.11d). Note different scale of strength [MPa] for panel oceanic strength versus continental strength.

In comparison to the initial strength envelopes of the PFSS (Figure 3.4c and d) the strength of the oceanic lithosphere (Figure 3.11a) has not changed significantly. Still, maximum strength of the oceanic lithosphere is reaching ~1100 MPa in around 140 km depth. The strength of the continental lithosphere (Figure 3.11d) differs from its initial state. Smoothening of the initial temperature field implementation and advection of heat from the implemented heat production and basal heat influx (heat production and influx at continental side only) have altered the geotherm. The in the crust and uppermost mantle lithosphere increased temperatures have weakened the material and a maximum strength of around 550 MPa is reached at ~65 km depth. Here, frictional plastic deformation transitions to viscous deformation. At the plate margin (Figure 3.11b), the strength profile exhibits frictional plastic behavior in the upper continental crust with a maximum strength of around 120 MPa at 20 km depth. The increase in crustal strength is the result of the decreased temperature. Temperature is generally decreasing in the area above the slab and especially in the part traveling horizontally. Beneath the slab, the profile is reaching towards the strength profile of the oceanic lithosphere and asthenosphere, only colder temperatures increase strength. Contrary to the strength profile at the margin of the subduction zone (Figure 3.11b), the weak oceanic crust is not positioned between the upper and lower crust, but cuts between the lower continental crust and mantle lithosphere at around 80 km depth in the profile positioned at the horizontal part of the slab (Figure 3.11c). Here, a significant decrease in strength can be detected at the position of the slab. Below the slab the profile reaches into the altered (linear viscous) oceanic mantle lithosphere and strength increases. The low geothermal gradient (see also temperature field in Figure 3.11d and e) has the strongest influence on lithospheric strength.

Overall, parts of the strength profiles compare fairly well to general lithospheric strength envelopes, but are heavily influenced by the abnormally cold environment, especially in the subduction zone (e.g. van der Pluijm and Marshak, 2004; Stüwe, 2007; Turcotte and Schubert, 2014).

Sliver movement in the PFSS experiments is restricted in areal extent and magnitude of velocity. The sliver develops directly after initiation of the experiment (Figure 3.13a) and stabilizes after the temperature spin up (Figure 3.13b-d). Sliver movement is mainly restricted to the close vicinity of the plate margin in the forearc of the subduction zone. Northward directed velocities reach magnitudes of around 0.3 cm/a. A second smaller area of strain partitioning is observed at the latter end of the horizontal part of the subducting slab. This, however, might be an artefact caused by the general velocity field. The velocity field is only prescribed at the base of the model domain and not within. This way is the internal velocity field only restrictedly controllable and the collision-type velocity field at the second bend of the slab is inevitable. Also, the abnormally low temperatures in the area around the horizontally traveling slab favor a coupling between the slab and the overriding plate.

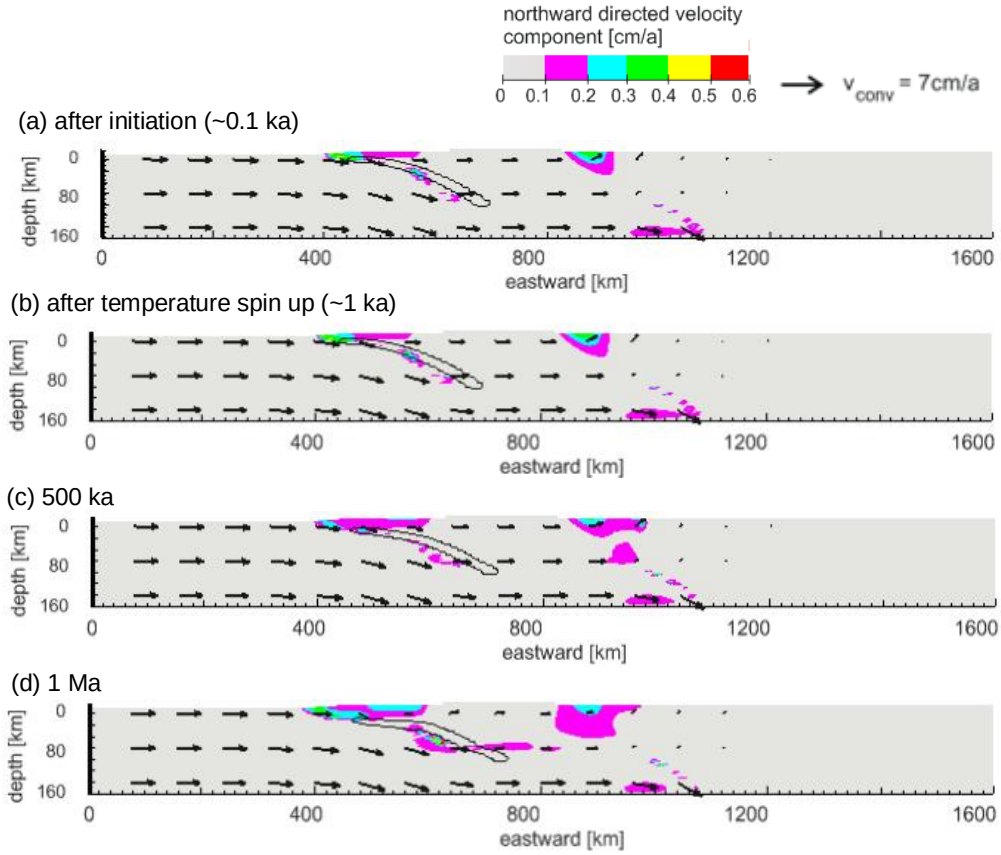

Figure 3.13. Side view of the velocity field (black arrows) and northward directed velocity component of the PFSS model after (a) initiation (~0.1 ka), (b) temperature spin up (~1 ka), (c) 500 ka and (d) 1 Ma. The black contour line indicates the location of the weak continental slab.

In spite of poor decoupling of the oceanic and continental plates, the strain partitioning behavior of the thermo-mechanical models presented here and that of the purely mechanical models from Case Study II are quite similar. The areal extent of the forearc sliver in this thermo-mechanical model (Figures 3.13 and 3.14) is about the same as in the purely mechanical experiments (Figure 2.5). Also, the magnitude of the velocity field is at the subduction margin the same for both experiments. Similarly, purely mechanical and thermo-mechanical models develop the limited sliver movement above the horizontal part of the slab (e.g. Figure 2.5).

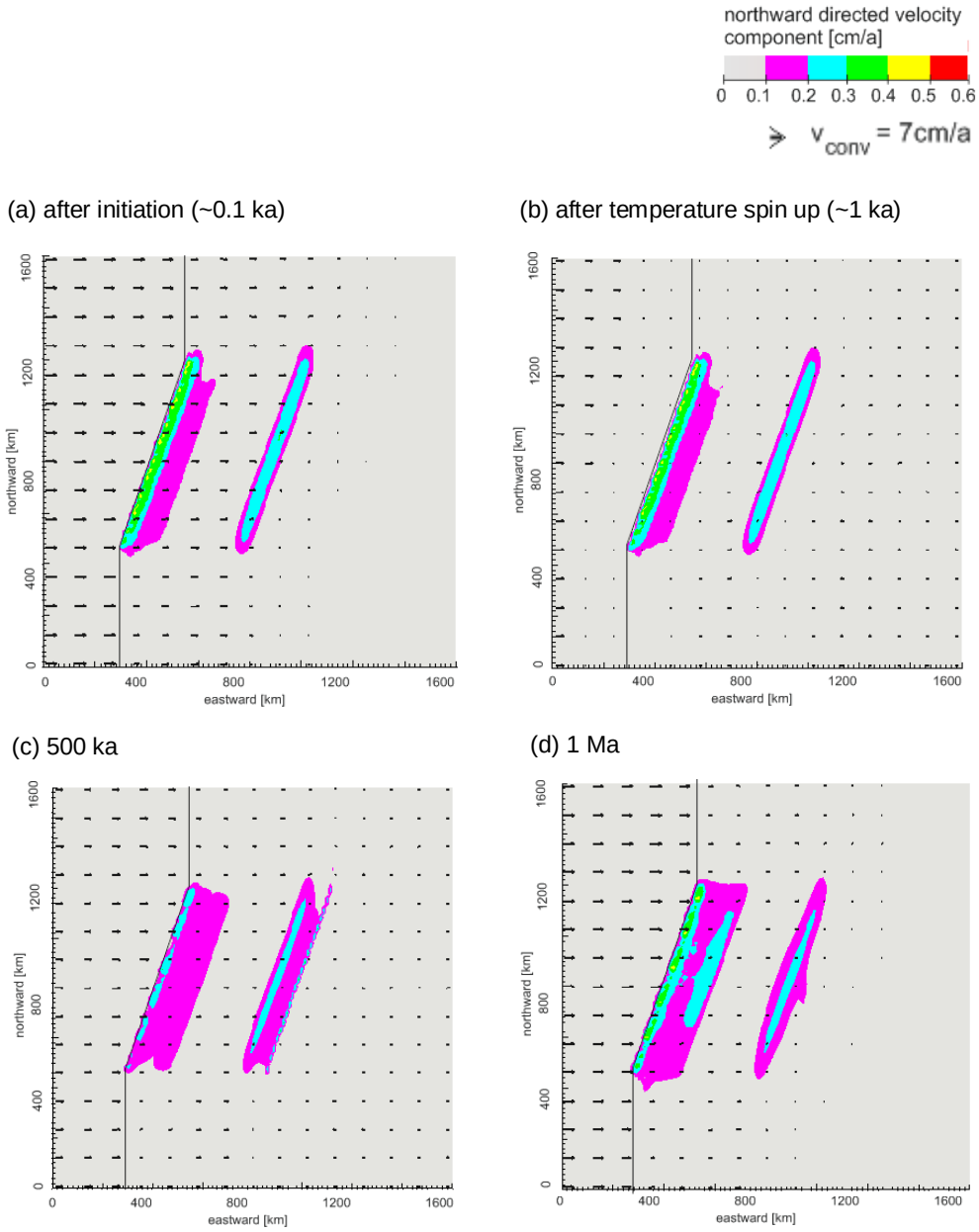

Figure 3.14. Map view of the velocity field (black arrows) and northward directed velocity component (colored for the interval 0 cm/a to 0.6 cm/a) of the PFSS model after (a) initiation (~0.1 ka), (b) temperature spin up (~1 ka), (c) 500 ka and (d) 1 Ma coupled run time. The black line indicates the boundary between the plates.

Due to the poor thermal solution of the PFSS experiments, conclusions regarding strain partitioning can only cautiously be drawn. It can, however, be noticed that the overall sliver movement of this thermo-mechanical experiment of the PFSS is in quite good agreement with the results from the purely mechanical experiments in Case Study II. This similarity in behavior was already observed for the NVZ experiments and suggests that the mechanical calculations (which ultimately determine the crustal deformation in the overriding plate) are probable, even with a misbehaving (i.e., not coinciding with nature) temperature field.

The observed sliver movement, or lack thereof, suggests that the smaller obliquity angle is the main reason for restricted sliver movement in the flat slab (or step-shaped) subduction zones. The total velocity field, however, points out a deficiency of the model, which is as such not observed in nature. Due to the slab not being detached from the overriding plate, 'collision' above the second descend of the slab is observed. The fact that this collision is not observed in nature, suggests that slab and overriding plate must be fully detached in nature. Measured seismicity along the plate interface (Gutscher, et al., 2000; McNulty and Farber, 2002) suggests this, too. This would also suppress the second onset of sliver movement.

The surface heat flow values shown in Figure 3.14 have been calculated using Fourier's law. Acknowledging but excluding the artificial peak above the second descend of the slab caused by above described collision-like pattern, heat flow across the subduction zone is in generally good agreement with the expected pattern (e.g. Pollack and Chapman, 1977; Stein, 2003). Crossing over the subducting plate margin from west to east (as shown in Figure 3.15a) the heat flow values decrease from a level at about 62 mW/m^2 above the oceanic plate towards the plate margin. Heat flux values of the oceanic crust are in good agreement of expected values for an about 30 Ma old cooling oceanic lithosphere. Starting with an initial temperature field of an about 10 Ma old oceanic lithosphere, 20 Ma temperature spin-up results in a 30 Ma old oceanic lithosphere. A slight decrease in surface heat flux is expected above the margin. This is obtained in the experiment, even though values are very low. This is due to the addressed low temperatures above the slab. Increase of surface heat flux is expected when moving further eastward over the margin into the continent. Continental surface heat flux values of around 43 $W/m^2$are observed. That is slightly too low. Having implemented a heat production of 1 $\mu W/m^3$ in a 30 km thick crust and a basal heat flux of around 20 W/m^2, heat flux of around 50 W/m^2would be expected. The low values are possibly explained by the already discussed alteration of the geotherm from a rough initial implementation towards a smooth temperature field. The main artefact is the peak above the second descent of the slab. This is artificially induced by the 'collision' mentioned earlier on. In the numerical study of flat-slab subduction conducted by English, et al. (2003) a volcanic center is evolving above the second descend of the slab. This is, however, firstly, not observed in the PFSS, and, secondly, due to a dehydrating slab (English, et al., 2003) and not due to mechanically coupled slab and overriding plate (this experiment). Since dehydration is not incorporated in the code, there should not be any kind of uplift observed for a properly working experiment. The expected curve for a fully balanced flat slab subduction zone is indicated in green in the surface heat flux plot in Figure 3.15a.

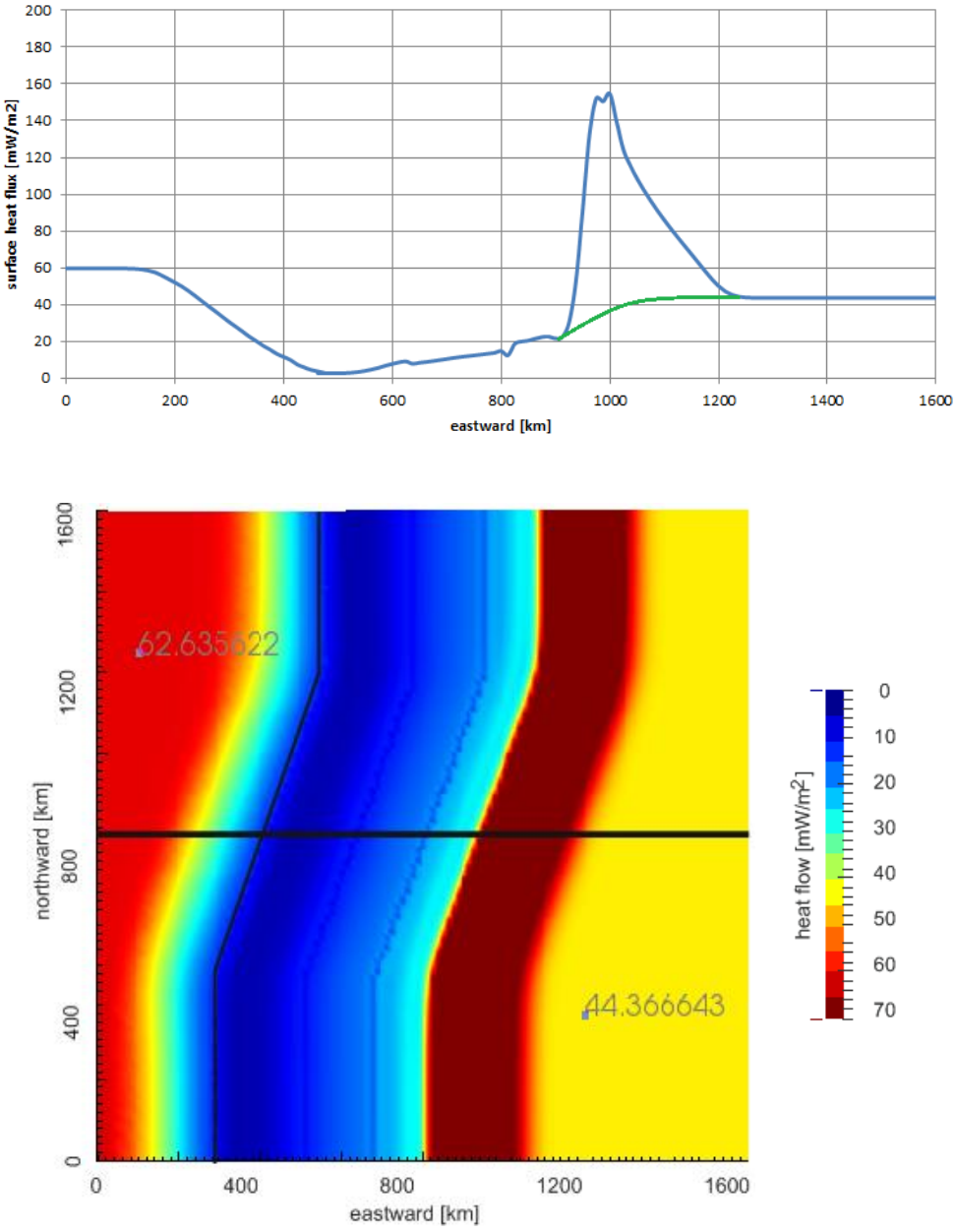

Figure 3.15. Heat flow [mW/m^2] calculated using Fourier's law at 2 Ma run time. (a) Surface heat flow graph through the middle of the model (y = 800 km), green line shows expected heat flux between 900 and ~1200 km east, (b) map view of surface heat flow with black line indicating the plate margin and bold black line marking the position of the heat flow graph.

To conclude from the thermo-mechanical experiments, it should be noticed that especially the NVZ experiment is in a good condition to be applied for investigation of for example other subduction zones or general examination of subduction zone characteristics. The initial design of the model resembles coarsely the topography of present day Andes. Temperature field as well as velocity field evolution give a good representation of what is expected. Strength profiles and overall surface heat flow curves show that the behavior of the model is consistent. Sliver movement in the NVZ is agreeing well with the results of the purely-mechanical experiments and with observations in nature. Although the lack of sliver movement in the PFSS is also agreeing with the results of the purely-mechanical experiments, one important issue in the temperature evolution has to be acknowledged. The area above the horizontally traveling part of the slab is very cold. This leads to a lack of detachment of the slab from the overriding plate in the PFSS experiment, which results in artificial collision-like behavior in the continental crust above the second descent of the slab. Without drastically changing the design and boundary conditions of the model, this artefact cannot to be removed. However, the experiments presented here do represent nature well and exposing a boundary between fully successful and partly failing thermo-mechanical experiments, they offer a good starting point for the development of fully coupled and self-evolving models.

Discussion

Case Studies I, II and III investigate the influence of various subduction zone characteristics, such as the subduction dip and obliquity angle, on the deformation and dynamics of the continental plate. While experiments of Case Studies I and II are purely mechanical, Case Study III is revisiting these reference experiments with a thermo-mechanical model.

Generally, it was confirmed through the experiments that oblique motion from the incoming oceanic plate has main influence on the dynamics of the overriding plate and is needed to initiate sliver formation and margin-parallel movement in the continent. Secondly, the presence of a predefined continental weakness divides the continental plate such that the wedge above the subducting slab between the margin and the weak zone is escaping as one block under the influence of the oblique motion transferred onto it from the incoming subducting plate. This weak zone in the continental crust enhances strain partitioning and sliver movement in the continent significantly. Further, a proportional trend between the dip angle and the width of a deforming continental sliver is observed: shallower subduction dip angles lead to wider slivers. These main findings with regard to the geometric characteristics of a subduction zone (subduction dip angle, obliquity angle), a continental weakness in the continental crust and strain partitioning in the overriding plate are summarized in Figure 1.

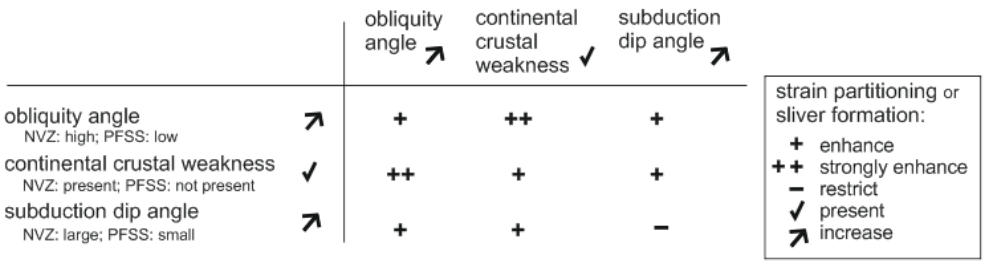

Figure 1. Comparison of main subduction zone characteristics obliquity angle, continental crustal weakness and subduction dip angle (and combination) with respect to sliver formation.

The experiments presented here show very good agreement with observations in nature. The northern study area, the Northern Volcanic Zone (NVZ), is characterized by steep (approx. 35°) oblique (about 40°) subduction and a prominent volcanic zone (e.g. Ramos, 1999; Stern, 2014) and shear zones (e.g. Veloza, et al., 2012; Yepes, et al., 2016). The southern study area, the Peruvian Flat Slab Segment (PFSS), is characterized by a step-shaped subducting slab (e.g. Gutscher, et al., 2000), a small obliquity angle (around 20°; e.g. Yepes, et al., 2016) and lack of volcanism. Comparable results include sliver movement in the NVZ (Case Study I: Chapter 1.2.1) with velocities of on average ~1 cm/a (e.g. Nocquet, et al., 2014; Gutscher, et al., 1999) and reduced sliver movement in the PFSS (Case Study II: Chapter 2.2.1) with velocities of ~0.5 cm/a (e.g. Nocquet, et al., 2014; Veloza, et al., 2012). In addition to the

magnitude of velocities, the modelled extent of the sliver is also similar to the observations: in the NVZ the sliver is well defined between the plate margin and the Dolores Guayaquil Mega (DGM) and Chingual-Cosanga-Pallatunga-Puná (CCPP) shear zones (see Chapter 2.2 on the NVZ). In the PFSS the sliver is not defined well and pronounced shear zones are missing (see Chapter 2.3 on the PFSS).

The case studies in this work present a systematic approach on how the various subduction zone characteristics influence the dynamics in the continental crust, and they have confirmed previous ideas and advanced the knowledge of the interrelation between subduction zone geometries, relative plate motion, (pre-) existing crustal structures and dynamics in the continental plate. Thermo-mechanical experiments support these results, but also present deficiencies in the coupling of mechanical and thermal calculations with the model design and properties.

Understanding of strain partitioning in subduction zones

Strain partitioning or sliver movement in the continental crust of the overriding plate in a subduction zone requires oblique relative plate motion and is enhanced by (pre-) existing weaknesses in the continental crust. This was an expected outcome and experiments have confirmed and strengthened this view.

Strain partitioning describes the behavior when the oblique component of relative motion between the two plates is large enough such that the combined movement of subduction and oblique shearing at the slab interface is divided into pure dip-slip movement at the slab interface and horizontal shearing at the rear of the subduction zone. In these cases, a block of continental crust, or sliver, detaches and moves above the slab along the margin. The sliver is bounded by the margin itself, the slab interface and a shear zone in the interior of the continental plate. In environments like the NVZ, the shear zone is well pronounced and further enforced by a volcanic arc. The obliquity angle contributes significantly to the development of sliver movement. The subduction dip angle is less influential, but plays a role in enhancing sliver movement by increasing the interplate friction for shallow subduction angles. This effect is, however, not dominant, as it would otherwise suggest broad sliver movement in flat-slab subduction zones or step-shaped subduction zones like the PFSS. In these environments the sliver movement is restricted despite increased interplate friction. A shear zone, volcanic arc or other continental weakness, which would enhance sliver movement, may not be present in this kind of environment either. Subduction zones with a flat dip angle usually lack arc volcanic activity. A volcanic arc is not only re-enforcing the possible weak point in the continent but also introducing heat to the system and thermally weakening the continental crust. Heat is an important factor in all geological and geophysical processes, so as well in subduction zone settings. While the cold slab subducts into warm underlying material, heat exchange and convection influence material properties, deformation style and overall dynamics.

Comparison of purely mechanical and thermo-mechanical experiments

Despite their simplicity very good results are obtained from the purely mechanical models (Case Studies I and II). Further developing these to thermo-mechanical models and including temperature calculations turned out to be more difficult than expected. While material properties typical of other geodynamic numerical modelling studies are provided, advection of heat strongly affects the models. This can lead to positive feedbacks where regions become hot and weak, then deform more and weaken further. To counteract this behavior, material properties, e.g. viscosity, can be modified using a scaling factor. This however, steps back from desired self – consistent models.

In order to obtain good results, the initial temperature field was defined such that it follows the geometry of the subducting slab. Also, analytical temperature calculations of a cooling oceanic lithosphere and a steady-state continental lithosphere were used to initialize the model temperatures. Although a reasonable estimate for the temperature field at the start of the simulations is used, use of basal velocity boundary conditions allow only limited control of the velocity field within the interior of the modeling domain. This is generally true, but for the thermo-mechanical models of greater disruptive effect due to e.g. strong coupling between units caused by undercooling of the system. In order to maintain reasonable velocity fields (e.g. to suppress unnatural uplift), material properties of the oceanic mantle lithosphere and asthenosphere were altered to ignore the influence of heat. This change still allows heat conduction, but means that the model moves back from a fully coupled thermo-mechanical model. Concentrating on the deformation of the continental crust, a proper velocity field has higher priority. With this the thermo-mechanical and purely mechanical model results regarding the sliver formation in the continental crust are in good agreement with each other and with observations in nature.

It has, however, to be mentioned that there are still some issues with some of the experiments. While the NVZ thermo-mechanical experiments are generally in good agreement with observations in nature, the PFSS features a collision-like uplift above the second descent of the slab. This is resulting from lack of detachment between the slab and the overriding plate and leads to not only material uplift but also increased crustal temperature and thus in an artificial peak in surface heat flux. The fact that this collision and high surface heat flux is not observed in nature, suggests that slab and overriding plate must be fully decoupled in nature. Measured seismicity along the plate interface (e.g. Gutscher, et al., 2000) and suggested active detachment faulting above the Peruvian flat slab (McNulty and Farber, 2002) supports this view. Further aspects of thermo-mechanical experiments of the flat-slab are discussed in more detail below.

(Thermo-) mechanical experiments of flat-slab subduction

The challenge of thermo-mechanical subduction zone modeling lies in the more complex geometry of a flat-slab subduction. Velocity boundary conditions are defined at the base of the model and while this balances mass influx from the side, there is limited control over the velocity field in the interior of the model. For a simple parabolic slab, the boundary

conditions can be adjusted such, that the slab roughly follows the preferred subduction path. In the case of flat-slab subduction geometry, the slab must first subduct, then flatten to travel horizontally and again bend downward to finally subduct completely, which is more difficult to control with the velocity boundary conditions. The velocity field might not follow the slab, but shortcut over the first descent. This does not only cause a bad velocity field but also lack of detachment between the slab and the overriding plate. This particularly holds true, when models get more complicated and different factors like temperature are incorporated.

In order to overcome the issues caused by basal velocity boundary conditions, subduction would ideally not be driven kinematically (as in this study), but gravitationally. To realize this, a model domain including the entire upper mantle is needed. However, focusing on crustal deformation requires high resolution in the uppermost kilometers of the model. This cannot be realized in a mantle scale model. For this reason the limitations caused by the size of this 3D model need to be accepted.

Several numerical studies (e.g. Gutscher, et al., 2000; Van Hunen, et al., 2002; Ramos and Folguera, 2009; Arrial and Billen, 2013; Liu and Currie, 2016) have addressed the question of what makes a slab to bend up to travel horizontally and equally, why the slab bends down again. The main factors in order to create a flat slab are a buoyant oceanic ridge or plateau (Gutscher, et al., 2000; Ramos and Folguera, 2009) and a subduction margin advancing into the continent (Liu and Currie, 2016). In the PFSS region, the Nazca Ridge has already been mentioned as a cause of flat subduction (see Chapter 2.3 The Peruvian Flat Slab Segment). Of the suggested factors causing flat subduction mentioned above only advancing subduction is included in this work. In order to remove the flat slab, slab dehydration and weakening of the crust as well as densification of an oceanic plateau is believed to be necessary (Van Hunen, et al., 2002; Arrial and Billen, 2013; Liu and Currie, 2016). The experiments presented here do not include either of these processes.

A thermal modeling study of flat subduction by English et al. (2003) suggests the formation of a volcanic arc above the second descent of the flat slab could develop due to slab dehydration. This description coincides with slab dehydration and weakening of the crust described by Liu and Currie (2016), for example, followed by repealing of the flat slab. In the same location, the PFSS experiment shows uplift of continental crust. The obtained uplift is, however, not due to hydration (slab hydration is not incorporated in the code), but is a result of one/ the velocity boundary conditions not explicitly dictating the velocity field in the interior of the model and two/ lack of detachment between the overriding plate and subducting slab.

The broad region of very low temperatures above the horizontal part of the slab in the PFSS experiment is caused by heat advection away from a fixed temperature boundary. This is mainly related to the velocity field. However, thermal processes (i.e. dehydration, fluid transport, partial melting or changes in deformation pattern) not accounted for in the temperature calculations would influence this behavior and possibly partly counteract (extreme) cooling. Even though, mantle wedge flow might be of less importance in the flat-

slab subduction zone geometry, in the normal subduction setting, heat convection in the mantle wedge would possibly enforce the volcanic arc and, with that, sliver formation.

Thermo-mechanical experiments: Temperature field and surface heat flow

The initial temperature field of the NVZ and the PFSS experiment were defined to follow the shape of the subducting slab for the thermo-mechanical models as shown in Figure 3.2. Further, analytical solutions (Stein and Stein, 1992; Chapman, 1986) based on the material properties applied in the model (Case Study III: Table 3) were used to initialize the temperature fields of the oceanic and continental lithosphere. This measure has in several tests shown to be necessary in order to achieve a feasible velocity and temperature field throughout the model run. Starting from a linear conductive geothermal gradient, run times to reach steady state in the continental crust would have been long (couple of days) even when performing temperature calculations without updating the velocity solution (Figure 3.3). Also, if running the experiment until reaching steady state in the continental side, the oceanic side would need to be defined separately to compensate for aging and cooling of the oceanic lithosphere. The temperature spin-up is kept in the experiments even with ready-made input temperature fields in order to ensure a proper incorporation of the magma chamber in the continental crust and to smooth out the initially discretized temperature field via heat conduction. With these measures, the (evolving) temperature field resembles the typical temperature field of a subduction zone well: cool slab and relatively cool near-slab environment. The temperature field above the horizontally traveling slab in the PFSS experiment is too cold compared to nature and to other thermal numerical studies of flat subduction (e.g., English et al., 2003). This generally influences strength and dynamics of the overriding plate. However, the upper crust is in any case thought to deform in frictional plastic manner. The temperature field of the NVZ experiment is evolving properly.

Surface heat flows extracted from the model results generally agree well with subduction zone heat flow curves (e.g., Pollack and Chapman, 1977; Peacock, 1996). Also, the magnitude of heat flow is matching global (Davies, 2013) and regional (e.g., Hamza and Muños, 1996) heat flow data. The obtained heat flow values are also consistent within the model. Starting from a geotherm resembling a 10 Ma old oceanic lithosphere, the 20 Ma temperature spin-up decreases the oceanic plate temperature and surface heat flux of the aging oceanic crust. The continental crust is expected to have a surface heat flow of around 50 mW/m^2 (resulting from an implemented heat production of 1 $\mu W/m^3$ in a 30-km-thick crust and a basal heat influx of 20 mW/m^2). The continental heat flux is compared to this consideration a bit too low. This is probably explained by the initial rough implementation of the geotherms and leveling out initial bumps might cause deviations form expected values. Also, the initial geotherms rather underestimate than overestimate temperature, which might add in to a colder temperature regime in the uppermost crust. Slightly too cold conditions are, however, not influencing the deformation of the crust significantly, as the uppermost kilometers are behaving plastically.

The peak in surface heat flux above the second descent of the slab in the PFSS experiment is resulting from the collision-like uplift, which is caused by lack of detachment of the slab

from the overriding continental crust. Despite this undesired uplift and low heat flow above the cold region above the horizontal slab (see above), the heat flux is satisfactorily represented in the PFSS as well.

According to a 2D numerical modeling study by Springer (1999), the subduction dip angle can influence the surface heat flow. A positive correlation is shown for the relation between the increase in subduction dip angle and decrease in surface heat flow above the margin. However, this effect is only very small and in the models presented here only marginally visible, if the effect is visible at all due to the abnormally low temperatures above the slab in the PFSS.

Thermo-mechanical experiments: Lithospheric strength

The lithospheric strength profiles shown in Case Study III (Figures 3.4 (initial state both experiments) and 3.7 (NVZ) and 3.12 (PFSS)) are calculated using the Mohr-Coulomb frictional plastic yield criterion for brittle strength as shown in Equation 3.24 in Chapter 3.1.5 and the power-law viscous flow law for ductile strength as shown in Equation 3.30 in Chapter 3.2.2. Using these rheologies, the oceanic crust reaches maximum strengths of around 20 MPa. Beneath that, the material is defined to be linear viscous with a high viscosity pre-factor and maximum strength reaches up to 1100 MPa at around 140 km depth (mantle asthenosphere). The strength of the continental crust is similarly reaching to 20 MPa but increases further to around 1100 MPa at depths of 110 km. The strength profiles for the PFSS experiment are alike but altered in the continental side by a lower viscosity pre-factor; maximum strength of 550 MPa is reached at depths of about 65 km. In some cases these results deviate from expectations in nature owing to design choices in the numerical experiments. For instance, consider the alteration of the oceanic mantle lithosphere and asthenosphere strengths mentioned above. The materials are set to be temperature independent and rigid or highly viscous, while keeping heat transfer properties. The strength profiles through the oceanic and purely continental part (in the far field of the subduction zone) are not significantly altered throughout both runs. An influence of the weak slab as well as the hot magma chamber on the lithospheric strength and geotherm is observed in the strength profiles cutting through the margin (Figures 3.7b and Figure 3.12b), the continental weak zone with magma chamber (Figure 3.7c) and the horizontally traveling slab (Figure 3.12c). In the latter, again abnormally low temperatures are influencing the strength. Comparison to other numerical studies shows that the established strength profiles of this work are in good (e.g. Kohlstedt, et al., 1995; Rey and Houseman, 2006) and fairly good agreement (e.g. Huismans and Beaumont, 2014; Regenauer-Lieb, et al., 2006) with previous studies, with a tendency to be too weak (e.g. Burov and Yamato, 2007; Schmalholz, et al., 2009). Strength profiles are a combination of pressure-dependent, brittle strength and temperature- and strain-rate-dependent, viscous strength, which are easily altered using different material properties and model concepts (e.g., “jelly sandwich” vs. “crème brûlée”; Burov and Watts, 2006).

One reason for mismatches in strength can be assumed to be in the roughly estimated thicknesses of lithospheric layers. The Moho is at a depth of around 50 km in the continental plate, which is slightly deeper than usually observed (e.g. Stüwe, 2007; Turcotte and Schubert, 2014). This issue is obviously influencing the dynamics of the entire model and thus of the continental crust as well. Also, the (subducting) oceanic crust is up to 14 km thick. The artificial layer thicknesses are partly due to computational issues, such as resolution, but also simplicity. This is discussed further in the following section. Strength profiles of the presented experiments show a structure of brittle and ductile deformation throughout the model domain and demonstrate that the here presented thermo-mechanical models are valid for interpretations of crustal deformation.

Assumptions and restrictions

General assumptions have been made in order to keep the numerical experiments simple while capturing the first-order physical processes thought to be important in an oblique subduction setting. Assumptions and restrictions have been briefly mentioned in the respective Case Studies I, II and III and in the Chapter in context of thermo-mechanical experiments but will be reviewed here in order to provide a complete list.

For all the experiments, the upper most surface has been kept fixed throughout the entire experiment. This was decided after several attempts with a free surface, which ended with numerical problems and/or horizontal surfaces with several hundreds of meters to kilometers of elevation between the plates. The uppermost surface is designed such that it roughly resembles the topography of South America. This ensures reasonable results even after short run times. Although isostasy and gravity are influenced by changes in topography, the main concern lies on stable numerical solutions.

A crustal root underneath the mountain range has effects on isostasy and composition (e.g., strength, velocity) in the interior of the model domain. A crustal root is not included in the model. The deeper parts of the continental crust will be deforming in ductile manner and will not necessarily be a strong influence on the deformation and strain partitioning in the upper continental crust, which this study is focusing on. The emphasis lying on the upper continental crust is one reason to allow simplicities such as neglecting crustal roots or roughly estimating (lithospheric) layer thicknesses.

Some layer thicknesses are overestimated. This is partly due to numerical issues, but also due to simplicity and the estimate that the effect on the upper crustal deformation processes is minor. Numerical issues include, for example, the 14 km thick oceanic upper crust (the subducting slab) in the PFSS experiment. A 7-km-thick oceanic crust corresponds to 2 elements in the model discretization, which was not recognized as a mechanical weakness in the calculations and needed to be thicker. The input material properties describing the layers are few in the purely mechanical experiment and are not temperature dependent in the thermo-mechanical experiments. This means that they influence the materials behavior (e.g. thermal conductivity and density) under influence of temperature, but do not change during

the experiment. Further differentiation of materials would have unnecessarily made the model more complex.

The same ‘simplicity rule’ applies to age differences in the oceanic crust and presence of oceanic ridges. They are neglected. The age of the oceanic crust would influence the density and thus buoyancy of the subducting slab, which could affect the subducting dip angle. With kinematic boundary conditions for subduction, this is not a concern.

The subducting slab is not gravitationally initiated, but kinematically. Gravitational slab initiation would be favorable but a significantly deeper model domain would be necessary to realize this. In this study it is chosen to force the slab onto its path by defining basal velocity boundary conditions and pulling the slab together with underlying lithosphere and mantle down and out of the domain. Material is pushed into the domain at the sides of the model in order to keep the material flux in balance. A thicker model domain and more sophisticated thermal processes would improve the experiments, their comparability to nature and their presentation regarding subduction zone dynamics. This would mean to redesign the model geometry, boundary conditions, providing complex thermal calculations and lies with this beyond the scope of this work. It has to be added that when redesigning the model, resolution has to be reconsidered. With a mantle-scale model, resolution in the continental crust cannot be as high as it would be needed to make detailed statements on crustal deformation and dynamics.

The crustal weakness, employed in the continental plate, is realized by reducing the friction angle in the material in question. This weakness is mimicking a volcanic arc, a shear zone or otherwise pre-defined weakness in the continental crust. In the thermo-mechanical models a magma chamber is substituting the mechanical weakness and an area of higher temperature is implemented. The magma chamber is at constant heat and, as the mechanical continental weakness, its position and shape is following the entire oblique segment. Both features, the mechanically and the thermally induced continental weakness, are continuous and do not include any kind of variation in space or time. Under these assumptions, this is one end member behavior, simulating a strong thermal effect of arc volcanism. Variations of this approach could be targeted in future studies.

The rock strength of hot magma in magma chambers and feeding systems underneath volcanic arcs is very low (McBirney and Murase, 1984). It is thus intuitive to treat volcanic arcs as a continental crustal weakness. This has also been done in the Case Studies I and II (mechanically induced continental crustal weakness) as well as Case Study III (thermally induced continental crustal weakness). It has, however, to be mentioned that the presence of a volcanic arc system can also be source of increased rock strength in the crust by solidification of magma (Chernov, 2003). The solidification is usually triggered by the release of volatiles, mixing of materials or both (Hort, 1997) and results in, most importantly, cooling (Chernov, 2003; Zhao, et al., 2005) and thus an increase in strength. Results of the presented experiments show that sliver formation is strongly enhanced, when a continental crustal weakness is present, whereas it is restricted in the absence of a crustal weakness. It is

redundant in the here presented set up of test series, which investigates the role of a continental crustal weakness (possibly represented by a volcanic arc), to examine, what happens if the crust is even further strengthened by the solidification of magma; sliver movement is reduced in a strong continental crust. With a more sophisticated model (including melt generation and thermal weakening) it would be interesting to investigate, how sliver movement is generated in a scenario, where the volcanic arc itself is not directly associated with the sliver boundary, but, instead, a local thermal anomaly is weakening the continental crust (Rees Jones, et al., 2018).

All features in the model are perfectly parabolic, straight or box-shaped. These approximations to nature are satisfying to maintain simple and reproducible experiments.

Not only shapes are approximated, but also the distributions and nature of material properties. Materials in one defined area are homogenous and do not include heterogeneities such as smaller intrusions. In the purely mechanical experiments the layers of materials can be compared to sand, sugar or syrup layers in (unheated) analog models, which represent the majority of material present in certain regions of a subduction zone. The general idea of these representations is still valid in the more advanced thermo-mechanical models, but adjusting the material properties is more complicated.

General approximations and restrictions described above hold true for all presented experiments in this work. Additional, the thermo-mechanical experiments are more complex (than the purely mechanical) and require careful calibrating. Purely mechanical models do not include any temperature calculations, weakening or partial melting due to heat transfer. This heat might influence the deformation of the continental crust. A weaker continental crust might favor strain partitioning as the force restricting shear motion in the rear end of the subduction zone might be smaller and thus easier to overcome. On the contrary, a weaker slab might reduce friction and thus the obliquely dragging force between slab and overriding plate might be too small to initiate sliver movement.

The initial temperature field is, as mentioned, based on analytical solutions of a cooling oceanic lithosphere of 10 Ma (Stein and Stein, 1992) and a steady-state continental lithosphere (Chapman, 1986) using the material properties listed for the thermo-mechanical experiments (Table 3). These are calculated externally and introduced as ready-made input data into the code prior to starting the experiment. As described later, this process should be included in the experiment in future code developments. These future versions of the code, however, would need to acknowledge that, as stated above, running the experiment until reaching steady-state would leave the oceanic lithosphere in the wrong (too old, too cold) state.

The temperature fields in the thermo-mechanical models are adjusted to follow the geometry of the subducting slab. This reduces run time, in which a linear temperature field would need to adjust itself to the subduction scenario. The initial geotherms are not smooth. Even though, properties like surface heat flow are initially correct, deviations from expected

values can be caused by smoothening initial bumps in the geothermal gradient. Also, the temperature is rather underestimated than overestimated by the initial geotherms. A lower temperature regime in the uppermost crust is, however, not believed to influence the dynamics of the continental crust significantly. For one, a colder crustal layer is heating up during the temperature spin up and secondly, the uppermost tens of kilometers are deforming in a plastic manner.

As heat-dependent behavior is crucial in deformation processes of the Earth, thermo-mechanical models are desired. The thermo-mechanical models presented in Case Study III provide a starting point for future work on sophisticated thermo-mechanical models. Additionally to the pre-adjusted temperature fields a temperature spin up loop has been implemented to overcome long runtimes. Despite the mismatch between oceanic and continental thermal state, to reach steady state from the initial linear temperature field conditions a couple of hundred million years of run time would be required for the fully coupled model, which would take up to years using present available computational power. Further, there is no dehydration from the subducting slab implemented or other effects of heat, which might either restrict or favor strain partitioning. For example, as discussed above, dehydration in the slab might trigger volcanic centers and with that, similarly to the continental crustal weakness in the NVZ, enhance sliver movement. The simplifications described (e.g., ready-made temperature fields) demonstrate that also simple approaches require adjustments and careful calibrating in material properties to be functioning in a geophysically feasible way.

Comparison to other modeling studies

Since the advent of powerful computing machines numerical modelling studies of subduction zones have not only increased in number but also in complexity. Starting from transferring analog models into simple numerical models, various questions regarding subduction zones have been addressed (Gerya, 2011; Burov, et al., 2014). In order to be able to draw conclusions on which parameters are controlling the dynamics of the continental crust, it is useful to test these parameters systematically. Starting from the conditions of the NVZ, this work investigates first the influence of the continental weakness. Thereafter, the obliquity and subduction dip angle are investigated separately as well as in combination (cf. Figure 1 for main results). A similar strategy was followed in the PFSS experiments. These experiments are purely mechanical but the findings are highly valuable. Even though one important part, heat, is missing, the comparison to nature as well as to expected outcome confirms this.

Similar conclusions to what was observed in the experiments described in Case Studies I and II, have been drawn by other numerical, purely mechanical studies (e.g. Braun and Beaumont, 1995; Koster, et al., 2012): the obliquity angle needs to exceed a certain value (at least 30°; depending on the composition of the continental crust, i.e. homogenously strong or with crustal weakness) in order to initiate strain partitioning. Analog models confirm that the main demand for strain partitioning is that the driving force (or length of oblique subduction

zone) is exceeding the resisting force at the rear end of the subduction zone. This is usually the case for high inter-plate friction (MacCaffrey, 1992; Chemenda, et al., 2000; see also Chapter 3.3 Strain partitioning at obliquely convergent margins). The influence of pre-existing crustal weaknesses on the dynamics of the subduction zones has, at least to the author's knowledge, hitherto not been investigated in detail using 3D numerical models. Analog experiments (e.g., Chemenda et al., 2000) conclude that a continental crustal weakness is enhancing strain partitioning. This is also in line with the main findings of this work. In the analog subduction zone study of Chemenda et al. (2000) it was suggested, that a geometrically simple position (i.e. a continental weakness roughly following the rough geometry of the margin) is favoring strain partitioning. In this work, the continental crustal weakness is always aligned with the plate margin. In future model designs other geometries of continental weaknesses could be tested.

With the advance of numerical modelling studies of subduction zones, it was soon realized that numerical models have one great advantage over analog models: heat transfer can be (relatively) easily implemented (Burov, et al., 2014). Case Study III is coupling temperature calculations to the previously purely mechanical models. These thermo-mechanical models need a more careful calibration than purely mechanical models, because they are more complex. Both experiments (NVZ and PFSS) demonstrated how sensitive the model is to temperature. Several measures needed to be taken (see Assumptions and restrictions), in order to get a stable result.

Dynamics in the overriding plate have been addressed in serveral studies (e.g. van Hunen, et al., 2000; 2004; Sobolev and Babeyko, 2005; Gerya and Meilick, 2011). Recent highly sophisticated numerical models direct toward free erosion/sedimentation surface, coupled 2 or 3D thermo-mechanical experiments including dehydration and fluid transport, as well as partial melting (Clark, et al., 2008; Zhu, et al., 2009; 2011; Gerya and Meilick, 2011). In these models slab bending or overriding plate dynamics are not prescribed but are free to evolve spontaneously and are thus appropriate for studying stability of passive margins, overriding plate processes and extension and rift processes (Gerya, 2011). The development of these kinds of models lies beyond the scope of this work. The in this study presented thermo-mechanical models offer a good starting point for further development and refinement of the thermo-mechanical models in DOUAR. This is not only desirable, but also necessary if this code is to become a widely applicable tool. As was mentioned earlier, inter-plate friction is important for a high driving force of the oblique motion, which in turn needs to overcome the resisting force in order to initiate strain partitioning. Dehydration has shown to influence the inter plate friction (Gorczyk, et al, 2007) and adding this feature would thus be one important step for further investigation of continental dynamics in oblique subduction zones.

Overall are the models presented in this work falling in one of the two categories of numerical models described by Gerya (2011). They are simple models, which "attempt to isolate the influence of one or a small number of physical parameters on subduction processes based on notably simplified numerical setups". This is however one qualifying

approach and the systematic investigation of the influence of subduction dip angle, obliquity angle and continental weakness on strain partitioning performed in this study gives new insight as well as confirms previous findings.

Comparison to other subduction zones

The model results (of the purely mechanical experiments) are also applicable to other subduction zones without adjustment to the subduction system in question.

The Sumatra Java subduction zone is characterized by a normal subduction slab dip angle of around 30° and an approximate obliquity angle of 30° (USGS, Slab 1.0). Based on the results of Case Study I, the overriding plate is expected to develop a sliver movement with a bit smaller magnitude of velocity compared to the NVZ due to the smaller obliquity angle. Accordingly, a sliver movement of ~0.6 cm/a is observed along the Sumatra Fault, which runs approximately parallel to the subduction margin (McCaffrey, 2009).

The Kurils-Kamchatka Japan subduction zone is geometrically more complicated due to the triple point of the Eurasian, Philippine Sea and Pacific Plate. From northern to southern Japan, the subduction zone characteristics change from shallow (20°) to steeper (40°) subduction dip angle and from a very small obliquity angle (0° - 10°) to higher obliquity angle (30° - 40°) (Fitch, 1972; USGS, Slab 1.0). The model results of Case Study I (for the northern segment of the Japan subduction zone; north of 35° N) and Case Study II (for the southern segment; south of 35° N) predict no to very little strain partitioning in the northern segment and some intermediate sliver movement in the southern segment. These predictions are all excluding the respective lithospheric strength and specific subduction geometry. While sliver movement is vanishingly small in the northern segment of the Kurils-Kamchatka Japan subduction zone, the southern segment has developed an approximately 0.6 cm/a moving sliver, the Nankai Forearc sliver (Fitch, 1972).

A third example is Cascadia in north-western margin of North America. The subduction slab dip angle in Cascadia is rather small and the setting can be classified as a flat slab subduction (USGS, Slab 1.0; Gutscher, et al., 2000). The model results of Case Study II would suggest no sliver movement for obliquity angles less than 30° and only moderate sliver velocities for angles larger than 30°. Cascadia is characterized by an obliquity angle of around 20°-30°, but still sliver movement of ~0.7 cm/a are observed (Flesch, 2007). The Cascades are one example, where the generalization of the model results from this work does not hold true. The large scale influence of the adjacent plate tectonics needs to be considered. Here, in the example of Cascadia, the sliver movement can be an escape window for the margin parallel running San Andreas Fault, which is to the south adjacent to the Cascades (Flesch, 2007).

Future work

In the future, the focus should mainly lie on developing and refining of the thermo-mechanical models. In this study thermo-mechanical experiments were only briefly

discussed and it became clear that implementation of temperature calculations requires careful adjustment and calibration of material properties, boundary and initial conditions. Especially for more complicated slab geometries (flat-slab) basal velocity boundary conditions and simple temperature calculations alter the mechanical and temperature field too much. As discussed above, the temperature calculations do not account for dehydration, fluid transport, partial melting or changes in deformation pattern and the velocity boundary conditions may trigger the slab velocity to shortcut through the continental crust. To counteract the misbehavior observed in the thermo-mechanical models, a new model design would be desirable. Solutions would include a deeper model domain (at least 300 km) and thermal processes like dehydration and corner flow. The temperature field input data was pre-calculated using a cooling half-space model and a steady-state condition for the oceanic and the continental plate, respectively. Additionally, a temperature loop was implemented in the beginning of the run. The loop only updates the temperature field, while the velocity field is kept fixed. When the code exits this loop, velocity field and temperature field calculations are evolving dependently. Initially, the temperature spin-up was implemented to overcome the tremendous run time to achieve a stable/feasible (steady-state) geotherm from a linear temperature field. With the ready-made temperature input, this spin-up is mostly to even the initially discretized temperature field. In the future, this spin-up could possibly be used to calculate the cooling half-space and steady-state temperature fields (which is done externally now), which could then be fed in as input data.

Further, a free surface would be a good step towards self-evolving numerical models. Sedimentation, erosion but also uplift would be of interest for surface heat flow, for example, but generally for consistent gravity and isostasy effects in both purely mechanical and thermo-mechanical models. Additionally, the implementation of horizontal in-/out flux at the lateral margins of the model sliver domain would be of interest. This would allow applications to more subduction zones (e.g., the fault system in Colombia and Venezuela as an escape system for sliver movement in the NVZ; or Cascadia and the San Andreas Fault).

With these future implementations and improvements understanding of the processes and knowledge of subduction zone dynamics can be further advanced and numerical models of subduction zones can possibly be also used as a tool of prediction. This work, however, provides new insight into the influence of subduction zone geometry and presence of weak zones in the continental and oceanic plate on the deformation and dynamics of the continental plate.

Conclusions

The Earth's surface is undergoing constant change. This in a very general statement, but from a geoscientific perspective it includes continents shifting their position on the planet and deforming over long time scales. Continental collision, rifting apart and subduction are the main components in the Wilson cycle, which describes the cyclic interactions of continental and oceanic plates. Although much has been investigated and explored, not everything has been revealed to full understanding.

In oblique subduction systems, factors such as the dip angle of the subducting plate and the convergence obliquity, as well as the presence of weak zones in the overriding plate, all influence how oblique convergence is partitioned onto various fault systems. This has been investigated in three case studies: (I) the NVZ mechanical model, (II) the PFSS mechanical model, and (III) the NVZ and PFSS thermo-mechanical models.

For Case Study I, the reference model was designed after observations from the NVZ (5°N - 3°S), characterized by a ~35° subduction dip angle with an obliquity angle of about 40°, extensive volcanism and significant strain partitioning in the continental crust. The model results show clear strain partitioning in the area between the plate margin and the continental weakness. Modelled sliver velocities are in good agreement with observed GPS velocities in that area. A model run without a continental weakness suggests that a continental weakness is necessary for a proper sliver to develop in a moderately steep (approx. 35°) subduction setting. The obliquity angle has positive feedback on strain partitioning (for a larger angle more strain partitioning is observed) and the subduction dip angle has a negative feedback (for a shallower angle more strain partitioning is observed). A series of experiments combining small subduction dip angle with small obliquity angles shows that the obliquity angle has a larger effect than the subduction dip angle.

For Case Study II, the geometry of the subducting slab was changed, such that it resembles the PFSS (3°S -14°S). Here the subducting slab descends with an approximate angle of 35° and when reaching a depth of about 90-100 km bends to travel horizontally for around 300 km. The obliquity angle in this setting is small (~20°) and the continental crust lacks well-developed sliver movement. Experiments show, that in this flat slab setting the weakness of the oceanic slab and the obliquity angle gain importance. Strain partitioning – though not so pronounced – is observed above the horizontally traveling slab. Most importantly, with decreasing obliquity strain partitioning or sliver movement is significantly decreasing, too. The PFSS experiment shows only insignificant sliver movement with margin parallel velocities of about 0.5 cm/a, which is in good agreement with observed GPS values in this area.

Case study III is an extension of the investigations of Case Studies I and II. The NVZ and PFSS experiments are revisited under thermo-mechanical conditions. The temperature-dependent material and basal heat flux showed to have a very strong influence on the behavior of the experiments. Several measures including a separate temperature spin up

phase, adjusting the initial temperature field to the geometry of the slabs and alteration of the temperature-dependent rock properties where necessary to achieve reasonable results. Overall, thermo-mechanical models are supporting the results of the purely mechanical experiments. They also expose the boundary between successful (NVZ with normal subduction) and partly failing (PFSS with more complicated slab geometry) incorporation of temperature dependence into mechanical models. This provides a good starting point for further development of temperature dependent experiments.

Finally, it can be concluded, that the experiments are – despite their simplicity – in good agreement with observations in nature, in particular in the studied areas but also in comparison to global subduction zones. In summary, this work suggests that the obliquity angle is the main influence on the formation of strain partitioning in the continental crust. A weak zone in the continental crust enhances strain partitioning and the subduction angle in a simple parabolic shape of the slab has the smallest influence on strain partitioning. While purely mechanical and thermo-mechanical experiments do agree on sliver formation in the continental crust, the latter need to be developed in the future. With this, I like to close with that the work presented here provides new insight into the dynamics of subduction zones.

References

Almeida, F. F. M., de; Brito Neves, B. B., and de; Carneiro, C. D. R., 2000. The origin and evolution of the South American Platform. Earth-Science Reviews 50:77-111.

Alvarado, A., Audin, L., Nocquet, J. M., Jaillard, E., Mothes, P., Jarrín, P., Segovia, M., Rolandone, F., and Cisneros, D., 2016. Partitioning of oblique convergence in the Northern Andes subduction zone: Migration history and the present-day boundary of the North Andean Sliver in Ecuador. Tectonics, 35, 1048 – 1065.

Arcay, D., Tric, E., and Doin, M.-P., 2005. Numerical simulations of subduction zones Effect of slab dehydration on the mantle wedge dynamics. Physics of the Earth and Planetary Interiors 149, 133-153.

Arrial, P.-A. and Billen, M. I., 2013. Influence of geometry and eclogitization on oceanic plateau subduction. Earth and Planetary Science Letters 363, pp. 34–43.

Baes, M., Govers, R., and Wortel, R., 2011. Subduction initiation along the inherited weakness zone at the edge of a slab: Insights from numerical models. Geophys. J. Int. 184, 991–1008.

Bandy, W. L., Hilde, T. W. C., and Yan, C.-Y., 2000. The Rivera-Cocos plate boundary: Implications for Rivera-Cocos relative motion and plate fragmentation. Geological Society of America, Special Paper 334.

Barazangi, M. and Isacks, B. L. 1978. Spatial distribution of earthquakes and subduction of the Nazca plate beneath South America. Geology Vol 4, No 11.

Beaumont, C. Ngyuen, M. H., Jamieson, R. A., and Ellis, S., 2006. Crustal flow modes in large hot orogens. From: Law, R. D., Searle, M. P., and Godin, L. (eds) Channel Flow, Ductile Extrusion and Exhumation in Continental Collision Zones. Geological Society, London, Special Publications, 268, 91-145.

Berrocal, J. and Fernandez, C., 2005. Flat subduction beneath the Andean region from seismological evidences. 6th International Symposium on Andean Geodynamics (ISAG 2005, Barcelona), Extended Abstracts: 107-110

Bird, P., 1978. Finite elements modelling of lithosphere deformation: The Zagros collision orogeny. Tectonophysics 50, 307-336.

Bourgois, J., 2013. A Review on Tectonic Record of Strain Buildup and Stress Release across the Andean Forearc along the Gulf of Guayaquil-Tumbes Basin (GGTB) near Ecuador-Peru Border. International Journal of Geosciences, 4, 618--635.

Braun, J., 1993. Three-dimensional numerical modeling of compressional orogenies: Thrust geometry and oblique convergence. Geology, vol 21, 153-156.

Braun, J. and Beaumont, C., 1995. Three-dimensional numerical experiments of strain partitioning at oblique plate boundaries: Implications for contrasting tectonic styles in the southern Coast Ranges, California, and central South Island, New Zealand. Journal of Geophysical Research, Vol. 100, No B9.

Braun, J., Thieulot, C., Fullsack, P., DeKool, M., Beaumont, C., and Huismans, R., 2008. DOUAR: A new three-dimensional creeping flow numerical model for the solution of geological problems. Physics of the Earth and Planetary Interiors, 171(1-4):76–91.

Braun, J. and Sambridge, M., 1997. Modelling landscape evolution on geological time scales: a new method based on irregular spatial discretization. Basin Res. 9.

Braun, J. and Sambridge, M., 2001. Landscape evolution models: a software review. Hydrological Processes 15.

Burbidge, D. R. and Braun, J., 1998. Analogue models of obliquely convergent continental plate boundaries. Journal of Geophysical Research 103, 15,221 – 15,237.

Burov, E., Francois, T., Yamato, P., and Wolf, S., 2014. Advances and challenges in geotectonic modelling. Bulletin de la Société Géologique de France, n 3, 147-168.

Burov, E. and Watts, A., 2006. The long-term strength of continental lithosphere: "jelly sandwich" or "crème brûlée"? GSA Today, Vol 16, No 1.

Burov, E. and Yamato, P, 2008. Continental plate collision, P-T-t-z conditions an unstable vs. stable plate dynamics: Insights from thermos-mechanical modelling. Lithos 103.
Campbell, C. J., 1974. Ecuadorian Andes. Geological Society, London, Special Publications 4, 725-732.

Chapman, D. S., 1986. Thermal gradients in the continental crust. From: Dawson, J.B., Carswell, D.A., Hall, J.T., and Wedepohl, K.H. (eds), 1986. The Nature of the Lower Continental Crust, Geological Society Special Publication No 24, pp 63-70.

Chemenda, A., Lallemand, S., and Bokun, A., 2000. Strain partitioning and interplate friction in oblique subduction zones: Contraints provided by experimental modeling. Journal of Geophysical Research, Vol 105, No B3.

Chernov, A. A., 2003. A model of magma solidification during explosive volcanic eruptions. Journal of Applied Mechanics and Technical Physics, Vol. 44, No. 5, 667–675.

Chopra, P. N. and Paterson, M. S., 1984. The role of water in the deformation of dunite. Journal of Geophysical Research, Vol 89, No B9, pp. 7861-7876.

Cediel, F., Shaw, R. P., and Cáceres, C., 2003. Tectonic Assembly of the Northern Andes Block. in C. Bartolini, R. T. Buffler, and J. Blickwede, eds., The Circum-Gulf of Mexico and the Caribbean: Hydrocarbonhabitats, basin formation, and plate tectonics: AAPG Memoir 79,p. 815–848.

Clark, S. R., Stegman, D., and Müller, R. D., 2008. Episodicity in back-arc tectonic regimes. Physics of Earth and Planetary Interior 171, 265-279.

Cobbold, P. R. and Rossello, E. A., 2003. Aptian to recent compressional deformation, foothills of the Neuquén Basin, Argentina. Marine and Petroleum Geology 20(5), 429-443

Cobbold, P. R., Rossello, E. A., Roperch, P., Arriagada, C., Gómez, L. A., and Lima, C., 2007. Distribution, timing, and causes of Andean deformation across South America. From: Ries, A. C., Butler, R. W. H., and Graham, R. H. (eds), 2007. Deformation of the Continental Crust: The Legacy of Mike Coward. Geological Society, London, Special Publications, 272, 321-343.

Corredor, F., 2003. Seismic strain rates and distributed continental deformation in the northern Andes and three-dimensional seismotectonics of northwestern South America. Tectonophysics 372, 147–166.

Cosma, L., Lapierre, H., Jaillard, E., Laubacher, G., Bosch, D., Desmet, A., Mamberti, M., and Gabriele, P., 1998. Petrographie et géochimie des unites magmatiques de la Cordillére occidentale d´Équatuer (0°30´S): implications tectoniques. Bulletin de la Société Geologique de France, 169.

Courant, R., Friedrichs, K., Lewy, H., 1928. Über die partiellen Differenzengleichungen der mathematischen Physik. Mathematische Annalen (in German), 100 (1), 32–74.

Currie, C.A., Ducea, M.N., DeCelles, P.G., and Beaumont, C., 2015, Geodynamic models of Cordilleran orogens: Gravitational instability of magmatic arc roots, in De Celles, P.G., Ducea, M.N., Carrapa, B., and Kapp, P.A., eds., Geodynamics of a Cordilleran Orogenic System: The Central Andes of Argentina and Northern Chile: Geological Society of America Memoir 212, pp. 1–22, doi:10.1130/2015.1212(01).

Davies, J. H., 2013. Global map of solid Earth surface heat flow. Geochemistry Geophysics, Geosystems, 14, pp. 4608–4622

Dewey, F. J., and Lamb, S.H., 1992. Active tectonics of the Andes. Tectonophysics 205, 79-95.

Dumitru, T. A,. 1991. Refrigeration of the western Cordilleran lithosphere during Laramide shallow-angle subduction. Geology Vol 19, No 11.

Duretz, T., Gerya, T. V., and May, D. A., 2011. Numerical modelling of spontaneous slab breakoff and subsequent topographic response. Tectonophysics 502, 244–256.

Egbue, O. and Kellog, J., 2010. Pleistocene to Present North Andean 'escape'. Tectonophysics 489, 248-257.

English, J. M., Johnston, S. T., and Wang, K., 2003. Thermal modelling of the Laramide orogeny: testing the flat-slab subduction hypothesis. Earth and Planetary Science Letters 214, pp. 619-632.

Faccenna, C., Oncken, O., Holt, A. F., Becker, T. W., 2017. Initiation of the Andean orogeny by lower mantle subduction. Earth and Planetary Science Letters 463, 189–201.

Fitch, T. J., 1972. Plate Convergence, Transcurrent Faults, and Internal Deformation Adjacent to Southeast Asia and the Western Pacific. Journal of Geophysical Research 77.

Flesch, L. M., 2007. A possible "window of escape" in the southern Cascadia subduction zone. Geology, Research Focus, 35, 959–960.

Gaetani, G. A. and Grove, T. L., 1998. The influence of water on melting of mantle peridotite. Contributions to Mineralogy and Petrology, 131, 323–346.

Gansser, A., 1973. Facts and theories on the Andes. Journal of Geological Society London, 129.

Gerya, T. V., 2011. Future directions in subduction modeling. Journal of Geodynamics 52, 344-378.

Gerya, T. V. and Meilick, F. I., 2011. Geodynamic regimes of subduction under an active margin: effects of rheological weakening by fluids and melts. Journal of Metamorphic Geology 29, 7-31.

Gerya, T. V. and Yuen, D. A., 2003. Rayleigh-Taylor instabilities from hydration and melting propel 'cold plumes' at subduction zones. Earth and Planetary Science Letters 212, 47-62.

Gerya, T. V., Yuen, D. A., and Maresch, W. V., 2004. Thermomechanical modelling of slab detachment. Earth and Planetary Science Letters 226, 101-116.

Gleason, G. C. and Tullis, J., 1995. A flow law for dislocation creep of quartz aggregates determined with the molten salt cell. Tectonophysics 247, pp 1 - 23.

Gorczyk, W., Willner, A. P., Gerya, T. V., Connolly, J. A. D., and Burg, J.-P., 2007. Physical controls of magnetic productivity at Pacific-type convergent margins: new insights from numerical modeling.

Physics of the Earth and Planetary Interior 163, 209-232.

Gregory-Wodzicki, K. M., 2000. Uplift history of the Central and Northern Andes: A review. GSA Bulletin, V 112, no. 7, 1091–1105.

Gross, D. and Seeling, Th., 2011. Fracture Mechanics; With an Introduction to Micromechanics. Chapter 2. Springer

Gutscher, M.A., Malavielle, J., Lallemand, S. and Collot, J.Y., 1999. Tectonic segmentation of the North Andean margin: impact of the Carnegie Ridge collision (Vol 168, pg 255, 1999). Earth and Planetary Science Letters, 170(1-2): 155-156.

Gutscher, M-A., Spakman, W., Bijwaard, H., and Engdahl, E. R., 2000. Geodynamics of flat subduction: Seismicity and tomographic contraints from the Andean margin. Tectonics Vol 19, No 5, 814-833.

Hager, B. H. and O'Connell, R. J., 1978. Subduction zone dip angles and flow driven by plate motion. Tectonophysics, 50, pp. 111-133.

Ham, M. L. and Herrera Jr., L. J., 1963. Role of Subandean fault system in tectonics of eastern Peru and Ecuador. In: Backbone of the Americas, eds. Childs, O. and Beebe, B. W. American Association of Petroleum Geologists Memoir, 2, 47-61.

Hamza, V. M. and Muños, M., 1996. Heat flow map of South America. Geothermics Vol. 25, No 6, 599-646.

Harvard CTM database, earthquakes between 1900 and 2014 with magnitude above 5; http://www.globalcmt.org/CMTsearch.html

Hassani, R. and Jongmans, D., 1997. Study of plate deformation and stress in subduction processes using two-dimensional numerical models. Journal of Geophysical Research 7.

Hess, H. H., 1962. History of Ocean Basins. Petrologic studies: a volume to honor A. F. Buddington. Geological Society of America, 599-820.

Holmes, A., 1931. Radioactivity and Earth Movements. Transactions of the Geological Society, Glasgow, Vol 18, 559–606.

Hort, M., 1997. Abrupt Change in Magma Liquidus Temperature because of Volatile Loss or Magma Mixing: Effects on Nucleation, Crystal Growth and Thermal History of the Magma. Journal of Petrology Vol. 39, N. 5, 1063-1076.

Huchon, P. and Bourgois, J., 1990. Subduction-induced fragmentation of the Nazca Plate off Peru: Mendana Fracture Zone and Trujillo Trough revisited. Journal of Geophysical Research Atmospheres 95, 8419-8436.

Huismans, R., S. and Beaumont, C., 2014. Rifted continental margins: The case for depth-dependent extension. Earth and Planetary Science Letters 407, 148-162.

Isacks, B. and Molnar, P., 1971. Distribution of Stresses in the Descending Lithosphere from a Global Survey of Focal-Mechanism Solutions of Mantle Earthquakes. Review of Geophysics and Space Physics 9, No. 1.

Jarrard, R. D., 1986. Relations among subduction parameters. Reviews of Geophysics No 24 (2), 217-284. doi:10.1029/RG024i002p00217

Jaillard, E., Soler, P., Carlier, G., and Mourier, T., 1990. Geodynamic evolution of the northern and central Andes during early to middle Mesozoic times: a Tethyan model. Journal of the Geological Society, London 147, 1009-1022

Ji, Y., and Yoshioka, S., 2015. Effects on slab geometry and obliquity on the interplate thermal regime associated with the subduction of three-dimensionally curved oceanic plates. Geoscience Frontiers, Vol 6, 61-78.

Kanamori, H., 1977. The energy release in great earthquakes. Journal of Geophysical Research, 82, 2981-2987.

Kellner, A., 2007. Different styles of deformation of the fore-arc wedge along the Chilean convergent margin: Insights from 3D numerical experiments. Dissertation thesis, University Potsdam, Germany.

Knezevic Antonijevic, S., Wagner, L. S., Kumar, A., Beck, S. L., Long, M. D., Zandt, G., Tavera, H., and Condori, C., 2015. The role of ridges in formation and longevity of flat slabs. Nature 524.

Kohlstedt, D. L., Evans, B., and Mackwell, S. J., 1995. Strength of the lithosphere: Constraints imposed by laboratory experiments. Journal of geophysical research Vol 100, No B9, 587 – 602.

Kono, M., Fukao, Y., and Yamamoto, A., 1989. Mountain building in the central Andes. Journal of Geophysical Research 94, 3891–3905, doi:10.1029/JB094iB04p03891.

Koster, K. L., Haq, S. S., and Flesch, L. M., 2012. A Numerical Study of Strain Partitioning and the Development of Forearc Slivers at Obliquely Convergent Margins. American Geophysical Union, Fall Meeting 2012, abstract #T33F-2713

Kumar, A., Wagner, L. S., Beck, S. L., Long, M. D., Zandt, G., Young, B., Tavera, H., and Minaya, E., 2016. Seismicity and state of stress in the central and southern Peruvian flat slab. Earth and Planetary Science Letters 441, 71–80.

Lallemand, S., Heuret, A., and Boutelier, D., 2005. On the relationships between slab dip, back-arc stress, upper plate absolute motion, and crustal nature in subduction zones. Geochem. Geophys. Geosyst., 6, Q09006, doi:10.1029/2005GC000917.

Lavenu, A., 2006. Neotectónica de los Andes entre 1°N y 47°S (Ecuador, Bolivia y Chile): una revisión. Revista de la Asociación Geológica Argentina 61, 504-524.

Levin, H. L., 2013. The Earth through time. Chapter Nine. Wiley E-Text. ISBN: 978-1-118-54945-2.

Li, Z. H., Xu, Z. Q., and Gerya, T.V., 2011. Flat versus steep subduction: Contrasting modes for the formation and exhumation of high- to ultrahigh-pressure rocks in continental collision zones. Earth and Planetary Science Letters 301, 65–77.

Liu, S. and Currie, C. A., 2016. Farallon plate dynamics prior to the Laramide orogeny: Numerical models of flat subduction. Tectonophysics 666, pp. 33 47.

Mackwell, S. J., Zimmerman, M. E., and Kohlstedt, D. L., 1998. High-temperature deformation of dry diabase with application to tectonics on Venus. Journal of Geophysical Research, Vol 103, No B1, pp. 975-984.

Malatesta, C., Gerya, T. V., Crispini, L., and Capponi, G., 2016. Interplate Deformation at Early-Stage Oblique Subduction: 3d Thermomechanical Numerical Modeling: 3D modeling of interplate deformation. Tectonics. doi: 10.1002/2016TC004139

McBirney, A. R. and Murase, T, 1984. Theological Properties of Magmas. Annual Review of Earth and

Planetary Sciences 12, 337-357.

McNulty, B. and Farber, D., 2002. Active detachment faulting above the Peruvian flat slab. Geology, Vol. 30, No. 6.

McCaffrey, R., 2009. The Tectonic Framework of the Sumatran Subduction Zone. Annual Review of Earth and Planetary Science 37, 345–66.

McCaffrey, R., 1992. Oblique Plate Convergence, Slip Vectors, and Forearc Deformation. Jounral of Geophysical Research, Vol. 97, No. B6, 8905-8915

Meagher, D., 1980. Octree Encoding: A New Technique for the Representation, Manipulation and Display of Arbitrary 3-D Objects by Computer. Rensselaer Polytechnic Institute, Technical Report IPL-TR-80-111.

Minear, J. W. and Toksöz, M. N., 1970. Thermal regime of a downgoing slab and new global tectonics. Journal of Geophysical Research 75, 1397-1419

Molnar, P., Freedman, D., and Shih, J. S. F., 1979. Lengths of intermediate and deep seismic zones and temperatures in downgoing slabs of lithosphere. Geophysical Journal of the Royal Astronomical Society., 56, 41-54.

Mooney, W. D., 1979. Seismic refraction studies of the Western Cordillera, Colombia and the East Pacific-Caribbean Ridge during the Jurassic and Cretaceous and the evolution of Western Colombia. Ph. D. Thesis, University of Wisconsin, 84p.

Mora, A., Parra, M., Strecker, M. R., Sobel, E. R., Hooghiemstra, H., Torres, V., and Vallejo Jaramillo, J., 2008. Climatic forcing of asymmetric orogenic evolution in the Eastern Cordillera of Colombia. GSA Bulletin 120, No. 7/8, 930–949.

Mora-Páez, H., Mencin, D. J., Molnar, P., Diederix, H., Cardona-Piedrahita, L., Peláez-Gaviria, J.-R., and Corchuelo-Cuervo, Y., 2016. GPS velocities and the construction of the Eastern Cordillera of the Columbian Andes. Geophysical Research Letters, 43, 8407-8416.

Nocquet, J-M., Villegas-Lanza, J. C., Chlieh, M., Mothes, P. A., Rolandone, F., Jarrin, P., Cisneros, D., Alvarado, A., Audin, L., Bondoux, F., Martin, X., Font, Y., Régnier, M., Vallée, M., Tran, T., Beauval, C., Maguiña Mendoza, J. M., Martinez, W., Tavera, H., and Yepes, H., 2014. Motion of continental slivers and creeping subduction in the northern Andes. Nature geoscience Vol 7.

Orme, A. R., 2007. The Tectonic Framework of South America. In: Veblen, T. T., Young, K. R., and Orme, A. R. (eds.) The Physical Geography of South America. Oxford University Press.

Peacock, S. M., 1996. Thermal and Petrologic Structure of Subduction Zones. Geophysical Monograph, American Geophysical Union.

Pennington, W. D., Mooney, W. D., van Hissenhoven, R., Meyer, H., Ramirez, J. E., Meyer, R. P., 1979. Results of a reconnaissance microearthquake survey of Bucaramanga, Colombia. Geophysical Research Letters 6, 65-68.

Pilger R.H., 1981. Plate reconstructions, aseismic Ridges, and low-angle subduction beneath the Andes, Geological Society American Bulletin, 92, 448–456.

Pindell, J. L., and Kennan, L., 2009. Tectonic evolution of the Gulf of Mexico, Caribbean and northern South America in the mantle reference frame: an update. From: James, K. H., Lorente, M. A. and Pindell, J. L. (eds) The Origin and Evolution of the Caribbean Plate. Geological Society, London, Special Publications, 328, 1–55. doi: 10.1144/SP328.1

Pluijm, van der, B. A. and Marshak, S., 2004. Earth Structure: an introduction to structural geology and tectonics. 2nd edition W.W. Norton & Company, Inc. ISBN 0-393-92467-X

Pollack, H. N. and Chapman, D. S., 1977. On the regional variation of heat flow, geotherms, and lithospheric thickness. Tectonophysics 38, pp. 279-296.

Pulido, N., 2003. Seismotectonics of the northen Andes (Colombia) and the development of seismic networks. Bulletin of the International Institute of Seismology and Earthquake Engineering, 2003 Special Edition, p69-76.

Pulido, N., Nakai, S., Yamanaka, H., Calderon, D., Aguilar, Z., and Sekiguchi, T., 2014. Estimation of a Source Model and Strong Motion Simulation for Tacna City, South Peru. Journal of Disaster Research 9, No.6.

Ramos, V. A., 1999. Plate tectonic setting of the Andean Cordillera. Episodes Col 22, 3.

Ramos V. A., Cristallini E. O., and Pérez, D. J., 2002. The Pampean flat-slab of the Central Andes. Journal of South American Earth Sciences 15, 59-78.

Ramos, V. A., 2015. South America, Geological history. In: Encyclopædia Britannica Online. Retrieved 10 November, 2015, from http://global.britannica.com/place/South-America.

Ramos, V. A. and Folguera, A., 2009. Andean flat-slab subduction through time. From: Murphy, J. B., Keppie, J. D., and Hynes, A. J. (eds) Ancient Orogens and Modern Analogues. Geological Society, London, Special Publications, 327, 31–54.

Rees Jones, D. W., Katz, R. F., Tian, M., and Rudge, J. F., 2018. Thermal impact of magmatism in subduction zones. Earth and Planetary Science Letters 481, 73–79.

Regenauer – Lieb, K., Weinberg, R. F., and Rosenbaum, G., 2006. The effect of energy feedbacks on continental strength. Nature Vol 442.

Rey, P. F. and Houseman, G., 2006. Lithospheric scale gravitational flow: the impact of body forces on orogenic processes from Archean to Phanerozoic. From: Buiter, S. J. H and Schreurs, G (eds.) Analogue and numerical modeling of crustal scale processes. Geological Society, London, Special Publications, 25, 153-167.

Roperch, P., Mégard, F., Laj, C., Mourier, T., Clube, T., and Noblet, C., 1987. Rotated oceanic blocks in western Ecuador. Geophysical Research Letters, 14, pp. 558-561.

Rosenbaum, G., Giles, D., Saxon, M., Betts, P. G., Weinberg, R. F., Duboz, C., 2005. Subduction of the Nazca Ridge and the Inca Plateau: Insights into the formation of ore deposits in Peru. Earth and Planetary Science Letters 239, 18-32.

Sacks, I . S., 1983. The subduction of young lithosphere. Journal of Geophysical Research Vol 88. 3355-3366.

Schmalholz, S. M., Kaus, B. J. P., and Burg, J.-P., 2009. Stress-strength relationship in the lithosphere during continental collision. Geology 37, No 9, 775-778.

Schmeling, H., Babeyko, A. Y., Enns, A., Faccenna, C., Funiciello, F., Gerya, T., Golabek, G. J., Grigull, S., Kaus, B. J. P., Morra, G., Schmalholz, S. M., and van Hunen, J., 2008. A benchmark c comparison of spontaneous subduction models – towards a free surface. Physics of the Earth and Planetary Interiors, Volume 171.

Sébrier, M. and Soler, P., 1991. Tectonics and magmatism in the Peruvian Andes from late Oligocene

time to the Present. GSA Special Papers 265, 259-278.

Sobolev, S. V. and Babeyko, A. Y., 2005. What drives orogeny in the Andes? Geology 33, 617-620.

Springer, M., 1999. Interpretations of heat-flow density in the Central Andes. Tectonophysics 306, 377-395.

Stein, C. A., 2003. Heat flow and flexure at subduction zones. Geophysical Research Letters, Vol 30, No 23.

Stein, C. A. and Stein, S., 1992. A model for the global variation in oceanic depth and heat flow with lithospheric age. Nature 359

Stern, R. J., 2002. Subduction zones. Reviews of Geophyics, Vol 40 No 4.

Stern, C. R., 2004. Active Andean volcanism: its geologic and tectonic setting. Revista Geológica de Chile, Vol 31, No 2, 161-206.

Stevens, C., McCaffrey, R., Bock, Y., Genrich, J., Pubellier, M., Subarya, C., 2002. Evidence for block rotations and basal shear in the world's fastest slipping continental shear zone in NW New Guinea. In: Stein, S., Freymueller, J. (eds.). Plate Boundary Zones: AGU Geodynamics Series 30, 101-122.

Stüwe, K., 2007. Geodynamics of the Lithosphere. Springer-Verlag Berlin Heidelberg, 2nd Edition.

Syracuse, E. M., van Keken, P. E., and Abers, G. A., 2010. The global range of subduction zone thermal models. Physics of the Earth and Planetary Interiors 183, 73–90.

Taboada, A., Rivera, L. A., Fuenzalida, A., Cisternas, A., Philip, H., Bijwaard, H., Olaya, J., and Rivera, C., 2000. Geodynamics o the northern Andes: Subductions and intracontinental deformation (Colombia). Tectonics, Vol. 19.

Torrance, K. and Turcotte, D. L., 1971. Thermal convection with large viscosity variations. Journal of Fluid Mechanics, 47, 113-125.

Turcotte, D. L. and Schubert, G. (2014) Geodynamics, Third edition. Cambridge University Press.

USGS, Slab 1.0 interactive map, slab models for subduction zones: http://usgs.maps.arcgis.com/apps/webappviewer/index.html?id=de81616029224bf699813ef7941a2ee0. Accessed April 2007.

Upton, P., and Koons, P. O., 2003. Extension and partitioning in an oblique subduction zone, New Zealand: Constraints from three-dimensional numerical modeling. Tectonics 22, doi:10.1029/2002TC001431

Van Hunen, J., van den Berg, A.P., and Vlaar, N.J., 2000. A thermo-mechanical model of horizontal subduction below an overriding plate. Earth and Planetary Science Letters 182.

Van Hunen, J., van den Berg, A.P., and Vlaar, N.J., 2000. On the role of subducting plateaus in the development of shallow flat subduction. Tectonophysics 352.

Van Hunen, J., van den Berg, A.P., and Vlaar, N.J., 2004. Various mechanisms to induce shallow flat subduction: a numerical parameter study. Phys. Earth Planet. Inter. 46, 179–194.

Veloza, G., Styron, R., Taylor, M., and Mora, A., 2012. Open-source archive of active faults for northwest South America. GSA Today, Vol 22, No 10.

Webb, J., 1990. Imposing linear constraints in finite-element analysis. Comm. Appl. Num. Methods Vol 6.

Wegener, A., 1912. Die Herausbildung der Grossformen der Erdrinde (Kontinente und Ozeane), auf geophysikalischer Grundlage. Petermanns Geographische Mitteilungen (in German) 63, 185–195, 253–256, 305–309.

Wessel, P. and Müller, R. D., 2009. Plate Tectonics, In: Schubert, G. and Watts, A. B. (eds.) Crust and Lithosphere Dynamics, Treatise on Geophysics, 6, 49-98.

Wilson, J. T., 1966, Did the Atlantic close and then re-open?, Nature, 211(5050), 676-681

Whipp, D. M. Jr., Beaumont, C., and Braun, J., 2014. Feeding the " aneurysm ": Orogen-parallel mass transport into Nanga Parbat and the western Himalayan syntaxis. Journal of Geophysical Research: Solid Earth, 119.

Wortel, M. J. R., Remkes, M. J. N., Govers, R., Cloetingh, S. A. P. L., and Meijer, P. T., 1991. Dynamics of the lithosphere and the intraplate stress field. Philosophical Transactions of the Royal Society of London

Yepes, H., Audin, L., Alvarado, A., Beauval, C., Aguilar, J., Font, Y., and Cotton, F., 2016. A new view for the geodynamics of Ecuador: Implication in seismogenic source definition and seismic hazard assessment. Tectonics 35, pp. 1249 – 1279.

Zhao, C., Hobbs, B. E., Ord, A., Peng, S., Mühlhaus, H. B., and Liu, L., 2005. Numerical modelling of chemical effects of magma solidification problems in porous rocks. International Journal for numerical methods in engineering 64, 709–728.

Zeumann, S., 2013. 3D Finite Element Modelling of the Central Andean subduction zone with realistic geometry. Dissertation thesis, Friedrich-Schiller-Universität Jena, Germany.

Zhu, G., Gerya, T. V., Yuen, D. A. Honda, S., Yoshida, T., and Connolly, A. J. D, 2009. 3D dynamics of hydrous thermalchemical plumes in oceanic subduction zones. Geochemistry, Geophysics Geosystems 10.

Zhu, G., Gerya, T. V., Honda, S., Tackley, P. J., and Yuen, D. A., 2011. Influences of the buoyancy of partially molten rock on 3D plume patterns and melt productivity above retreating slabs. Physics of Earth and Planetary Interior 185, 112-121.